The Pennsylvania State University

The Graduate School

Department of Energy and Mineral Engineering

MODELING OF HYDRAULIC FRACTURE NETWORK PROPAGATION IN SHALE GAS RESERVOIRS

A Thesis in

Energy and Mineral Engineering

by

Chong Hyun Ahn

Submitted in Partial Fulfillment
of the Requirements
for the Degree of

Master of Science

December 2012

The thesis of Chong Hyun Ahn was reviewed and approved* by the following:

John Yilin Wang
Assistant Professor of Petroleum and Natural Gas Engineering
Thesis Advisor

Derek Elsworth
Professor of the Department of Energy and Mineral Engineering, and the Center for Geomechanics, Geofluids, and Geohazards

James Terry Engelder
Professor of Geosciences

R. Larry Grayson
Professor of Energy and Mineral Engineering;
George H., Jr., and Anne B. Deike Chair in Mining Engineering;
Graduate Program Officer of Energy and Mineral Engineering;
Undergraduate Program Officer of Mining Engineering

*Signatures are on file in the Graduate School

ABSTRACT

The most effective method for stimulating shale gas reservoirs is massive hydraulic fracture treatments. Recent fracture diagnostic technologies such as microseismic technology have shown that complex fracture networks are commonly created in the field. The interaction between pre-existing natural fractures and the propagating hydraulic fracture is a critical factor affecting the complex fracture network. However, many existing numerical models simulate only planar hydraulic fractures without considering the pre-existing fractures in the formation. The shale formations already contain a large number of natural fractures, so an accurate fracture propagation model needs to be developed to optimize the fracturing process.

In this paper, we first characterized the interaction between hydraulic and natural fractures. We then developed a new, coupled numerical model that integrates dynamic fracture propagation, reservoir flow simulation, and the interactions between hydraulic fractures and pre-existing natural fractures. By using the developed model, we also conducted parametric studies to quantify the effects of rock toughness, stress anisotropy, and natural fracture spacing on the geometry and conductivities of the hydraulic fracture network. Lastly, we introduced new parmeters *Fracture Network Index (FNI) and Width Anistropy* (W_{ani}) which may describe the creation of the fracture network due to natural fracture. This new knowledge helps one understand and optimize the stimulation of shale gas reservoirs.

TABLE OF CONTENTS

LIST OF FIGURES

LIST OF TABLES

ACKNOWLEDGMENT

First, I would like to express my deep appreciation for my parents and my sister, who have supported me in every endeavor. My family has provided the moral support necessary for me to pursue my dreams.

I also want to thank my thesis advisor, Dr. John Yilin Wang, for his guidance, patience, and confidence. Without his help, this research would not have been possible. I would also like to thank Dr. Derek Elsworth and Dr. Terry Engelder for being on my thesis committee members.

I also extend many thanks to each member of the staff at the Penn State 3S Laboratory, who gave me encouragement when the research was particularly challenging. Mohamad Zeini Jahromi has mentored me throughout my academic career. I also want to take the opportunity to thank Quan Gan, Daniel Kunho Kim, Kyung-soo Kim, and Jianhang Han for their sincere advice.

Chapter 1

INTRODUCTION

Production from low-permeability formations has become a major source of the natural gas supply. In 2010, low-permeability reservoirs accounted for about 56% of natural gas production and about 35% of natural gas consumption in the United States. Tight gas formations include shale, sandstone, carbonate, and coal beds, whose matrix permeability is less than 0.1 md and, as illustrated in Figure 1, shale gas plays spread the U.S. geographically. The highlighted areas represent Marcellus Shale, which hold the highest amount of gas in place.

Shale gas reservoirs are organic-rich formations and are the source rock as well as the reservoir. Gas is stored in the limited pore space of the fracture and matrix, and a sizeable fraction of gas is adsorbed on the organic material (Cipolla, 2009). Shale formations have ultra-low permeability of 10 to 1000 nano-Darcy but contain 50 to 1,500 TCF of natural gas. In addition, typical shale gas reservoirs have a net thickness of 50 to 600 ft., porosity of 0.02 to 0.08, total organic carbon (TOC) of 1-14% and are found at depths of 1,000-13,000 ft. Thus, shale reservoirs must be stimulated effectively to be economically feasible.

The use of hydraulic fracturing in conjunction with horizontal drilling in shale gas formations has unlocked natural gas resources that were not previously economically feasible. As shale gas production has expanded into more basins and the technology has improved, the amount of shale gas reserves has increased dramatically. However, our understanding of the fracture propagation in the low-permeability formations is still limited. New knowledge in this area leads to increased reserve and improved gas recovering for the nation and world.

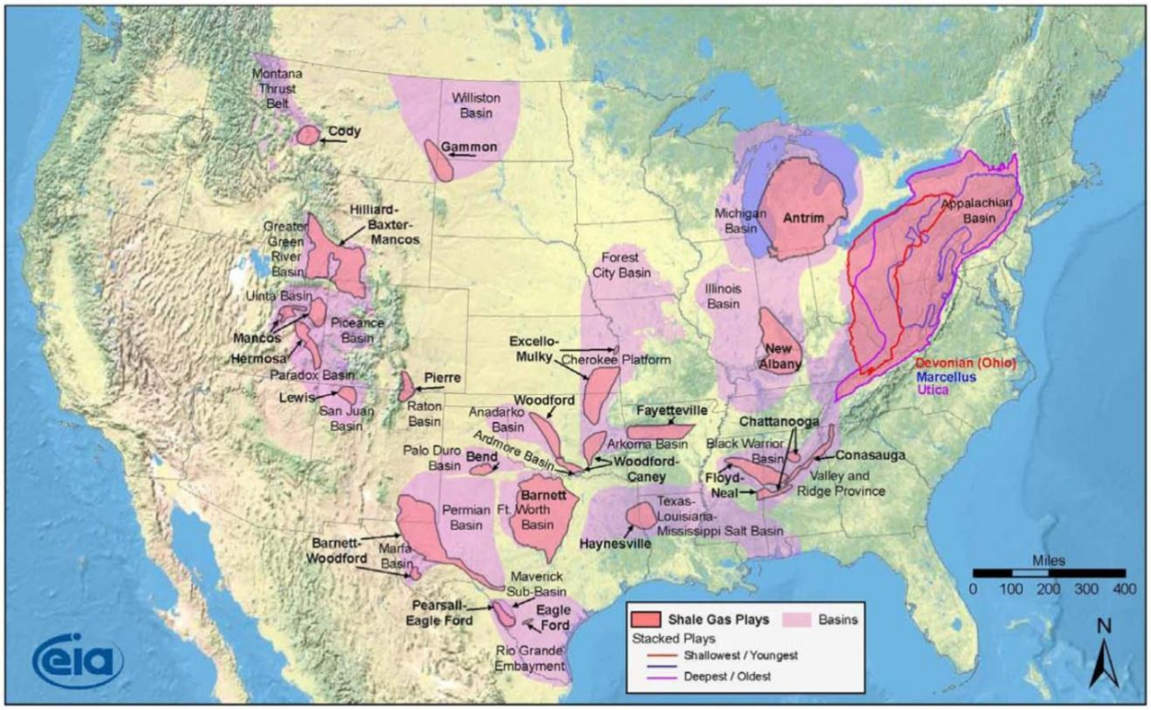

Figure 1. Shale Gas Plays in the U.S. (Energy information Administration, 2010)

Chapter 2

LITERATURE REVIEW

2.1 Naturally Fractured Reservoirs

A significant amount of oil and gas reserves – more than 60% of the world's known conventional oil reserves and 40% of the world's gas reserves (Schlumberger Market Analysis, 2007) – are found in fractured reservoirs. Figure 2 below is a clear example of the existence of subsurface natural fractures. In reservoirs with natural fractures, the opening fractures control fluid flow paths so that the production mechanism in naturally fractured reservoirs is significantly different from that in conventional reservoirs. These natural fractures may close as the reservoir pressure drops, and also influences the growth and final geometry of hydraulic fractures used to enhance production (Lorenz, et al., 1988; Teufel and Clark, 1984). Because natural fractures provide unique characteristics to a reservoir, knowing the properties and geometry of the natural fractures in a reservoir is essential. Precise and detailed information on any pre-existing natural fractures can facilitate the design of optimal recovery processes, such as hydraulic fracturing.

Figure 2. Fractured Woodford Shale in the Arbuckle Mountains of southern Oklahoma (Brian J. Cardott, 2006).

2.2 Fracture Mechanics

Rock mechanics is the theoretical and applied science of the mechanical behavior of rock, that branch of mechanics concerned with the response of rock to the force fields of its physical environment. The mechanical properties and the in-situ stress state of the reservoir rock are important properties in designing a fracture treatment. Knowledge of rock mechanics allows researchers to calculate the deformation and failure behavior of the rock mass induced by the treatment and determination of the fracture's final geometry. The mechanical properties that will be discussed in this section are in-situ stress and elastic properties, which are essential in order to understand the hydraulic fracturing process.

2.2.1 *In-Situ Stress*

In-situ stress is one of the most important factors controlling hydraulic fracturing. Stresses control the width of the fracture, direction of the propagation, and the height growth. In addition, closure pressure, fracture propagation pressure, and instantaneous shut-in pressure are directly related to the minimum in-situ stress. In-situ stresses are often measured through triaxial tests in the lab or formation tests in the field. The level of in-situ stress can also be calculated using the sonic log or laboratory data. Equations 1 and 2 are widely used to estimate the minimum horizontal in-situ stress (σ_{min}) and vertical stress (σ_v).

$$\boldsymbol{\sigma_{min}} = \frac{\boldsymbol{\nu}}{\mathbf{1}-\boldsymbol{\nu}}(\boldsymbol{\sigma}_{\mathbf{ob}} - \boldsymbol{\alpha} \cdot \boldsymbol{p_r}) + \boldsymbol{\alpha} \cdot \boldsymbol{p_r}$$

(Eq. 1)

and

$$\sigma_v = \sigma_{ob} - \alpha \cdot p_r$$

(Eq. 2)

where

σ_{ob} = overburden stress, psi

α = biot's constant, fraction

σ_{min} = minimum in-situ stress

p_r = pore pressure, psi

ν = Poisson's ratio, fraction.

Figure 3 illustrates σ_h, σ_v, and maximum horizontal in-situ stress (σ_H).

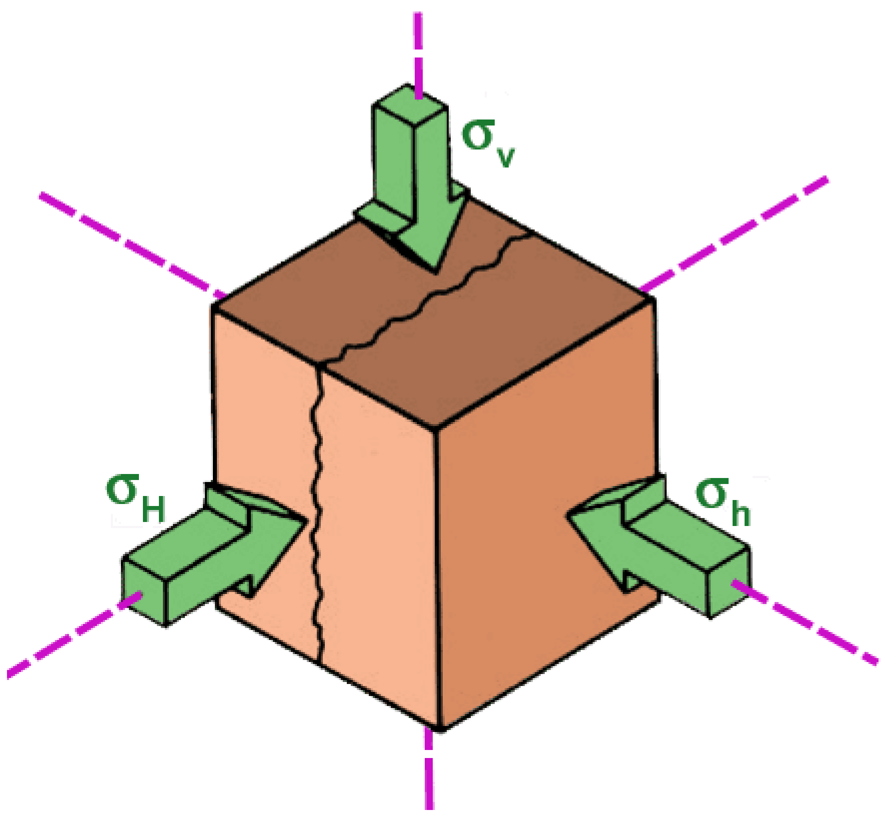

Figure 3. In-situ stresses.

2.2.2 Linear Elastic Fracture Mechanics (LEFM) and Fracture Toughness

The concept of LEFM was introduced by Irwin and explained using stress intensity factors: K_I, K_{II}, and K_{III}, which quantify the intensity of the stress similarity at a fracture tip (Irwin, 1957). LEFM states that a fracture will advance when its stress intensity reaches a critical value, K_{IC}, assuming that the tip is in a state of plane strain.

Irwin classified three different singular stress fields according to the displacement (Figure 4). Mode I is tensile opening, Mode II is in-plane shearing, and Mode III is out-of-plane shearing of the fracture surfaces. For most hydraulic fracturing especially in conventional reservoir without existing natural fractures, only the tensile opening mode happens. This section will therefore be restricted to the effect of K_I.

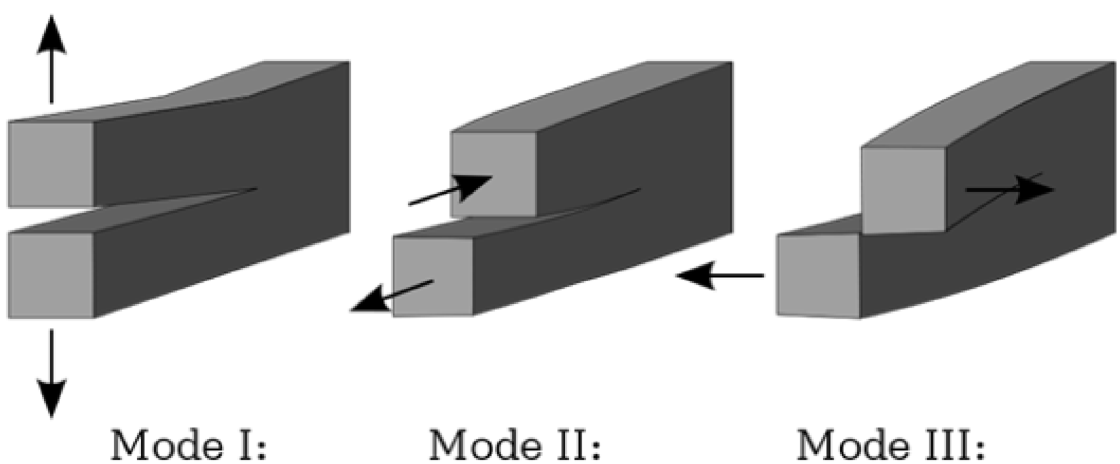

Figure 4. Modes of Fracturing

It can be shown that the stress-intensity factor, K_I, near the fracture tip is related to the applied stresses through the following equation:

$$\begin{Bmatrix} \sigma_x \\ \tau_{xy} \\ \sigma_y \end{Bmatrix} = K_I \frac{K_I}{\sqrt{2\pi a}} cos\left(\frac{\theta}{2}\right) \begin{Bmatrix} 1 - sin\frac{\theta}{2} sin\frac{3\theta}{2} \\ sin\frac{\theta}{2} sin\frac{3\theta}{2} \\ 1 + sin\frac{\theta}{2} sin\frac{3\theta}{2} \end{Bmatrix}$$

(Eq. 3)

where θ is the angle measured from the crack axis, τ_{xy} is the shear stress in the *x*-*y* plane, and r is the distance from a tip of the crack (Rice, 1968).

For a fracture extending from –*a* to +*a* on the *x* axis (propagation direction), Rice show that the Mode I stress-intensity factor can be calculated by

$$K_I = \frac{1}{\sqrt{\pi a}} \int_{-a}^{a} p(t) \sqrt{\frac{a+t}{a-t}}\, dt.$$

(Eq. 4)

In the vicinity of a uniform tensile stress field σ in the *y* direction, the equation easily reduces to

$$K_I = \sqrt{\pi a}\sigma.$$

(Eq. 5)

For failure to occur, this becomes

$$\boldsymbol{\sigma_c} \geq \frac{\boldsymbol{K_{Ic}}}{\sqrt{2\pi a}},$$

(Eq. 6)

where K_{Ic} is fracture(rock) toughness, and σ_c is critical stress. Combining Eqs. 5 and 6, finally gives the criterion for LEFM, for which failure occurs when

$$\boldsymbol{K_I} \geq \boldsymbol{K_{IC}}.$$

(Eq. 7)

Fracture toughness can be measured in the laboratory using several techniques. Some of the most recognized methods involve use of the hollow pressured cylinder, the short rod, the chevron-edge-notched round bar in bending, the Brazilian test and the disc-shaped compact specimen (Guo and Aziz, 1992).

2.3 Models of Hydraulic Fracture

Hydraulic fracturing was first used in the oil and gas industries during the 1930s when Dow Chemical Company discovered that by applying a large enough down-hole fluid pressure, it was possible to deform and fracture rock formations in order to maximize stimulation efficacy (Grebe et al., 1935). At the present time, hydraulic fracturing is extensively used to increase oil and gas productivity and recovery. Numerous treatments are performed each year in a wide range of geological formations, including low-permeability gas fields, weakly consolidated offshore sediments such as the Gulf of Mexico, soft coal beds exploited for methane extraction, naturally fractured reservoirs, and geometrically complex formations.

A hydraulic fracture is created in two phases (Weijers, 1995). First, a fluid called “pad” is injected into the formation. When the down-hole pressure exceeds “breakdown pressure,” a fracture is initiated and then propagates into the formation. The second phase is called the “slurry phase.” A mixture of viscous fluid and proppant is pumped into the formation to extend the fracture and transport the proppants further into the created fracture (Veatch et al., 1989). The geometry of the created fracture is dominated by the rock’s mechanical properties, in-situ stresses, the rheological properties of the fracturing fluid and local heterogeneities such as natural fractures and weak bedding planes (Weijers, 1995).

The process of modeling hydraulic fracturing is complex, not just because of the heterogeneity of the formation properties, but also because of the physical complexities of the problem. It involves three processes: (i) mechanical deformation of the formation caused by the pressure inside the fracture, (ii) fluid flow within the fracture networks, and (iii) fracture propagation (Taleghani, 2009). There are two widely known fracture models: PKN and KGD.

2.3.1 The Perkins, Kern and Nordgren (PKN) model

The PKN model assumes that each vertical strain-plane acts independently, which is equivalent to assuming that the pressure changes along the length of the fracture (Figure 3). This is reasonable if the length is two times greater than the height. In this model, the concentration is on the effect of fluid flow and corresponding pressure gradients.

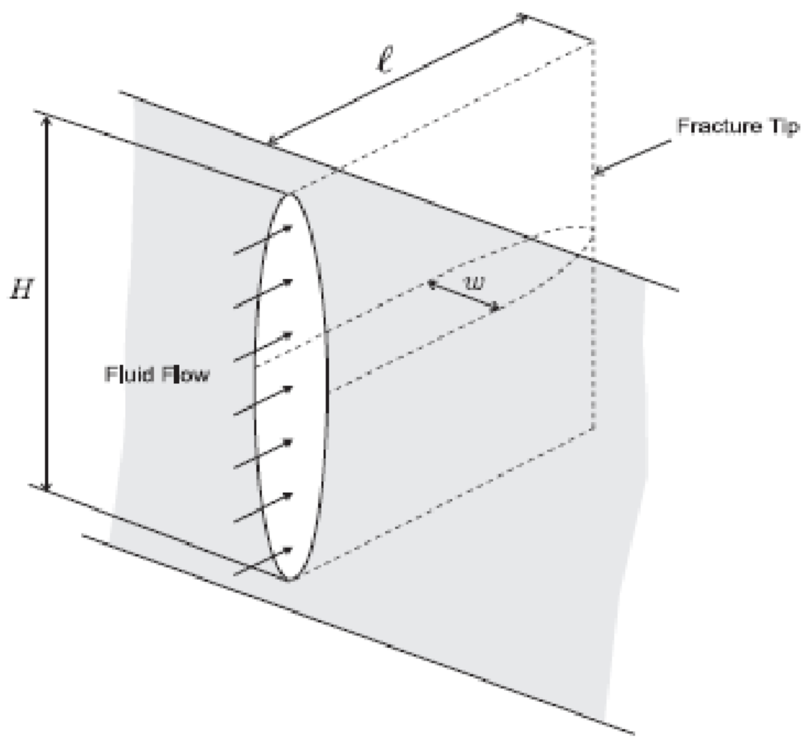

K

Figure 5. Schematic illustration of the PKN fracture model (Taleghani, 2009). The parameters *l*, *H*, and *w* are fracture length, height and width, respectively.

2.3.2 The Khristianovic, Geertsma and de Klerk (KGD) model

In the KGD model, all horizontal strain-plane act independently, which assumes that the fracture width changes along the length direction, not through height. KGD may be reasonably accepted if the fracture height is much greater than the length or if free slip occurs at the boundaries of the pay zone. The KGD model allows the fracture tip to play a more important role. Figure 5 briefly shows how the KGD model works.

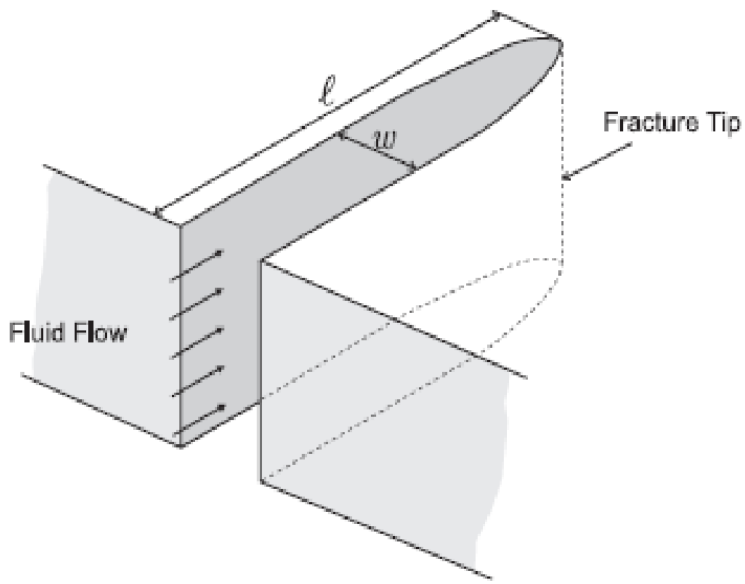

Pe

Figure 6. Schematic illustration of the KGD fracture model (Taleghani, 2009). The parameters *l*, *H*, and *w* are fracture length, height and width, respectively.

2.4 Hydraulic Fracturing in Naturally Fractured Reservoirs

Large amounts of natural gas are stored in unconventional reservoirs, which include tight gas, coal-bed methane, shale gas and natural gas hydrates that have the in-situ gas permeability of a reservoir equal to or less than 0.1 md. In order to recover hydrocarbons from unconventional reservoirs, the use of hydraulic fracturing is a key. The presence of natural fractures in these unconventional gas reservoirs is critical because it provides significant heterogeneity that is needed for stimulation (Aguilera, 2008).

One common observation in naturally fractured reservoirs is a high leakoff rate during hydraulic fracturing. Without natural fractures, the rate of leakoff strongly depends on formation permeability, net treatment pressure and fracture fluid parameters (Valko and Economides, 1995), whereas the presence of natural fractures makes the leakoff rate strongly pressure dependent but not to formation permeability (Baree, 1998). The increase in pressure generated by hydraulic fracturing in a fractured reservoir can open closed natural fracture and causes excessive leakoff so that the leakoff rate in naturally fractured reservoirs is pressure dependent. Therefore, to properly characterize this leakoff and the fracture geometry of a reservoir, it is critical to incorporate the interaction between a hydraulic fracture and pre-existing natural fractures.

Various authors have published analytical models for predicting the behavior of an induced fracture when it interacts with natural fractures. Blanton (Blanton, 1986) and Warpinski and Teufel (Warpinski and Teufel, 1987) derived fracture interaction criteria related to differential stress and the angle of approach. Renshaw provided a criterion for crossing unbounded interfaces (Renshaw and Pollard, 1995). In this section, I will review the above authors' analytical interaction criteria.

2.4.1 Blanton's criterion

Blanton (Blanton, 1986) developed a simple analytical fracture interaction model related to differential stress (Figure 7),

$$\boldsymbol{Differential\,Stress} = \boldsymbol{\sigma_1} - \boldsymbol{\sigma_3}$$

(Eq. 8)

and angle of approach, θ (Figure 7), by extrapolating the laboratory results to field simulations.

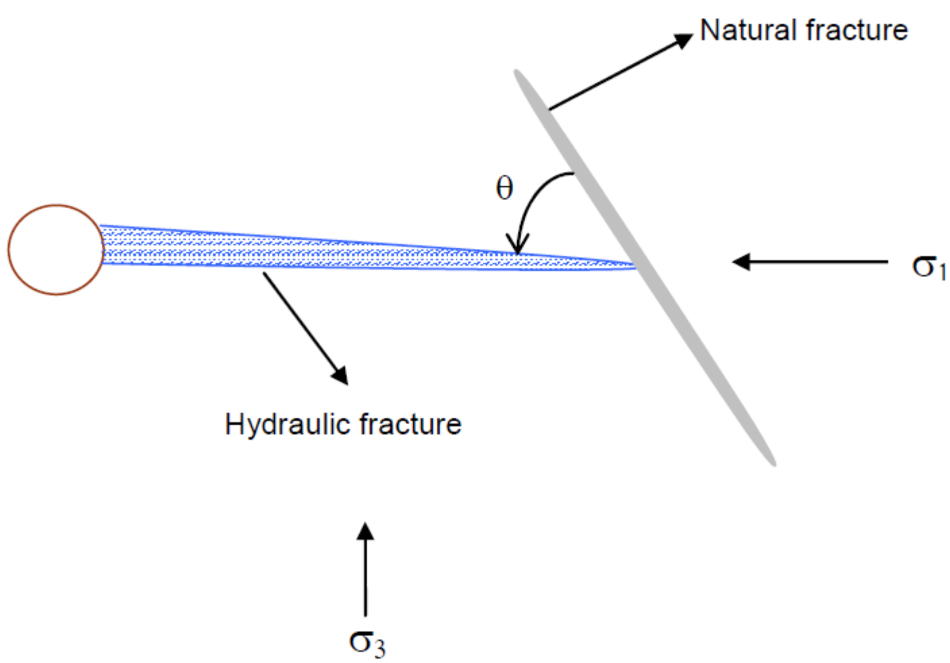

Figure 7. A hydraulic fracture intersecting a natural fracture (Potluri and Zhu, 2005).

Blanton's criterion can be summarized as follows: opening will occur if the fracture fluid pressure at the intersection point exceeds the normal stress, σ_n, acting on the natural fracture. Crossing will occur when the pressure required for re-initiation is less than the opening pressure. In mathematical form the criterion for crossing can be written as:

$$\boldsymbol{p > \sigma_t + T_o}$$

(Eq. 9)

and for opening as:

$$\boldsymbol{p > \sigma_n}$$

(Eq. 10)

where '*p*' is the pressure inside the fracture, σ_n is the normal stress acting on the plane of the natural fracture, σ_t is the stress acting parallel to the natural fracture and T_o is the tensile stress of the rock. The final equation for crossing, the combination of the equations above and the angle of approach, is given by Blanton as:

$$\boldsymbol{\frac{\sigma_1 - \sigma_3}{T_o} > \frac{1}{cos\ 2\theta - b\ sin 2\theta}}$$

(Eq. 11)

where

$$\boldsymbol{b = \frac{1}{2a}\left\{v(x_0) - \frac{x_o - l}{K_f}\right\}}.$$

$$\boldsymbol{v(x_0) = \frac{1}{\pi}\left\{(x_0 + l)\ln\left(\frac{x_o + l + a}{x_o + l}\right)^2 + (x_0 - l)\ln\left(\frac{x_o - l - a}{x_o - l}\right)^2 + \mathbf{c}\ln\left(\frac{x_o - l - a}{x_o - l}\right)^2\right\}}$$

(Eq. 12)

and

$$\boldsymbol{x_0 = \left\{\frac{(1 + a)^2 + e^{\frac{\pi}{2K_f}}}{1 + e^{\frac{\pi}{2K_f}}}\right\}^{\frac{1}{2}}}$$

(Eq. 13)

where 'a' is the length of the zone of slippage, the region from $-l$ to $+l$ is the open section of the natural fracture as shown in Figure 8, θ is the angle of approach, and K_f is the coefficient of friction.

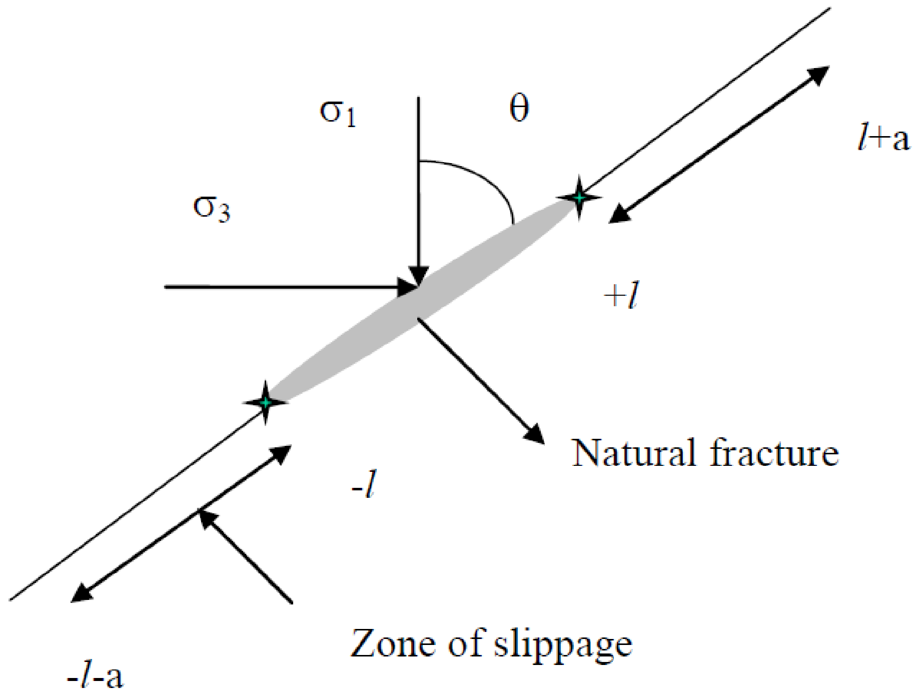

Figure 8. Zone of slippage for a natural fracture (Potluri and Zhu, 2005)

2.4.2 Warpinski and Teufel's criterion

Warpinski and Teufel (Warpinski and Teufel, 1987) built up an interaction criterion to predict whether the induced fracture causes shear slippage on the natural fracture plane leading to arrest of the propagating fracture or opens the natural fracture, causing excessive leakoff. According to Warpinski and Teufel, shear slippage occurs if the amount of normal stress acting on the plane of the natural fractures is not enough to prevent the planes from sliding against each other. Following a linear friction law (Jaeger and Cook, 1976), the mathematical relationship between the shear stress and normal stress acting on the natural fracture plane is given as

$$|\tau| = \tau_0 + K_f(\sigma_n - p)$$

(Eq. 14)

where τ_0 is the inherent shear strength of the natural fracture plane. As a result, according to Warpinski and Teufel's criterion shear slippage occurs when

$$|\tau| > \tau_0 + K_f(\sigma_n - p)$$

(Eq. 15).

As shown in Figure 9,

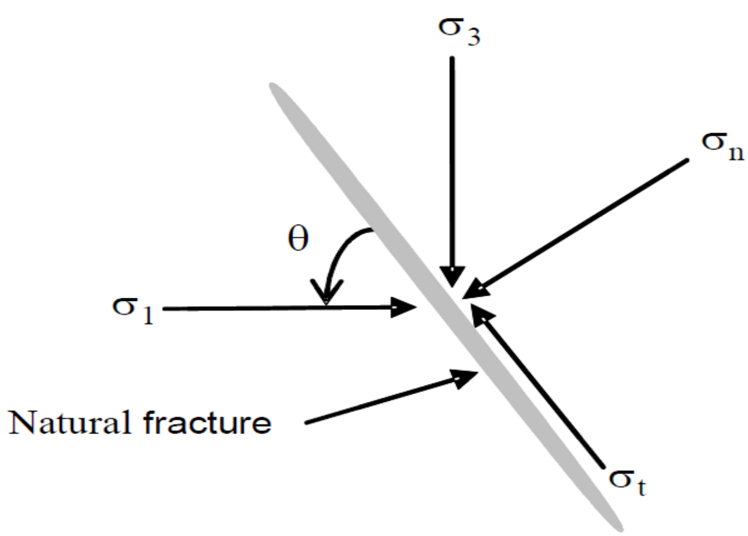

Figure 9. Stress resolution in the natural fracture plane (Jaeger and Cook, 1976)

τ can be written as

$$\tau = \frac{\sigma_1 - \sigma_3}{2} sin2(90 - \theta)$$

(Eq. 16)

such that final equation for shear slippage can be written as

$$(\sigma_1 - \sigma_3) > \frac{2\tau_0 - 2(P - \sigma_3) K_f}{sin2\theta + K_f cos2\theta - K_f}$$

(Eq. 17).

2.4.3 Renshaw's criterion

Renshaw (Renshaw and Pollard, 1995) generally proposed that the simplified version combines Blanton's and Warpinski and Teufel's criteria. Renshaw's criterion is similarly based on use of the linear elastic fracture mechanics solution for the stresses near the fracture tip to determine the stresses required to prevent slip along the interface at the moment when the stress on the opposite side of the interface is sufficient to reinitiate a fracture. Mathematically, this is given as

$$\frac{-\sigma_3}{T_o - \sigma_1} > \frac{0.35 + \frac{0.35}{K_f}}{1.06}$$

(Eq. 18)

The above criterion is restricted to orthogonal interactions and assumes that the frictional interface does not alter the direction of fracture propagation.

2.5 Existing Simulation Methods

In this section, I will discuss three recent models which takes account of the effect of pre-existing natural fractures. Modeling approach, advatages and disadvantages for each will be summarized.

2.5.1 Zhang *et al.*'s 2D model

Zhang (Zhang et al., 2007) and his group have developed a 2D hydraulic fracture model using the Discrete Discontinuity Method(DDM) technique (Crouch and Starfield, 1983), which considers the criteria outlined above and includes elastic rock deformation coupled to both fluid flow and frictional slippage. In the model, discretization is only performed along the fractures. To improve the accuracy of these calculations, the model employs a mesh adaptive scheme which re-applies discretization as the fracture grows (Figure 10).

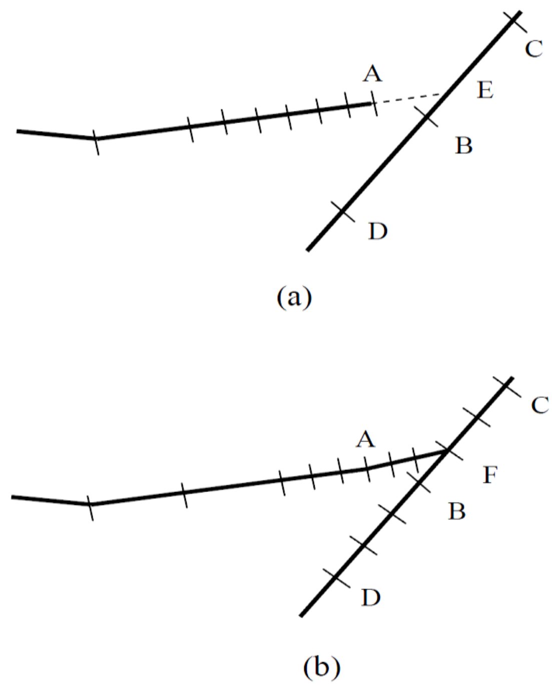

Figure 10. Schematic for the process of fracture coalescence (Zhang *et al.*, 2007). (a) Prior to coalescence and (b) post coalescence.

Since only fracture itself is discretized and updated through the Finite Difference Method (FDM), reservoir property influences the model only slightly. In other words, simulation performed in different reservoir conditions such as a low-permeability environment with a complex pre-existing fracture network would not be suitable for this model. In addition, this model does not allow for the visual representation of fracture geometry.

2.5.2 Weng *et al.*'s Unconventional Fracture model (UFM)

A new hydraulic fracture model was developed by Weng's group (Weng *et al.*, 2011) to simulate the propagation of complex fracture networks in a formation with pre-existing natural fractures. Similar to Zhang's model, this model solves a system of equations governing fracture deformation in a complex fracture network with multiple propagating fracture tips. Fracture height growth is modeled in the same manner as in conventional pseudo-3D models. Figure 11 illustrates the flow chart of UFM, and Figure 12 shows an example of the fracture geometry generated by UFM simulation. This model looks quite advanced and practical but has critical limitations: UFM is not fully coupled with reservoir simulation and fracture propagation was simplified. Various reservoir property changes such as pressure changes, which occur continuously during the hydraulic fracture process, cannot be calculated with UFM.

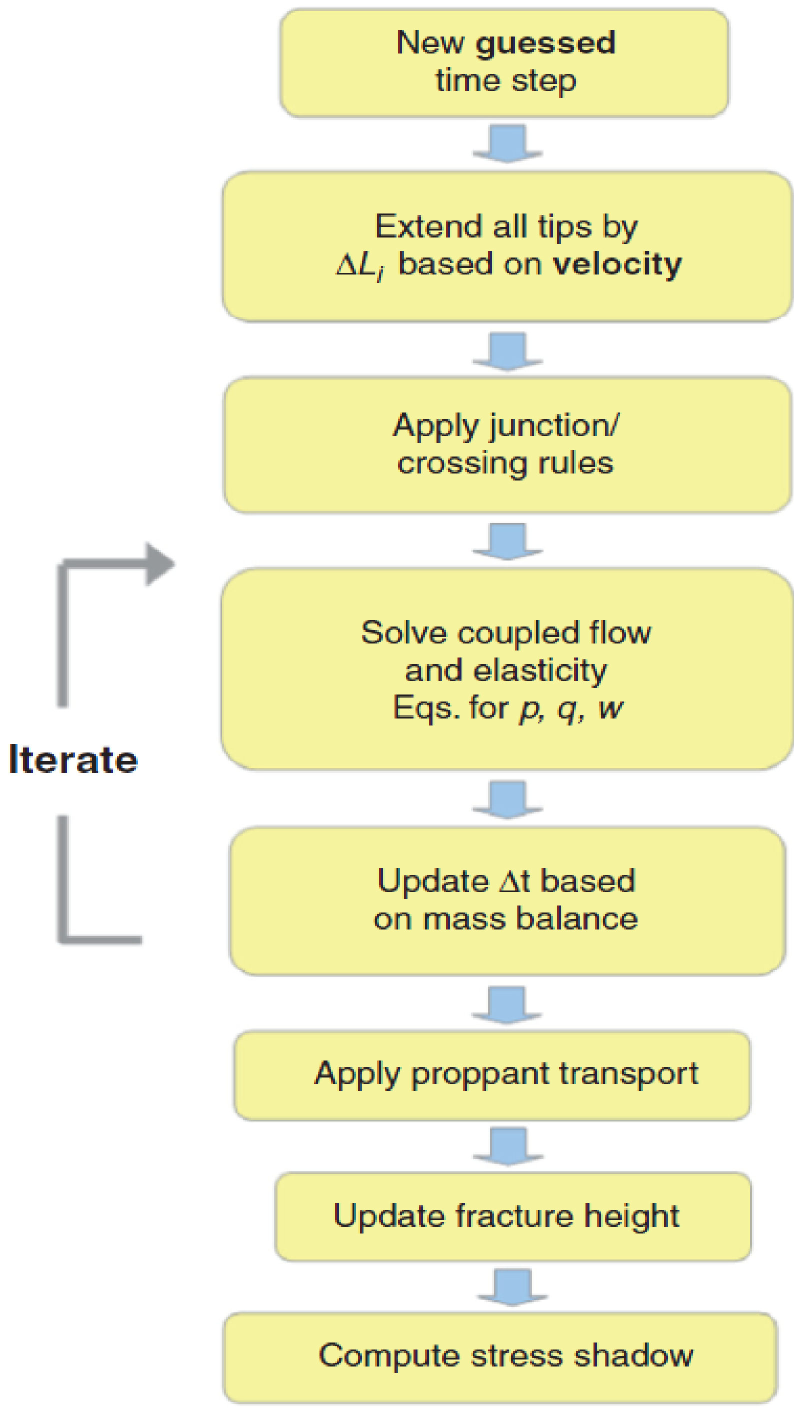

Figure 11. Structure of the propagation-solution loop (Weng *et al.*, 2011).

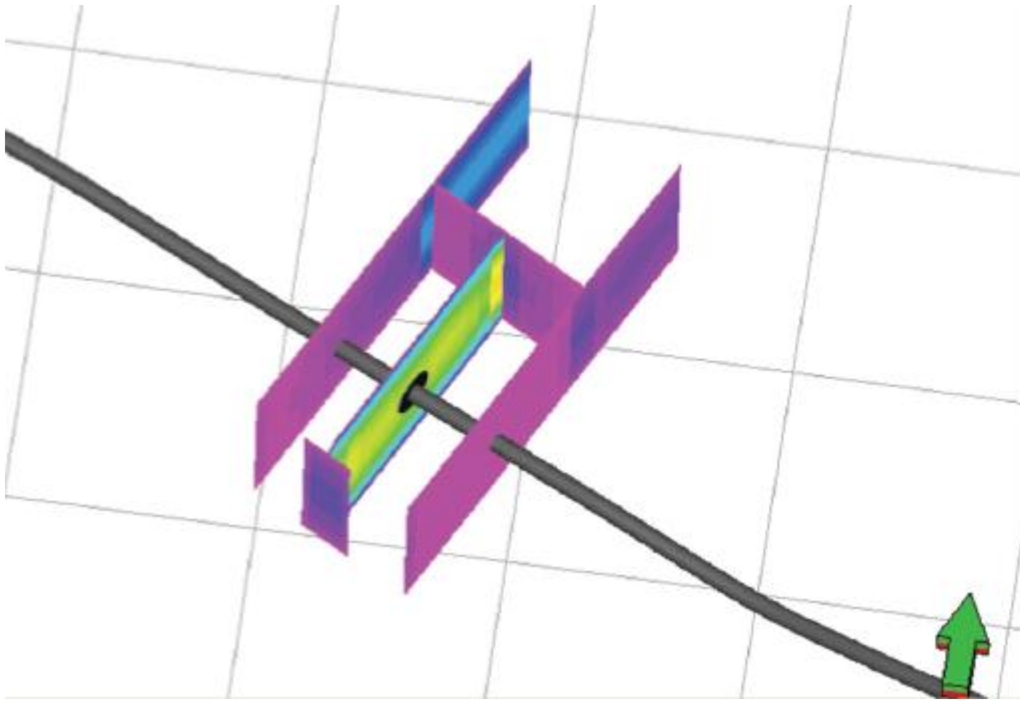

Figure 12. Fracture geometry as modeled using UFM (Weng *et al.*, 2011).

2.5.3 Keshavarzi *et al.*'s Extended Finite Element Method (XFEM)

The most notable advantage provided by the use of XFEM is the fact that fracture propagation can be modeled without any grid refinement. Furthermore, the difficulties of the conventional finite element method do not exist in simulations modeled by the extended finite element, because the crack is not modeled as a geometric entity and does not need to conform to element edges (Keshavarzi *et al.*, 2012). Figure 13 shows examples of the XFEM simulation results. However, this method has not yet been proven for the complex fracture network using multiple fracture propagations as provided by the UFM.

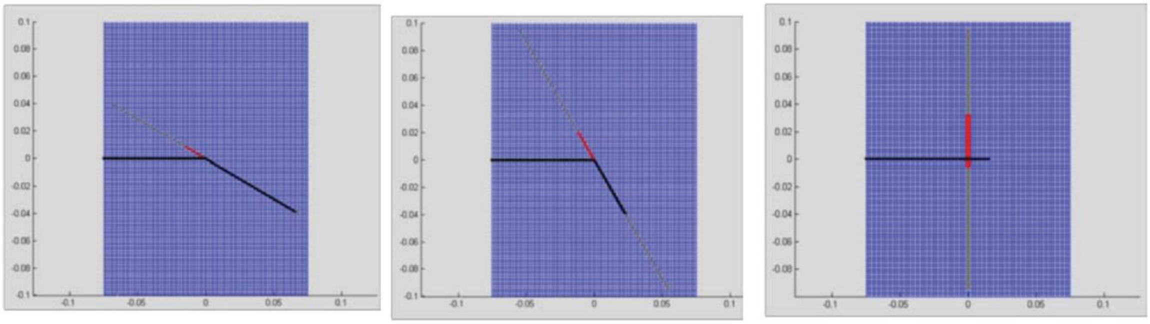

Figure 13. Fracture geometry as predicted by XFEM (Keshavarzi *et al.*, 2012).

In summary, none of the available models, either commercial or in academia, is able to capture the complexity of hydraulic fracture propagation, fracture fluid leakoff, proppant transport, fracture fluid flowback and fracture closure, and then long-term oil and gas recovery in shale oil and gas reservoirs. In this research, I plan to build an advanced, coupled hydraulic fracture simulation model to account for the complexity of fracture propagation and fluid leakoff in shale reservoirs. Model development will be discussed in details in chapter 3.

Chapter 3

MODEL DEVELOPMENT

In the traditional decoupled fracturing models, such as PKN and KGD, the fracture propagation is modeled based on the mass balance of injected fracture fluid and an analytical fluid leakoff model. However, integrated hydraulic fracture propagation models generally require the fully coupled simulation of reservoir fluid flow, hydraulic fracture propagation, fluid leakoff, and resultant stress change through a stationary reservoir/stress grid. This coupled method takes into consideration the mutual influence between dynamic fracture propagation and reservoir flow, treat the fracture as a part of the reservoir, and use one grid system to model both dynamic fracture propagation and reservoir flow in a fully coupled manner. Furthermore, as discussed above, most shale gas reservoirs have pre-existing natural fractures that strongly impact the propagation of hydraulic fractures. In this chapter, we demondtrate a methodology to build a coupled, 2-diemnsional, 1-phase numerical model for simulating dynamic hydraulic fracture propagation, its interaction with existing natural fracture, and fracture fluid leakoff in shale gas reservoirs. Our model will be a finite difference model for both fracturing and reservoir simulation. This chapter has the following four sections:

- 3.1 Discretization
- 3.2 Fluid flow modeling
- 3.3 Hydraulic Fracture Modeling
- 3.4 Coupling Procedure

3.1 Discretization

The modeling starts with the construction of a grid system. In order to include all of the relevant physics, such as natural fracture effect on the fracture propagation, local grid refinement (LGR) technique needs to be integrated into our gridding module. Depending on the location, density, and length of natural fractures, and the hydraulic fracture initiation point, LGR is implemented for the accurate modeling of dynamic fracture propagation. Figure 14 is the flowchart for building a grid system, which was coded in Matlab into a gridding module in my model.

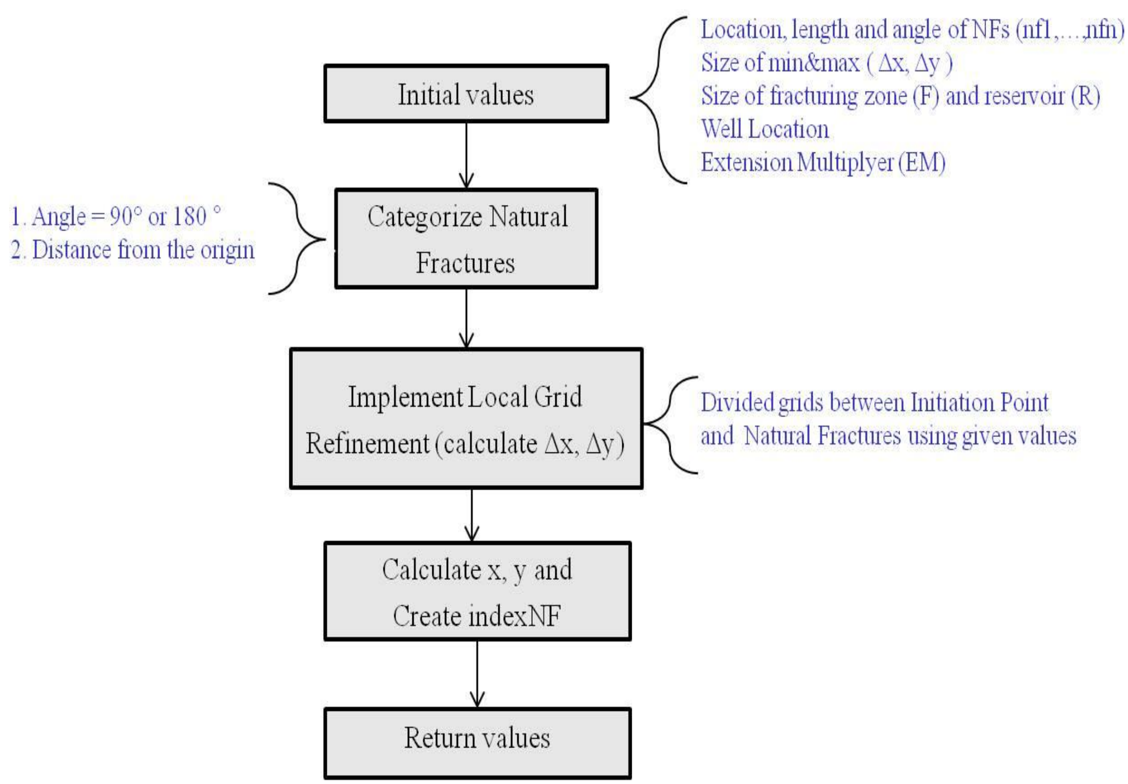

Figure 14. Flowchart of the algorithm for gridding module.

As shown in Figure 14, gridding module discretizes the reservoir by using the parameters representing the sizes of minimum and maximum grid blocks, the size of the fracture zone and reservoir, the well location, and the grid-size increment factor. Figure 15 presents an example of a discretized reservoir generated by using gridding module. In figure 15, the minimum grid block size in both x and y directions are 0.003 ft and the size of the fracture zone is 0.03 ft such that there are ten grids in the fracture zone (0.03/0.003 = 10).

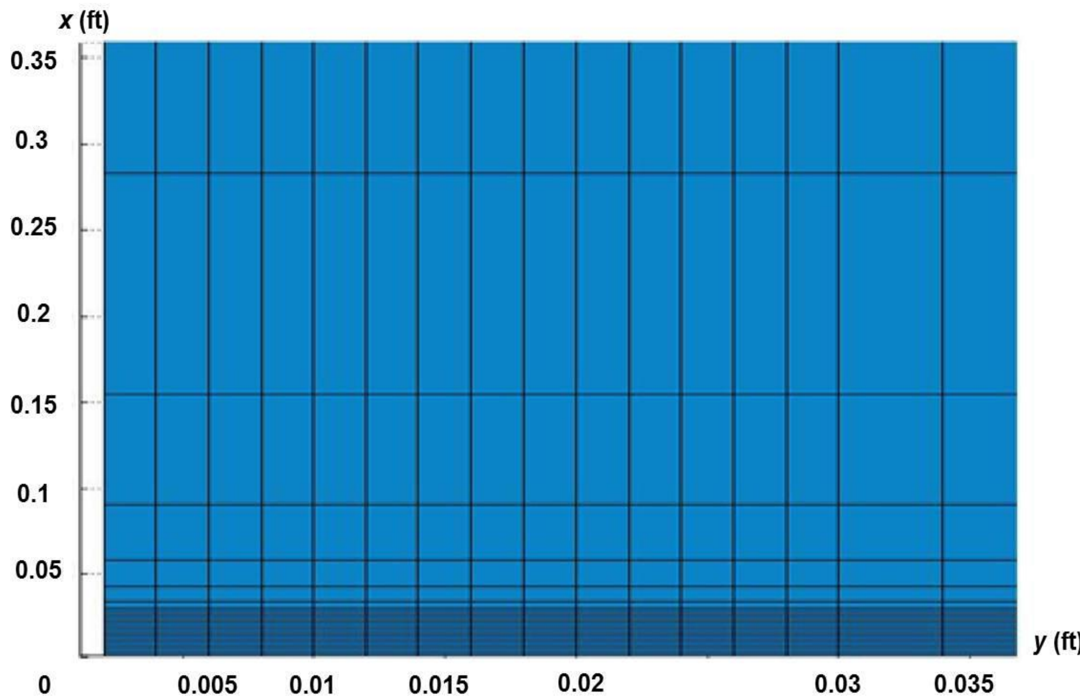

(a) Zoomed view near the hydraulic fracturing path

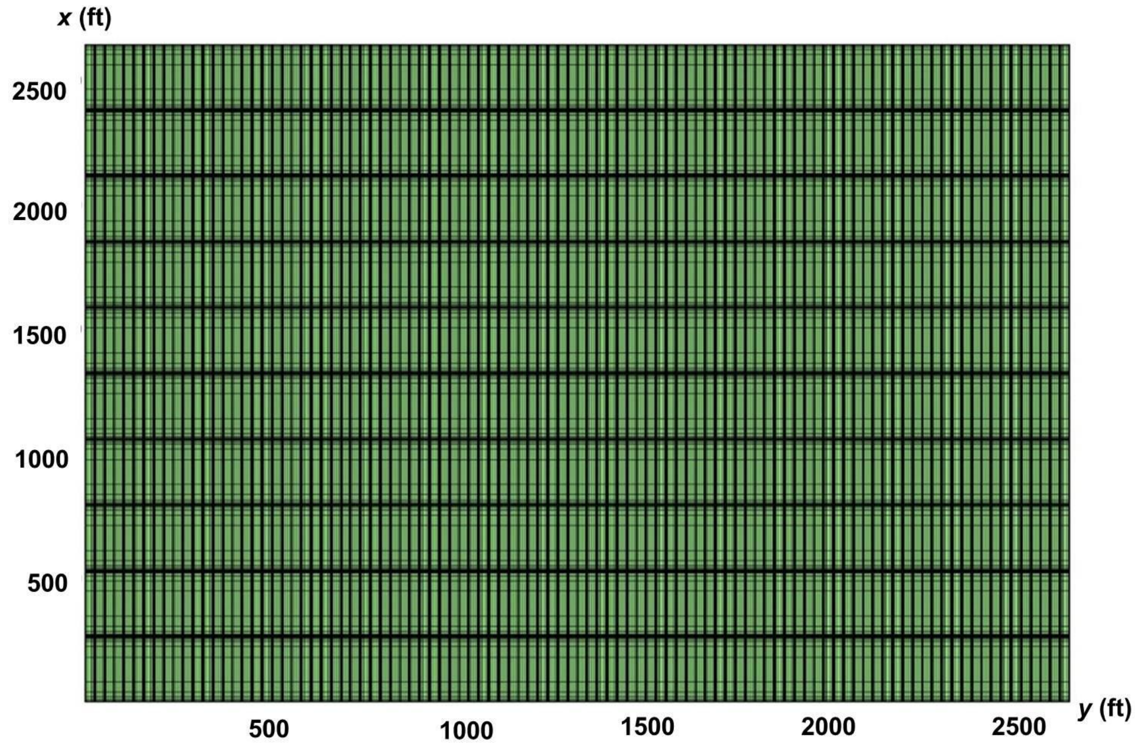

(b) Overall view of a reservoir

Figure 15. An example of a discretized reservoir as modeled using the LGR module. (a) Zoomed version of the LGR near the hydraulic fracturing path. (b) Overview of the 100x10 (*x*x*y*) LGR implemented.

Figure 15 (a) represents a zoomed version near the hydraulic fracturing zone. In this figure, the size of fracture zone is chosen to be 0.03 feet such that 10 minimum size grid blocks with 0.003 feet are located at the fracture zone. Beyond the fracture zone, grid block size begins to increase along with *x* direction by the increment factor 2 until the grid block size reaches maximum grid block size of 10 feet. Therefore, the result Figure 15 (a) is generated. Figure 15 (b) shows overall view of the reservoir. There are 10 existing natural fractures in *x* direction with a spacing of every 264 feet and 100 existing natural fractures in *y* direction with a spacing of every 26.4 feet. LGR is applied to the grids surrounding each existing nature fracture, as shown in zoomed

Figure 15 (a). The smallest grid inside the fracture zone of an existing or created fracture is 0.003 feet.

3.2 Fluid flow modeling

The fluid flow model is a 2-dimensional, 1-phase of slightly compressible or compressible black-oil system. The assumptions made for the reservoir flow in our model includes:

- Slightly compressible Newtonian flow, or compressible fluid
- 1-phase flow,
- 2-diemensional flow,
- Isotropic permeability.

In most of the fracture treatments in shale gas reservoirs, slickwater is used as a fracturing fluid. Slickwater has fairly identical rheological properties with water. We assumed the fluid used in our model to be water which is slightly compressible Newtonian fluid. Because the gas component is assumed to be immiscible in water, it is also reasonable to incorporate 1-phase flow into our model. In addition, shale gas reservoirs have extremely low permeability and was assumed isotropic permeability. At last, 2-dimensional flow is assumed by neglecting the flow in the *z* direction to have a faster simulation and to focus on the horizontal fracture propagation.

The general form of mass-conversion equation for the single component for two dimensional flow of the black-oil system is

$$-\frac{\partial}{\partial x}(\dot{m}_{cx}A_x)\Delta x-\frac{\partial}{\partial y}\left(\dot{m}_{cy}A_y\right)\Delta y=V_b\frac{\partial}{\partial t}(m_{vc})-q_{mc}$$

(Eq. 19)

where;

$\dot{m}_{cx}$ = mass flux for component c along the x, y and z direction, lbm/D-ft^2

m_{vc} = mass of component c per unit volume of rock, lbm

A = cross sectional area,ft^2

q_{mc} = rate of mass depletion for component c through injection, lbm/D

V_b = grid block bulk volume.ft^3

Darcy's law for single-phase flow may be substituted into the mass-conservation equation (Eq. 19) to obtain the following fluid (water)-flow equation.

$$\frac{\partial}{\partial x}\left[\beta_c K_x A_x \frac{K_r}{\mu_w B_w}\left(\frac{\partial p_w}{\partial x} - \gamma_w \frac{\partial Z}{\partial x}\right)\right]\Delta x + \frac{\partial}{\partial y}\left[\beta_c K_y A_y \frac{K_{rw}}{\mu_w B_w}\left(\frac{\partial p_w}{\partial y} - \gamma_w \frac{\partial Z}{\partial y}\right)\right]\Delta y = \frac{V_b}{a_c}\frac{\partial}{\partial t}\left(\frac{\varphi S_w}{B_w}\right) - q_{wsc}$$

(Eq. 20)

where;

k = permeability in the x, y and z direction, md

k_r = relative permeability, md

μ = viscosity, cp

B = FVF (or constant), RB/STB

Φ= porosity, fractional

γ = gravity of phase, psi/ft

R_s = solution GOR/GWR in Grid block n, scf/STB

S_w = saturation of water, fractional

β_c = transmissibility conversion factor,

a_c = volumetric conversion factor.

In order to solve the flow equation above (Eq. 20), numerical methods were applied to obtain an engineering solution. The finite-difference approach was used to obtain the numerical solution for our flow system. With this approach, the flow equations are discretized by the use of algebraic approximations of the second-order derivatives with respect to space and the first-order derivatives with respect to time. Depending on the approximation of the derivatives with respect to time, implicit finite-difference equations may be chosen for the numerical simulation. In our model, the strong implicit procedure (SIP) method is used for solving the flow equation to obtain pressures for each grid block at each time step.

3.3 Hydraulic Fracture Modeling

The stress fields determine how fractures might propagate. The actual propagation is calculated using criteria from linear elastic fracture mechanics (LFEM). Fracture propagation in LEFM is a function of opening and shearing modes stress intensity factors (K_I and K_{II}), which measure stress concentration at the tip of the fracture (Lawn, 2004). However, the shearing mode stress intensity factor is often neglected because its contribution to fracture propagation is relatively small compared to the opening mode. Thus, in my model, fracture propagates normal to the minimum principal in-situ stress(σ_h) using the critical intensity factor of only K_{Ic}. Minimum in-situ stress(σ_h) is also assumed to be perpendicular to the y-axis so that hydraulic fracture propagates from the origin along the y-axis. In addition, minimum and maximum in-situ stresses (σ_h and σ_H) are variables that depend on the initial stress field and the reservoir pressure. The changes in σ_h and σ_H are generally complex and vary along the fracture. However, in first approximations, changes in σ_h and σ_H can be assumed to depend on the change in average reservoir pressure Δp according to;

$$\Delta\boldsymbol{\sigma}_{\boldsymbol{h\ or\ H}} = \boldsymbol{\alpha}\frac{\mathbf{1}-\mathbf{2\nu}}{\mathbf{1}-\boldsymbol{\nu}}\Delta\boldsymbol{p}$$

(Eq. 21)

where,

α = poroelastic biot's constant, fraction

ν = Poisson's ratio, fraction

$\Delta\sigma_{h\ or\ H}$ = difference of *in-situ* stresses with respect to time, psi

(h = minimumprinciple, H = maximumprinciple)

Δp = difference of reservoir pressure with respect to time, psi

Depending on the above in-situ stresses, complex fracture behavior is modeled using one of the three modules presented below: the fracture initiation module, propagation module, or width module.

3.3.1 Fracture Initiation Module

A fracture is initiated as soon as fracture fluid pressure in the initiation block (wellbore) reaches the fracture initiation pressure or breakdown pressure of

$$\boldsymbol{p_{breakdown} = p_{initiation} = \sigma_{h,min} + \frac{K_{IC}}{\sqrt{12\pi L_f}}},$$

(Eq. 22)

where $\sigma_{h,min}$ is initial minimum insitu stress in psi, L_f is initial fracture half-length (0.72 in. used for this study), and K_{IC} is rock toughness (a critical intensity factor of mod I). To simulate $p_{breakdown}$, L_f was 0.005 to 0.06 ft in all the numerical experiments in this research. However, in real life, $p_{breakdown}$ should be measured frome pre-fracture field test first and then put into our model. Fracture not only initiates from the wellbore but can also be initiated from the body of any fracture to create a new fracture tip. Using Eq. 22, a new fracture can be created using any grid block representing fracture body or injection point (initiation point); therefore, initiation criteria can be derived as:

$$p_{@i,j} \geq p_{initiation@i,j} = \sigma_{h,min@i,j} + \frac{K_{IC@i,j}}{\sqrt{12\pi L_{f@ini}}}$$

(Eq. 23)

where,

$p_{@i,j}$ = fracture fluid pressure at the grid block i, j , psi

$p_{initiation@i,j}$ = initiation pressure at the grid block i, j , psi

$\sigma_{h,min@i,j}$ = minimum horizontal *in-situ* stess at the grid block i, j , psi

$K_{IC@i,j}$ = rock toughness or critical intensity factor for mod I at the grid block i, j , psi-in$^{0.5}$

$L_{f@ini}$ = fracture half-length for initiation (often twice the wellbore raidus), in.

In conventional hydraulic fracture models without natural fractures, initiation occurs only at the wellbore and the tip of the fracture; however, in our complex network model, initiation criteria needs to considered along the fracture face for a possible new fracture creation.

3.3.2 Fracture Propagation Module

During the fracture propagation, the pressure at the tip of fracture is assumed equal to the fracture propagation pressure of:

$$p_{propataion} = (\sigma_{h\ or\ H}) + \frac{(K_{ICm}\ or\ K_{ICnf})}{\sqrt{\pi L_f}}$$

(Eq. 24)

where K_{ICm} is rock toughness of the matrix and K_{ICnf} is rock toughness of the natural fracture, which is treated as zero in this model. Depending on σ_h, σ_H, K_{ICm}, and K_{ICnf}, we can have a maximum of four propagation pressures that govern the direction of propagation at the fracture tip. The amount of propagation pressure to consider is determined by the existence of natural fracture at the tip grid block. Among these propagation pressures, fracture is always considered as propagates in the direction of the minimum propagation resistance, because this parameter represents the least energy required for the fracture to extend. Equation 25 shows potential values for the propagation pressure at the tip and the propagation criteria.

$$\boldsymbol{p_{tip@i,j}} \geq \boldsymbol{p_{propataion@i,j} = min\left\{\begin{pmatrix} \sigma_{h@i,j} + \dfrac{K_{ICm@i,j}}{\sqrt{\pi L_{f@i,j}}} \\ \sigma_{H@i,j} + \dfrac{K_{ICm@i,j}}{\sqrt{\pi L_{f@i,j}}} \\ \sigma_{h@i,j} + \dfrac{K_{ICnf@i,j}}{\sqrt{\pi L_{f@i,j}}} \\ \sigma_{H@i,j} + \dfrac{K_{ICnf@i,j}}{\sqrt{\pi L_{f@i,j}}} \end{pmatrix}\right.}$$

(Eq. 25)

where,

$p_{tip@i,j}$ = pressure at the tip grid block i, j, psi

$p_{propagation@i,j}$ = propagation pressure at the grid block i, j, psi

$\sigma_{h@i,j}$ = minimum horizontal *in-situ* stess at the grid block i, j, psi

$\sigma_{H@i,j}$ = maximum horizontal *in-situ* stess at the grid block i, j, psi

$L_{f@i,j}$ = fracture half-length for initiation at the grid block i, j,in.

Because this model deals with heterogeneous rock toughness due to the natural fractures, the least propagation pressure requirement is not necessarily perpendicular to σ_h, and as such direction may change while fracture extends. Depending on which of σ_h or σ_H is governing the minimum propagation pressure, fracture grows perpendicular to σ_h or σ_H as illustrated in the Figure 16.

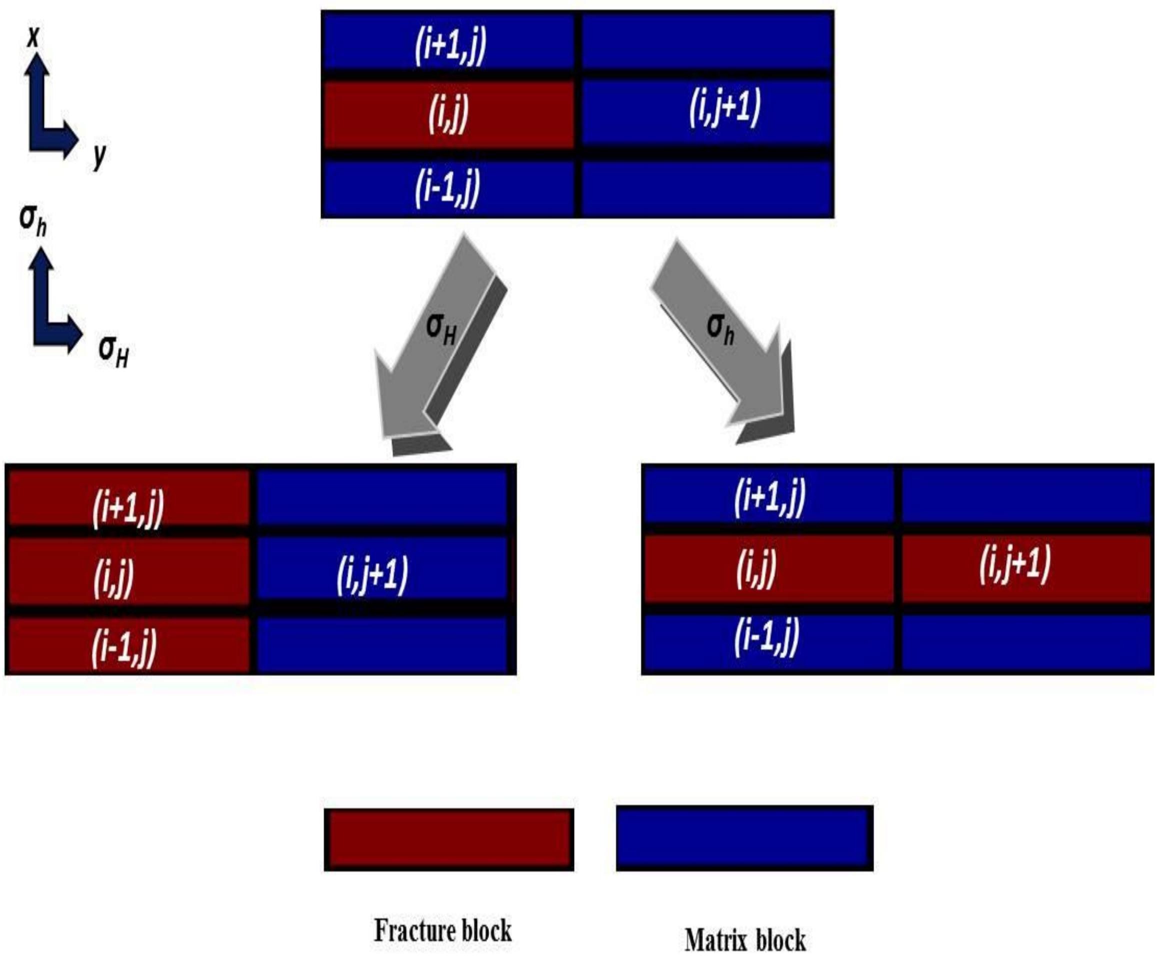

Figure 16. A schematic representation of the fracture propagation process.

3.3.3 Width Expansion Module

The fracture width at each fracture grid block is determined by the fluid pressure inside the grid block and its governing in-situ stress as following equation with the assumption of vertical plane-strain theory.

$$\boldsymbol{w(x,y,z,time)} = \frac{\boldsymbol{(1-\nu)h_f(p_f-\sigma_{h\ or\ H})}}{\boldsymbol{G}}$$

(Eq. 26)

where w is width in ft, p_f is fluid pressure in psi, ν is Poisson's ratio of rock formation, and G is the shear modulus of rock formation in psi. If the fracture propagates perpendicular to σ_h the width will grow parallel to the σ_h direction with the amount of w calculated using σ_h as in Equation 26. The width of a fracture extending perpendicular to σ_H can be calculated similarly using σ_H in Equation 26. Thus, width implementation in the discretized formation can be derived using the following two criteria:

$$\boldsymbol{dx(i,j)+2dx(i+1,j)} \le \boldsymbol{w(i,j)} = \frac{\boldsymbol{(1-\nu)h_f\left(p_f(i,j)-\sigma_h(i,j)\right)}}{\boldsymbol{G}},$$

(Eq. 27)

$$\boldsymbol{dy(i,j)+2dy(i,j+1)} \le \boldsymbol{w(i,j)} = \frac{\boldsymbol{(1-\nu)h_f\left(p_f(i,j)-\sigma_H(i,j)\right)}}{\boldsymbol{G}}$$

(Eq. 28)

where,

$dx(i,j)$ = x direction length at the grid block i, j, ft

$dy(i,j)$ = y direction length at the grid block i, j, ft

Equations 27 and 28 both assumes symmetrical neighboring grid block size along the x and y axes. An example of width implementation using Equation 27 is displayed in Figure 17 below.

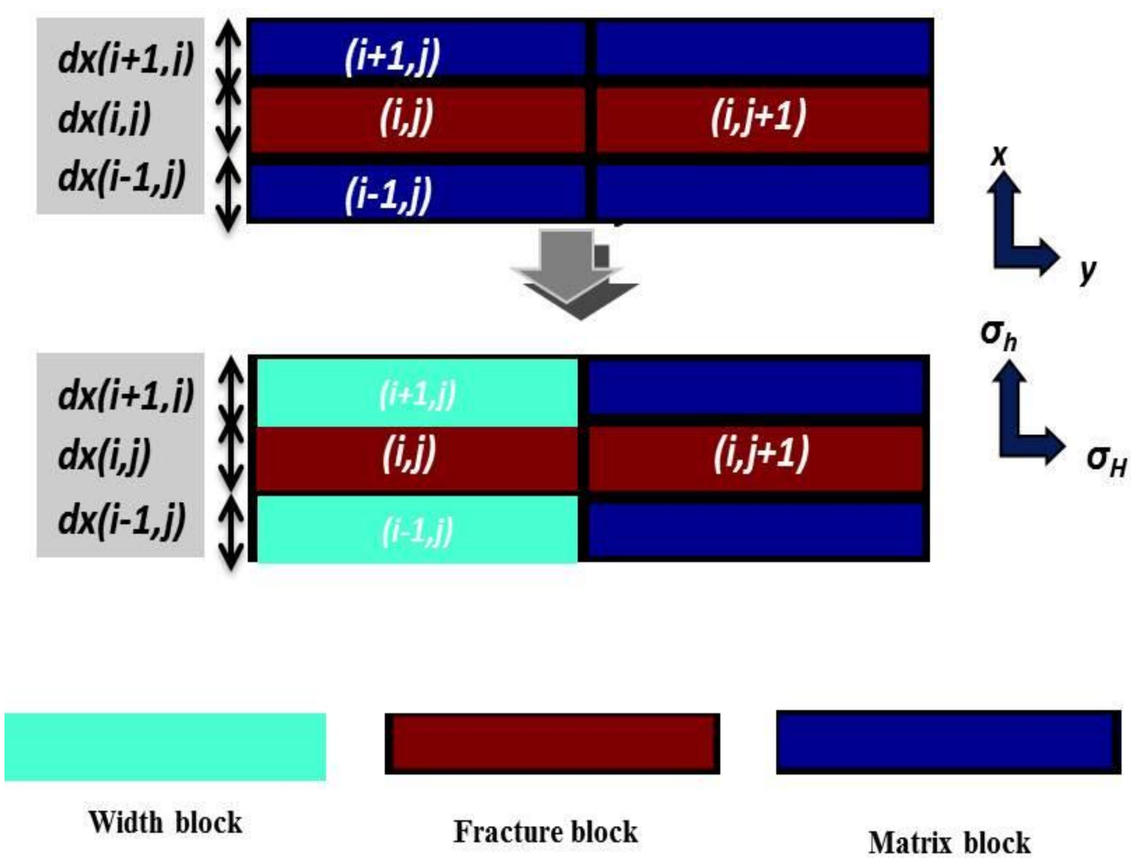

Figure 17. A schematic representation of width expansion.

As shown in Figure 17, width block and fracture block needs to be treated separately because the width calculation in this model is designed to be calculated only at the fracture block created by the propagation or initiation module. In other words, the application of width calculation to every width block will result in infinite width expansion; thus, different indices must be assigned to various width blocks.

3.4 Coupling Procedure

The coupled simulation of reservoir fluid flow and fracture propagation treats the fracture as a highly permeable part of the reservoir matrix, so only one common grid system is used to model both the reservoir flow and the propagating fracture. The procedure starts with the injection of fracturing fluid into the reservoir and the determination of pressure at different time steps for all grid blocks through the reservoir. While the pressure changes, the condition for fracture initiation, propagation, and width expansion will be checked for all grid blocks. On this basis, some grid blocks will join the fracture area. The associated characteristics (permeability, size and porosity) will therefore change (Zeini Jahormi and Wang, 2012). Figure 18 shows the flowchart for the coupled model.

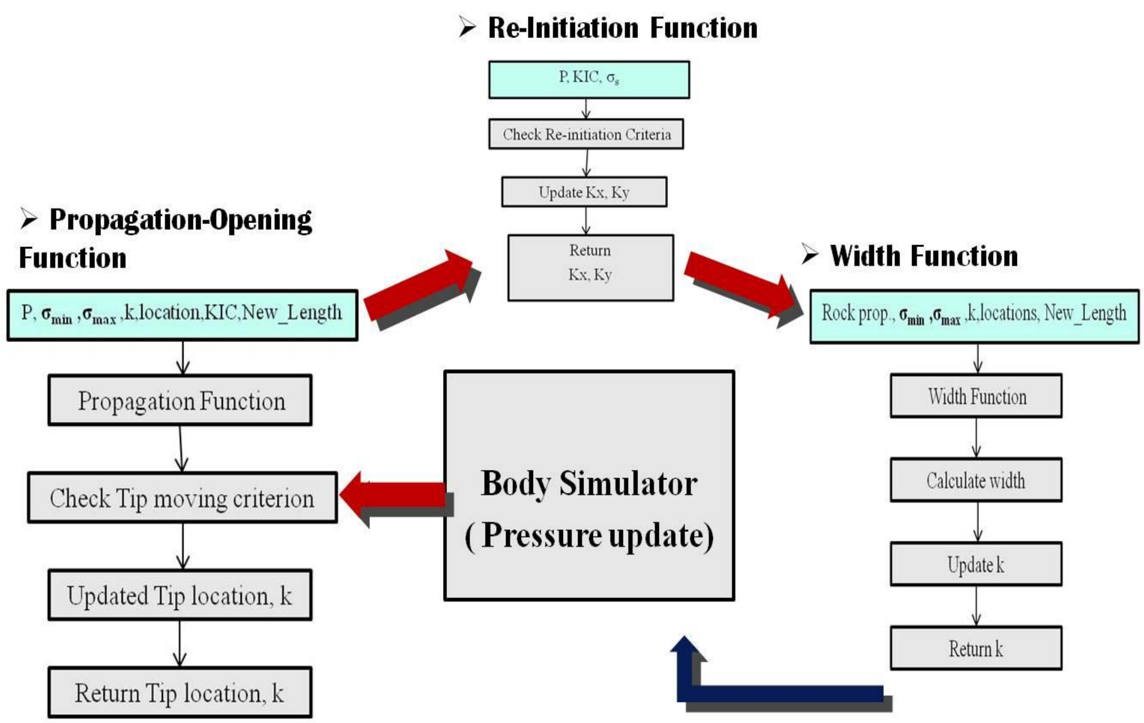

Figure 14. Flowchart for coupled fracture simulation

A numerical method has been used to solve both governing equations (reservoir fluid flow and fracture propagation equations). Using an iterative procedure, pressure changes inside the matrix and fracture, change of in-situ stresses and fracture propagation boundaries (fracture length and width) are calculated at each time step during and after the fracture treatment (Zeini Jahormi, Wang and Ertekin, 2012).

Time step (dt) selection is another key technique used for speedy simulation. Because of LGR and large permeability differences between the fracture block and matrix block, a large time step cannot be selected for the simulation to converge. Therefore, selecting a largest time step without sacrificing the accuracy of the simulation is the key for a time-efficient and accurate simulation. Iteration counts for the pressure update (Iter#), convergence criteria (ε), and incremental material balance check (IMBC) are considered as parameters for the selection. The material-balance check is the ratio of accumulation of mass to the net mass entering and leaving the boundaries of the reservoir. The material-balance check performed over a time step is known as the incremental material balance check, IMBC, and expressed as

$$\mathrm{IMBC} = \frac{\sum_{i=1}^{n_x}\sum_{j=1}^{n_y}\sum_{k=1}^{n_z}\frac{V_{b_{i,j,k}}}{\alpha_c}\left(\frac{\varphi^{n+1}}{B_l^{n+1}}-\frac{\varphi^{n}}{B_l^{n}}\right)_{i,j,k}}{\sum_{m=1}^{n+1}\Delta t^{m}{}_{i,j,k}\sum_{i=1}^{n_x}\sum_{j=1}^{n_y}\sum_{k=1}^{n_z} q_{lsc}^{m}{}_{i,j,k}}$$

(Eq. 29)

where,

$V_{b_{i,j,k}}$ = bulk volume for grid block i,j,k, ft^3

φ = porosity, fraction

B_l = Formation volume factor of the phase l, RB/STB

q_{lsc} = flowrate ate standard condition, bbl/day

Δt = timestep, day.

.

The figure below presents the flowchart for time-step selection.

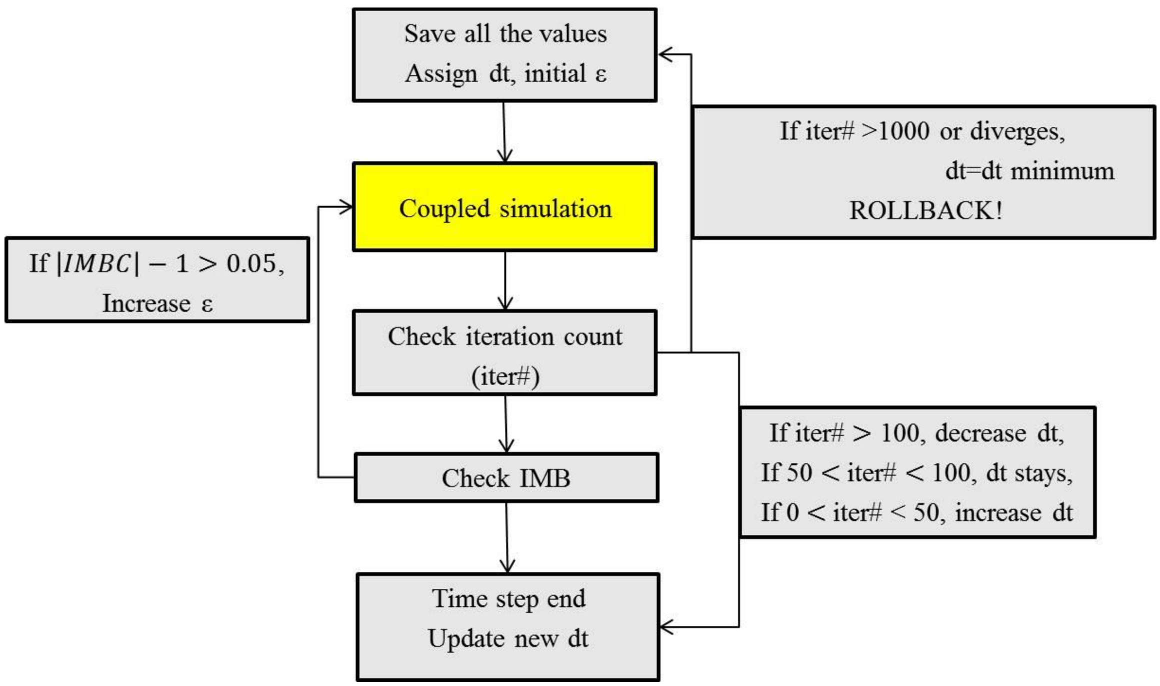

Figure 18. Time step selection flowchart

The time step is selected depending on the number of iterations from the simulator, and the accuracy of the simulation is maintained by increasing convergence criteria when the incremental material balance value moves away from 1. In addition, if the simulation fails to converge, instead of terminating the run and starting over, the model should repeat the time-step module with a very low dt such that the simulation can continue without restarting. Figure 19 shows the IMBC from constant ε and dynamic ε for 1000 time steps with a constant dt (10^{-8} day).

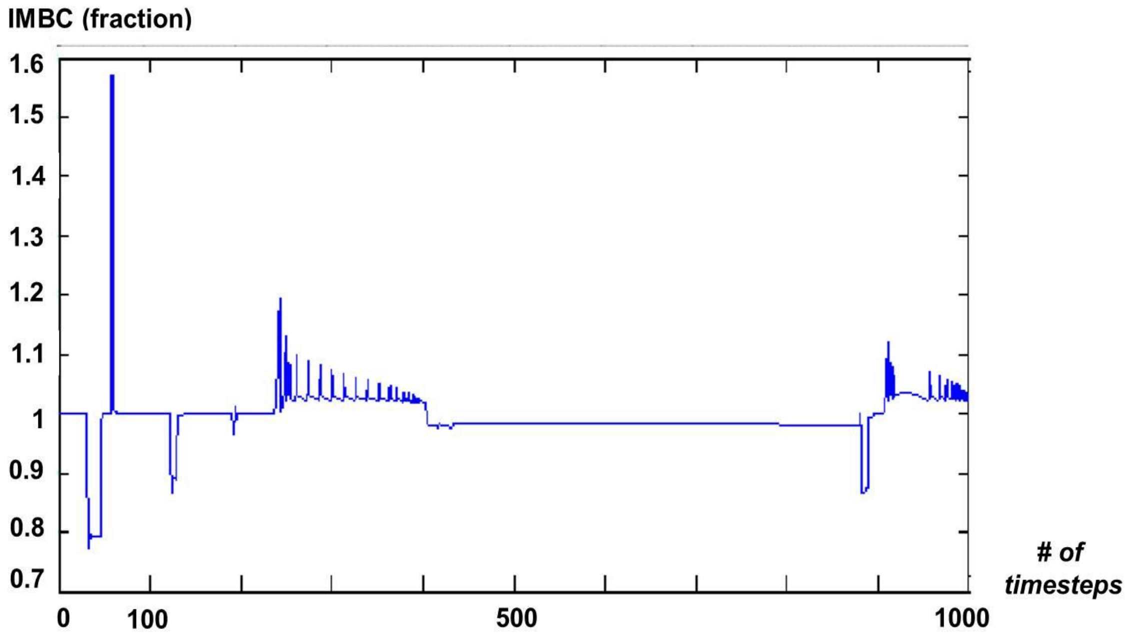

(a) Constant ε

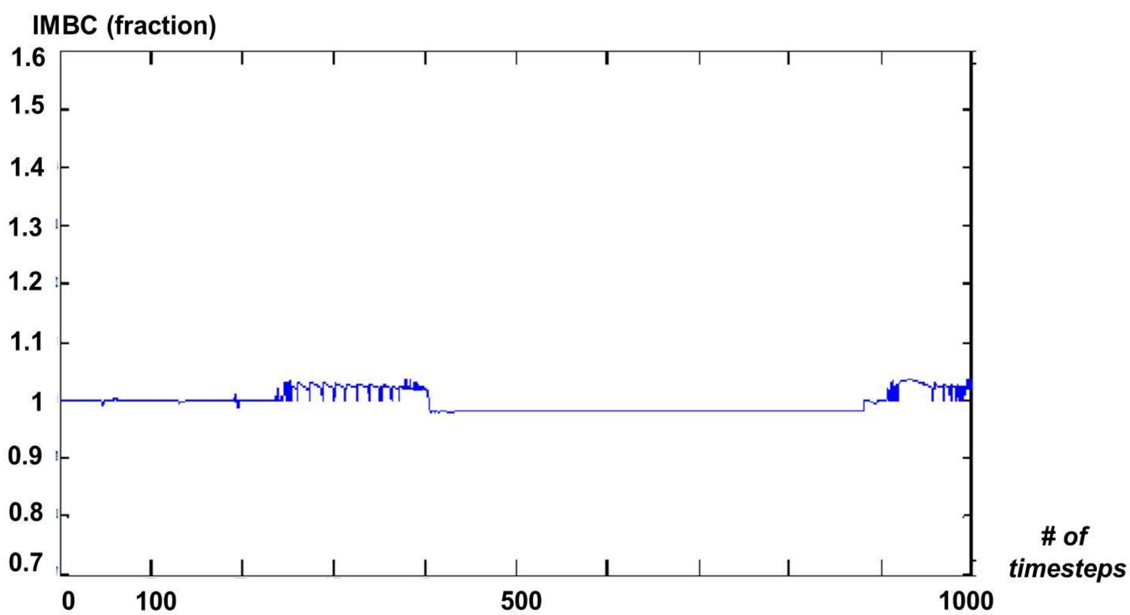

(b) Dynamic ε

Figure 19. IMBC results from 1000 time step (dt = 10^{-8} day)

It can clearly be seen from Figure 19 that the IMBC value from (b) is closer to 1 than (a). Figure 20 displays the IMBC results from our complete time step module, which includes a dynamic time-step section. From the same number of time steps of 1000, the total simulated time is 10^{-5} day in Figure 19 (b) but 5.55×10^{-4} day in Figure 20, which represents a 55-fold increase. The actual elapsed time for 1000 steps was similar in both cases.

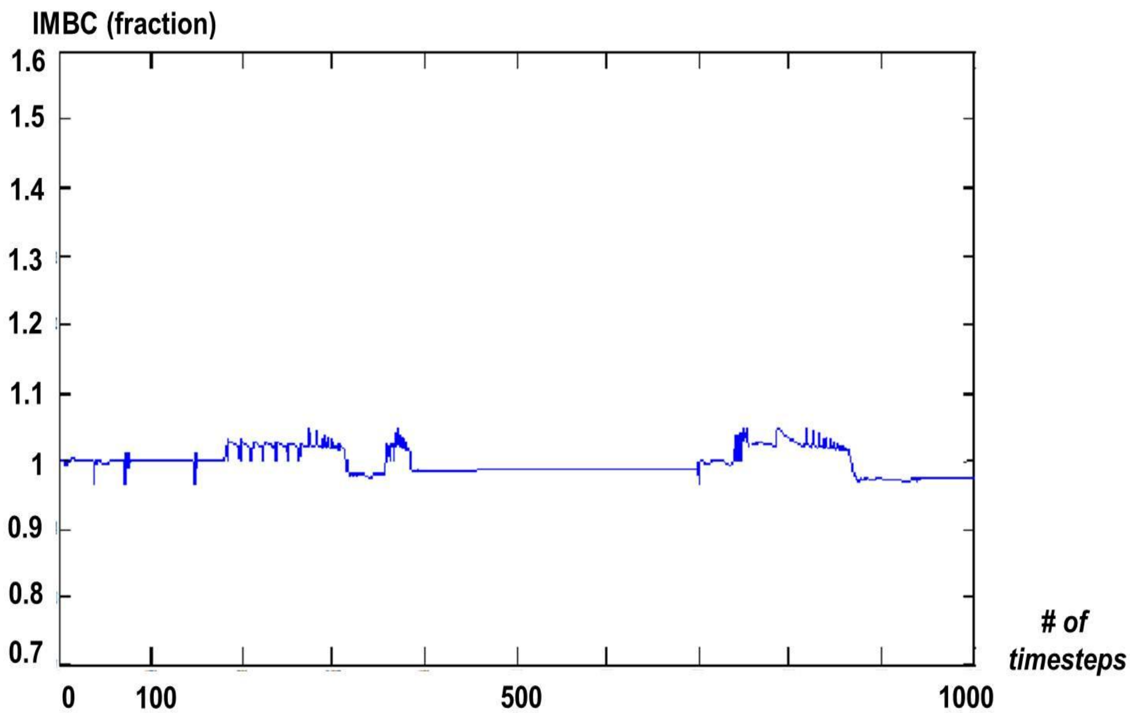

Figure 20. **IMBC result from the time step module (time steps = 1000, initial dt = 10^{-8}** day).

Chapter 4

MODEL VALIDATION

In the following sections, we validate our 2D 1-phase coupled model in three different steps. First is the validation for the hydraulic fracture propagation. In this part, single tip hydraulic fracturing propagation is simulated with local-grid-refinement(LGR) only applied to the width*(x)* direction and the results were compared with PKN and KGD results and Settari's simulation result as references (Settari, 2004). Second, we validated LGR implementation for both width*(x)* and propagation*(y)* directions using PKN and KGD analytical solutions and the results from Mohamad Zeini Jahromi's fracture propagation model. The third validation will look at the fracture opening behavior due to the effect of natural fractures.

4.1 Hydraulic Fracture Validation

Mohamad Zeini Jahromi (Zeini Jahormi, Wang and Ertekin, 2012) performed most of the validation in this section. Because his model and the model in this study share identical fracture propagation criteria when no natural fracture exists, we can take advantage of his validation work without a loss of generosity. He used two data sets to validate the hydraulic fracturing model:

- Case 1: using "Recent advances in hydraulic fracturing, chapter 4."
- Case 2: based on field data presented in the SPE 90874, Settari (2004) paper.

Table 1 shows the reservoir rock and fluid properties as input for the coupled model. Table 2 shows fracture treatment data, both based on the references mentioned. The predicted fracture length and width are presented with the corresponding reference data in Table 3.

Table 1. Reservoir rock and fluid properties as input for hydraulic fracture validation (Zeini Jahromi, 2012).

	Case 1	Case 2
Ky = permeability in y direction (flow direction)	10 md	50 md
Kx = permeability in x direction	4 md	50 md
Kyf = Kxf permeability of fracture	2000000 md	2000000 md
Φ = porosity	0.15	0.2
Pi = Initial reservoir pressure	2,750 psia	2,000 psia
σH1 = minimum in-situ normal rock stress, perpendicular to fracture face	2,750 psia	2,950 psia
σH2 = abounding in-situ normal rock stress	3,045 psia	2,950 psia
G = shear modulus of rock formation	1.45 x 10^6 psi	2.17 x 10^6 psi
ν = Poisson's ratio of rock formation	0.20	0.15
Stress-intensity-factor, KIC,	455 psi .$in^{0.5}$	100 psi .$in^{0.5}$
h_n or h_R= net reservoir interval height	100 ft	100 ft
h_g or h_f= gross fracture height	128 ft	128 ft
μ= fracturing fluid viscosity	1 cp	1 cp
Bw = Formation volume factor	1.0	1.0
ρ = Density	63.4 lbm/ft3	63.4 lbm/ft3
cw = Water compressibility	$5x10^{-7}$ psi^{-1}	4.93 $x10^{-6}$ psi^{-1}

Table 2. Results from the reference model (Zeini Jahromi, 2012)

	Case 1	Case 2
q_i = injection flow rate	10 bbl /min	13.1 bbl /min (18870 bbl /day)
t = injection time	400 minutes	14400 minutes (10 days)
Fracture Leangth PKN model	853 ft	
Fracture LeangthGdK model	636 ft	
Fracture Length simulation		1000 ft

Table 3. Results from the coupled model (Zeini Jahromi, 2012)

	Case 1	**Case 2**
Fracture Leangth	800 ft	900 ft
Fracture Width	0.04 ft	0.036 ft

As shown in Tables 2 and 3, the results from the coupled model are relatively similar to the reference data, which demonstrates the prove validity of our model.

4.2 LGR Validation

The above coupled model developed by Mohamad Zeini Jahromi was validated by applying LGR to the *x* direction(x-LGR) only so that, in this section, we will validate our model LGR applied for both width*(x)* and propagation*(y)* directions(x&y-LGR) by comparing the results from Mohamad Zeini Jahromi's model and the analytical results from PKN model. Table 4 presents the reservoir, rock, and fluid properties as input for LGR validation. Table 5 shows reservoir discretization inputs for LGR for the width*(x)* direction as well as inputs for use of both *x* and *y* directions. Figure 21 illustrates the reservoir map LGR applied for the *x* direction only. Figure 22 presents a map for LGR applied in both the *x* and *y* directions.

Table 4. Reservoir rock and fluid properties as input for LGR validation.

Rock and Fluid Properties	Input Data
Ky = permeability in y direction (flow direction)	0.00001 md
Kx = permeability in x direction	0.00001 md
Kynf, Kxnf = permeability of Natural Fracture	0.1 md
Φ = porosity	0.1
Φnf = porosity of NF	0.1
σ_{min} = minimum horizontal in-situ stress	2950 psia
σ_{max} = maximum horizontal in-situ stress	3000 psia
G = shear modulus of rock	2.17 x 10^{-6} psi
V = Poisson's ratio of rock	0.15
KIC = stress intensity factor	Matrix = 455, NF = 0
h = gross fracture height	100
μ = viscosity of fluid	0.8
Bw = FVF of frac. fluid	1.0
ρ = density of fluid	62.4 lb/cu.ft
Cw = compressibility of water	6.00 x 10^{-6} psi^{-1}
Wini = initial width of fracs	0.002 ft
Initial reservoir P =	2000 psi
Flow rate Q =	10 bpm

Table 5. Reservoir discretization results

Treatment time = 47 minutes	x-LGR	x&y-LGR
Nx = Number of rows of grid cells	168	168
Ny = Number of columns of grid cells	51	890
dx = grid length in x direction ft	0.002-12	0.002-12
dy = grid length in y direction ft	20	0.02-12

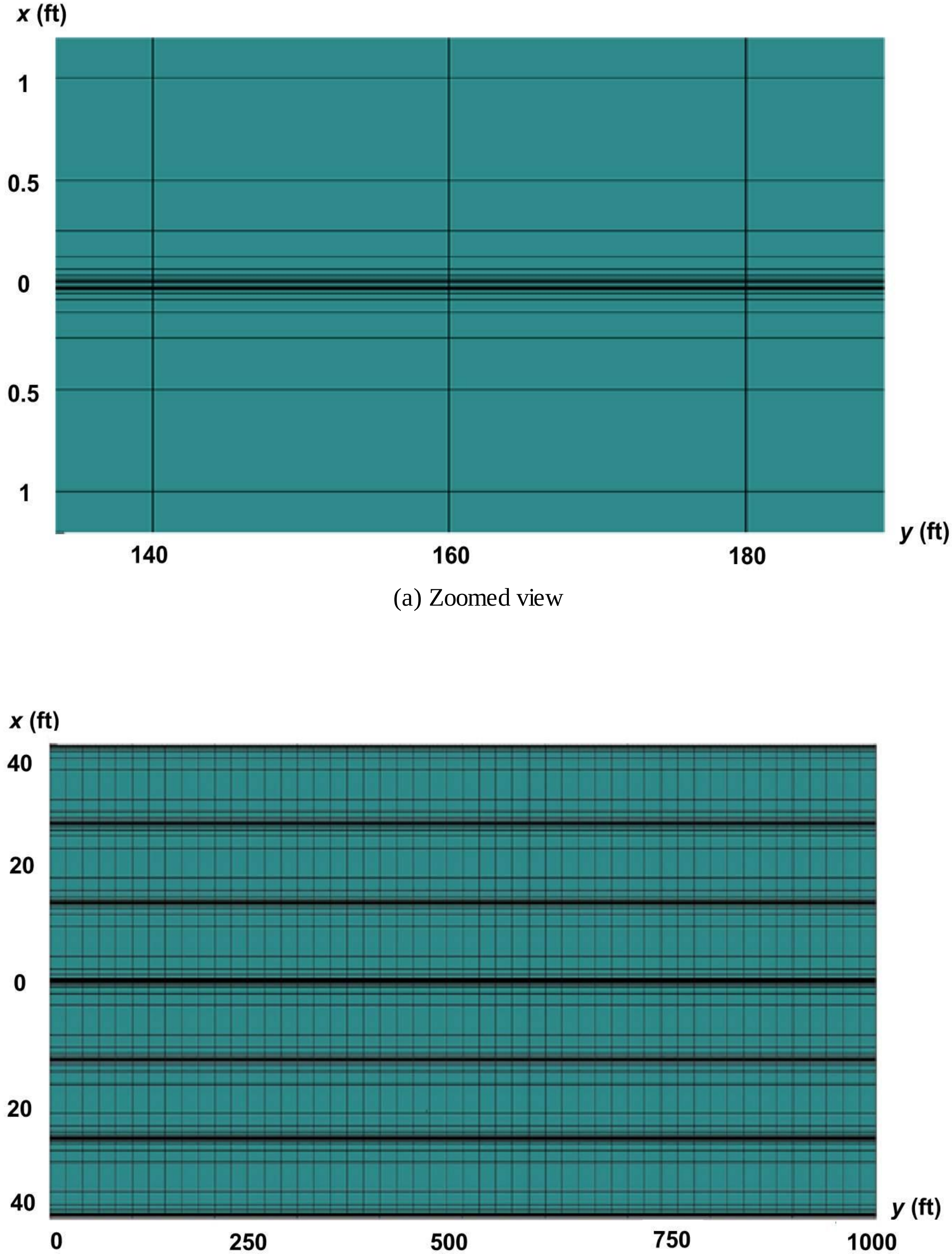

(a) Zoomed view

(b) Overall view

Figure 21. Discretization of the reservoir using LGR in the x direction only.

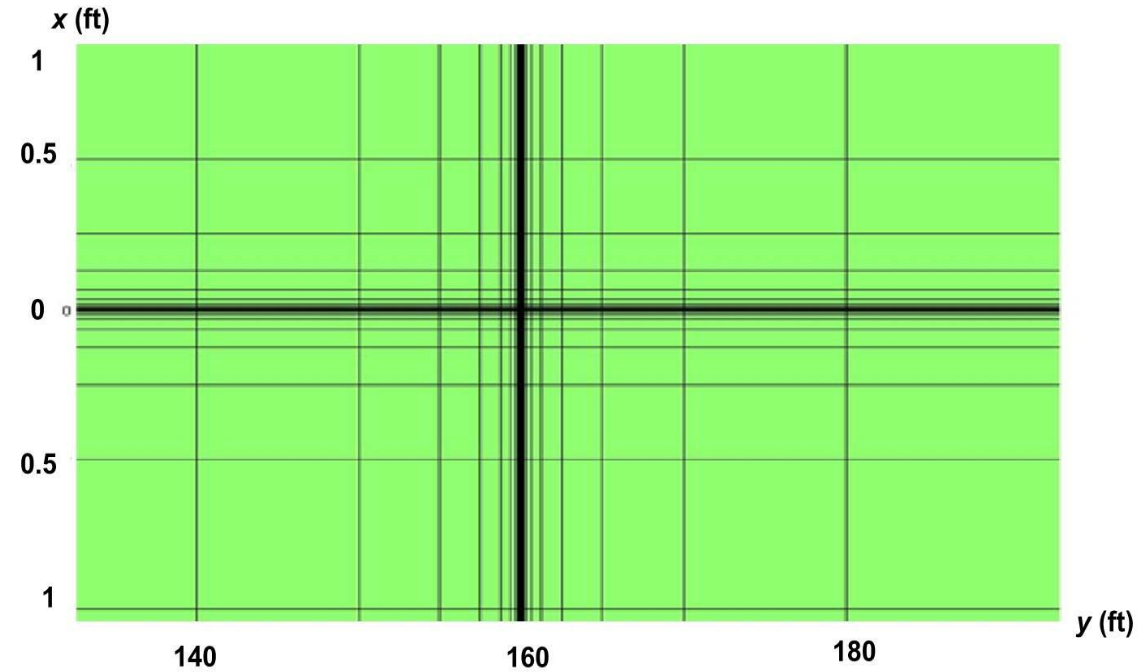

(a) Zoomed view

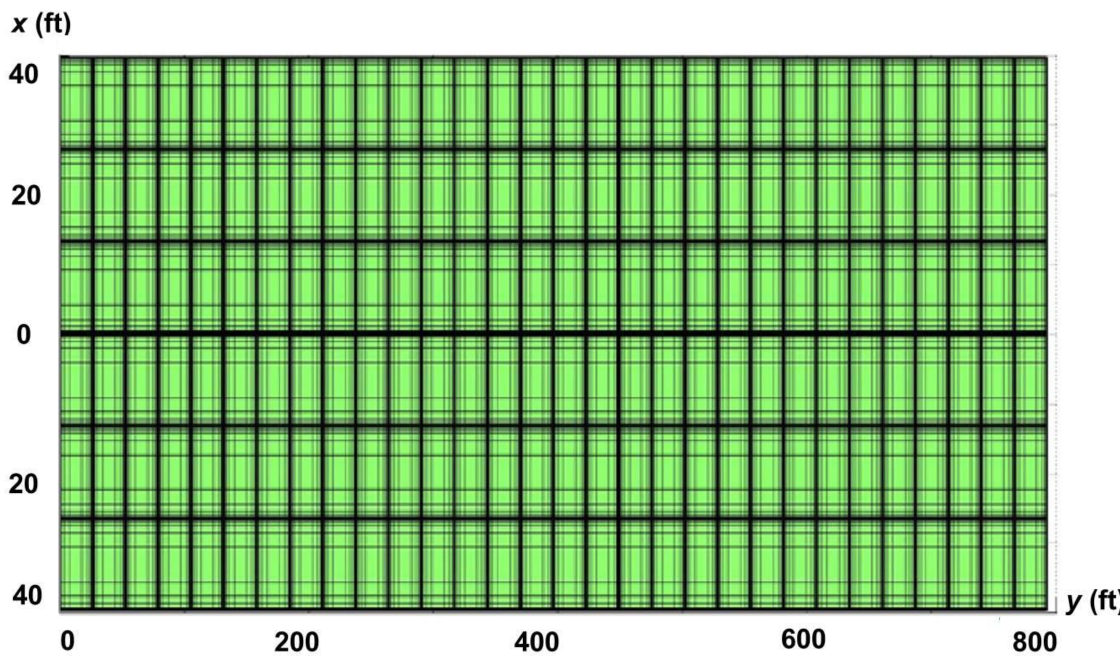

(b) Overall view

Figure 22. Discretization of the reservoir using LGR in *x* and *y* directions.

When using the above input data and grid system, if the results from both LGR cases are similar enough, then the validation can be considered as successful. Table 6 shows the resultant length and width from both cases as obtained through 47 minutes of simulation and the result from PKN analytical solution. The lengths of these results are not perfectly equal (280 ft, 297.702 ft and 322.505 ft) but are reasonable enough for the validation. The maximum width of the fracture is the same in both x-LGR and x&y-LGR simulations but PKN solution showed slightly narrower width.

Table 6. Length and width from the LGR validation results.

Treatment time = 47 minutes	x-LGR	x&y LGR	PKN
Length of the fracture (ft)	280	297.702	322.505
Width of the fracture (in)	0.288	0.288	0.192

Below Figure 23 confirms the validity of LGR. The plots of length (ft) versus time (min) are similar in both cases. In the case where LGR is only applied in the *x* direction, the curve is stair shaped because its grid block size is relatively greater in the *y* direction than in the other case. However, the graph of LGR in the *x* and *y* direction yields a smooth curve.

Figures 24 display similar plots of bottom-hole treatment pressure (BHTP). The plots are generated in a semi-log manner with respect to BHTP(psi) versus time(log(minute)). The graph of LGR in the *x* and *y* directions yields a smoother curve than the graph for the *x* direction alone. The points A in Figure 24 indicate the breakdown pressure and time of the fracture and all the peak points after the breakdown represents propagation pressure and time of the fracture.

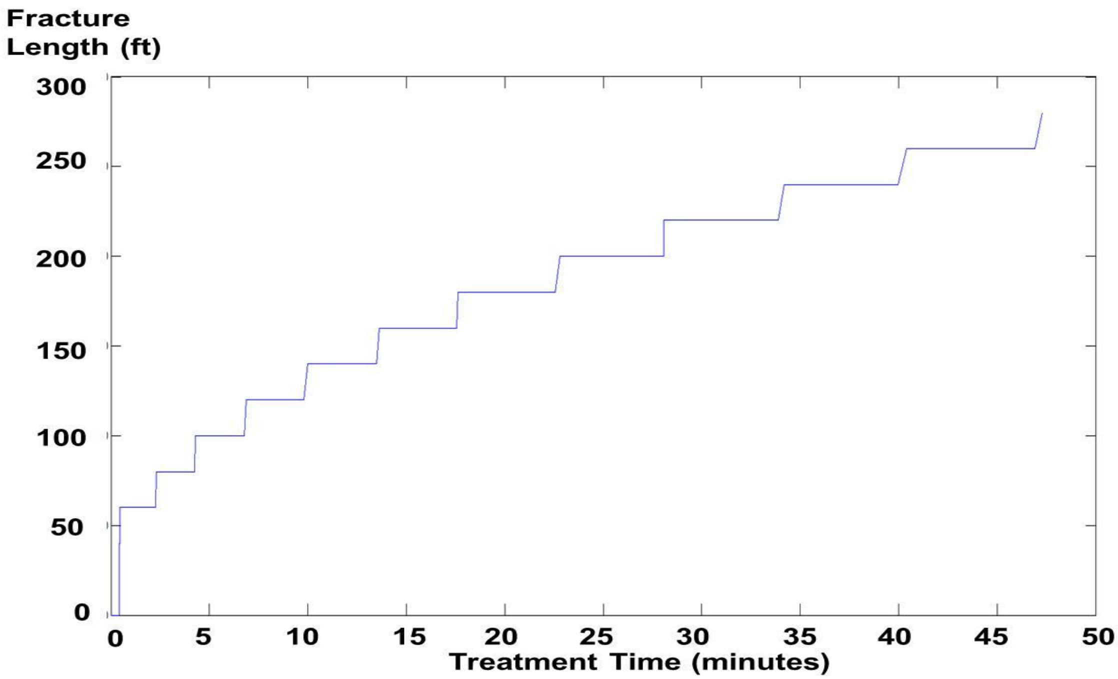

(a) LGR applied in the *x* direction only (x-LGR)

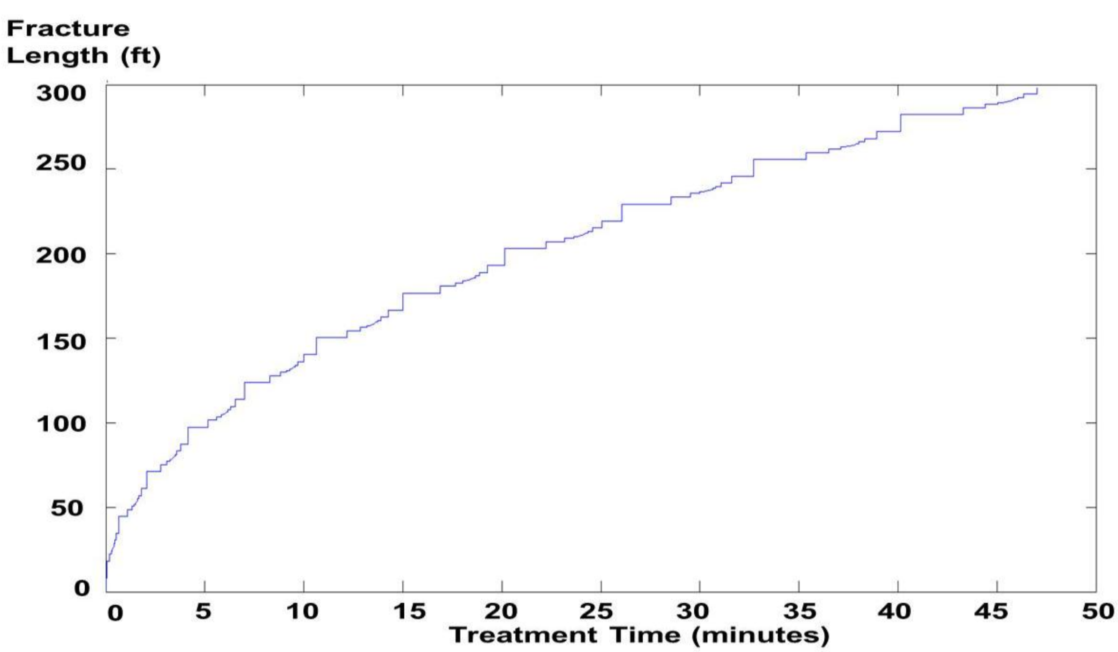

(b) LGR applied in the *x* and *y* directions (x&y-LGR).

Figure 23. Length(ft) versus time plots for both cases

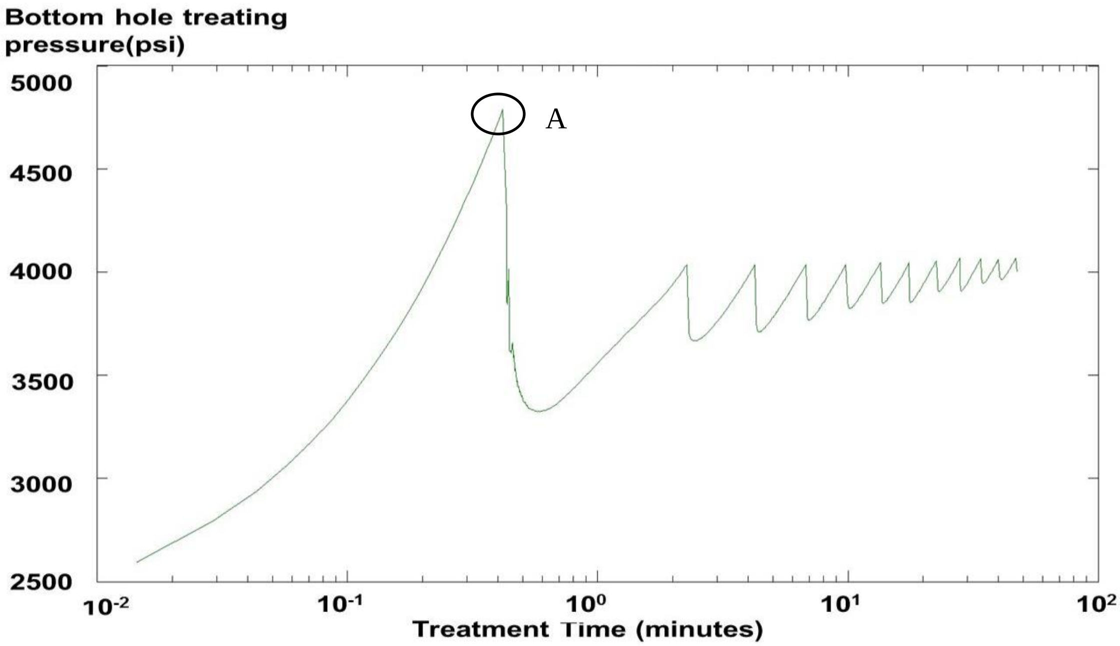

(a) LGR applied in the *x* direction only (x-LGR).

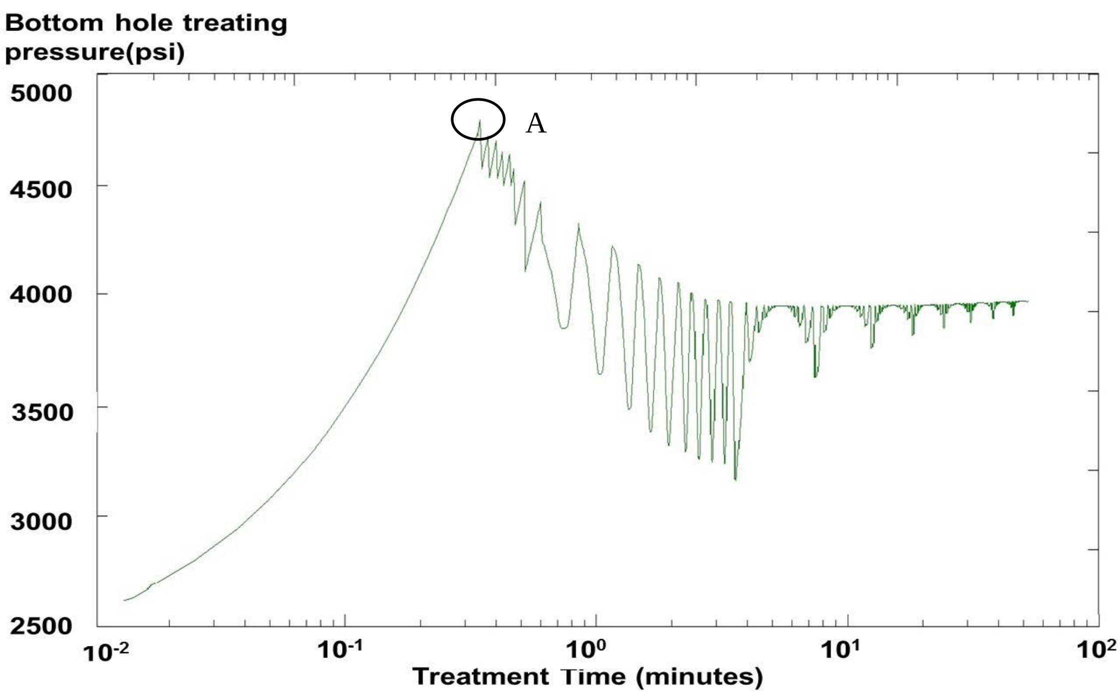

(b) LGR applied in the *x* and *y* directions (x&y-LGR).

Figure 24. BHTP(psi) versus Log(time(minute)) plots for both cases

Visual representations of the pressure and fracture geometry map (permeability map) are also displayed below for validation. Both axes in Figures 25 and 26 indicate grid blocks in the x and y directions; these are unrelated to the actual dimensions.

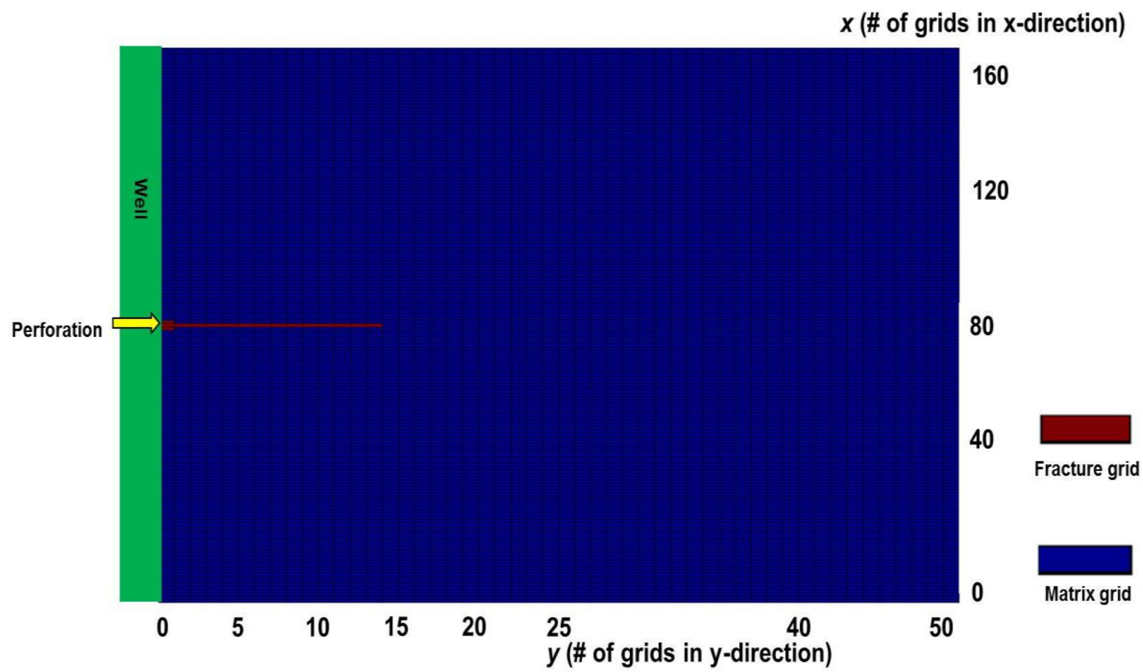

(a) Permeability map for x-LGR

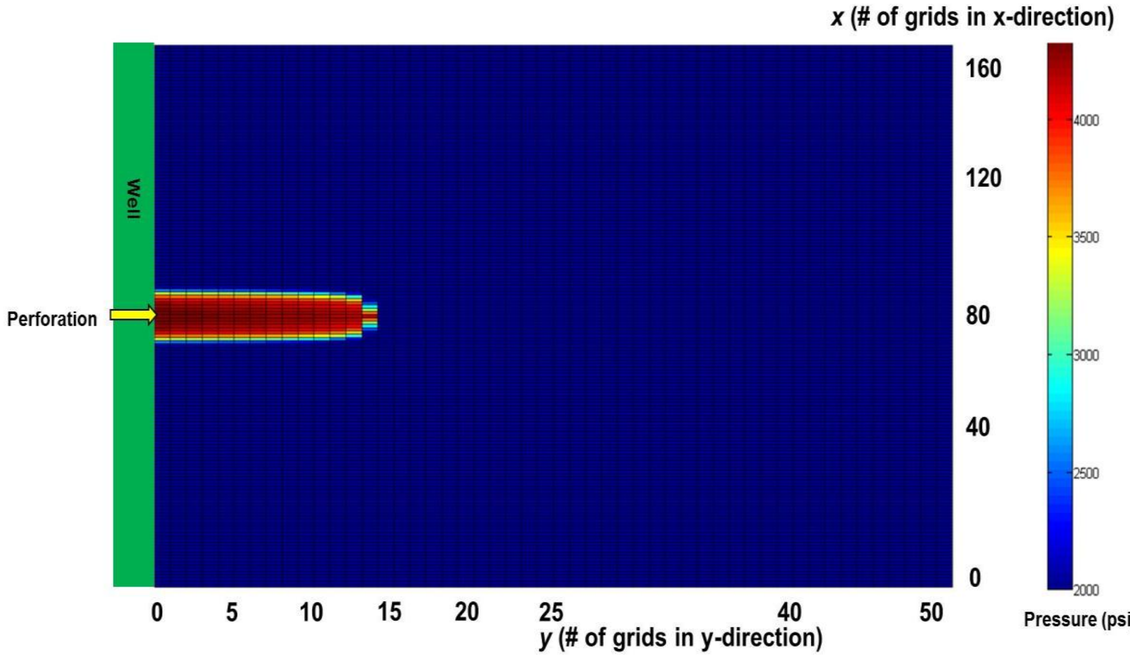

(b) Pressure map for x-LGR

Figure 25. Permeability and pressure map for LGR in the *x* direction.

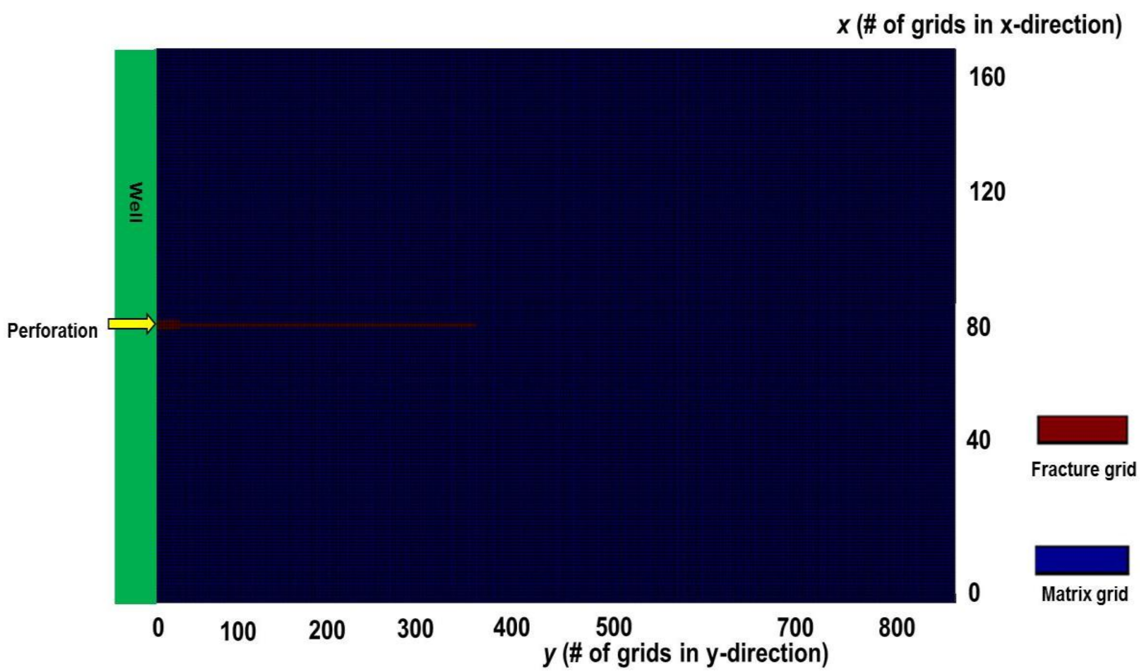

(a) Permeability map for x&y-LGR

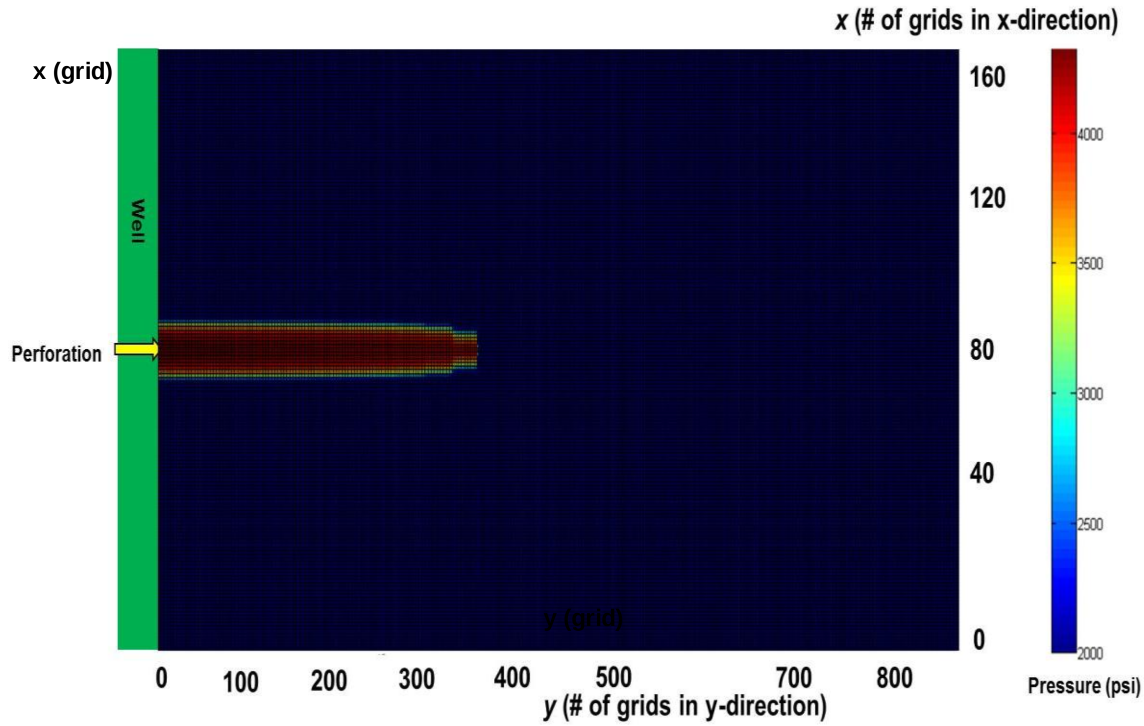

(b) Pressure map for x&y-LGR

Figure 26. Permeability and pressure maps for LGR in the for *x* and *y* directions.

From Figure 25 and 26, we can observe that both cases resulted fairly identical geometry after the simulation. Therefore, we can conclude the LGR module implemented in both *x* and *y* direction is accurate enough to prove the validity.

4.3 Validation of the Natural Fracture Effect

Because the crossing behavior at the intersection between the induced fracture and natural fracture is similar to that for the behavior of fractures without natural components, we will focus in this section on validating the initial behavior at the intersection. Using the analytical calculated results provided in Blanton's paper (Blanton, 1982), we can validate whether our model is indeed demonstrating identical fracture behavior at the intersection. Table 7 shows the input data and our results for comparison. Table 8 presents the rock and fluid input parameters for our coupled simulation.

Table 7. Input data for Blanton's analytical solution (Blanton, 1987).

	Blanton's	Couple Model
Distance to the natural facture	0.075ft	0.075ft
Length of NF		1ft
Max. Width of fracture		0.24in
KIC	67.2	67.2
Stress Anisotropy (σ_H-σ_h)	10	10
Open or Cross	Open	Open

Table 8. Rock and fluid properties for validation of the natural fracture effect.

Rock and Fluid Properties	Input Data
Ky = permeability in y direction (flow direction)	1 md
Kx = permeability in x direction	1 md
Kynf, Kxnf = permeability of Natural Fracture	0.1 md
Φ = porosity	0.1
Φnf = porosity of NF	0.25
σ_{min} = minimum horizontal in-situ stress	2010 psia
σ_{max} = maximum horizontal in-situ stress	2020 psia
G = shear modulus of rock	2.17 x 10^{-6} psi
V = Poisson's ratio of rock	0.15
KIC = stress intensity factor	Matrix = 67.5, NF = 0
h = gross fracture height	1
μ = viscosity of fluid	1
Bw = FVF of frac. Fluid	1.0
ρ = density of fluid	62.4 lb/cu.ft
Cw = compressibility of water	5.00 x 10^{-6} psi^{-1}
Wini = initial width of fracs	0.02 ft
Initial reservoir P =	2000 psi
Flow rate Q =	1 bpm

Because we seek to validate just the initial behavior of natural fractures, the reservoir size for this simulation was reduced to 5 ft by 10 ft (*x* x *y*). Figure 27 below shows the location of the natural fracture and reservoir boundaries.

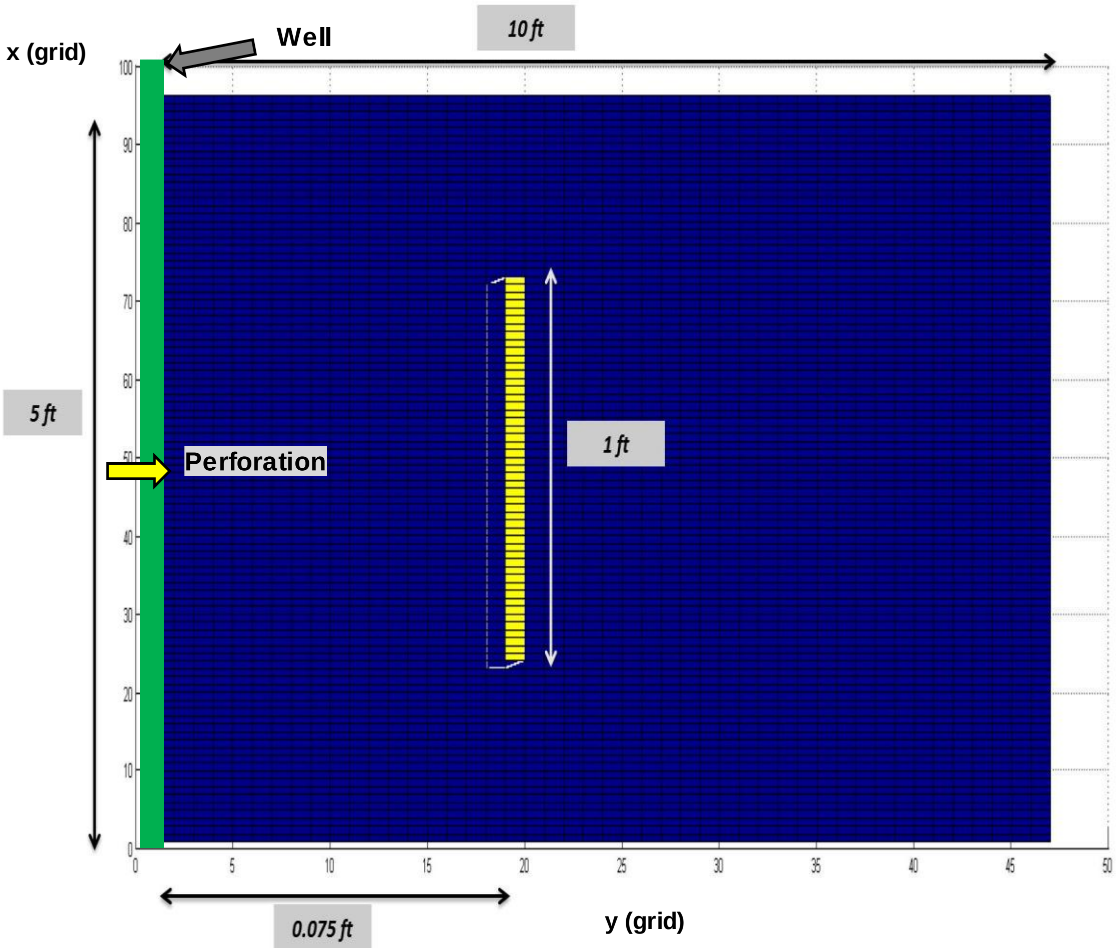

Figure 27. Location and length of the natural fracture and reservoir boundaries.

As shown in Figure 27, a natural fracture with the length of 1 ft is installed at the distance of 0.075 ft away from the perforation.

Figure 28 displays the permeability map for a treatment time of 3.2 seconds. This map clearly shows how the natural fracture dilation is related to the initial behavior of the fracture. At the intersection between natural and hydraulic fractures, we can see that the natural fracture opens in the *x* direction, then becomes a bi-wing fracture that propagates in the opposite direction.

Figure 29 indicates the pressure in the reservoir at the end of the fracture treatment. It illustrates the region of the fluid invasion.

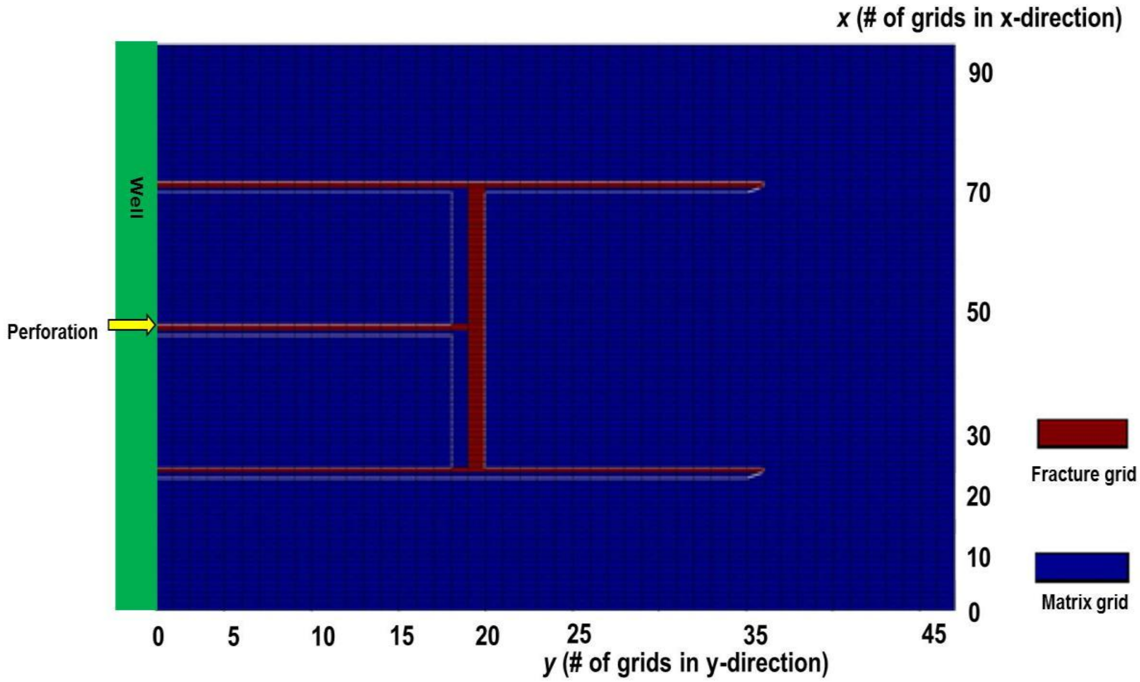

Figure 28. Permeability map for the opening validation run.

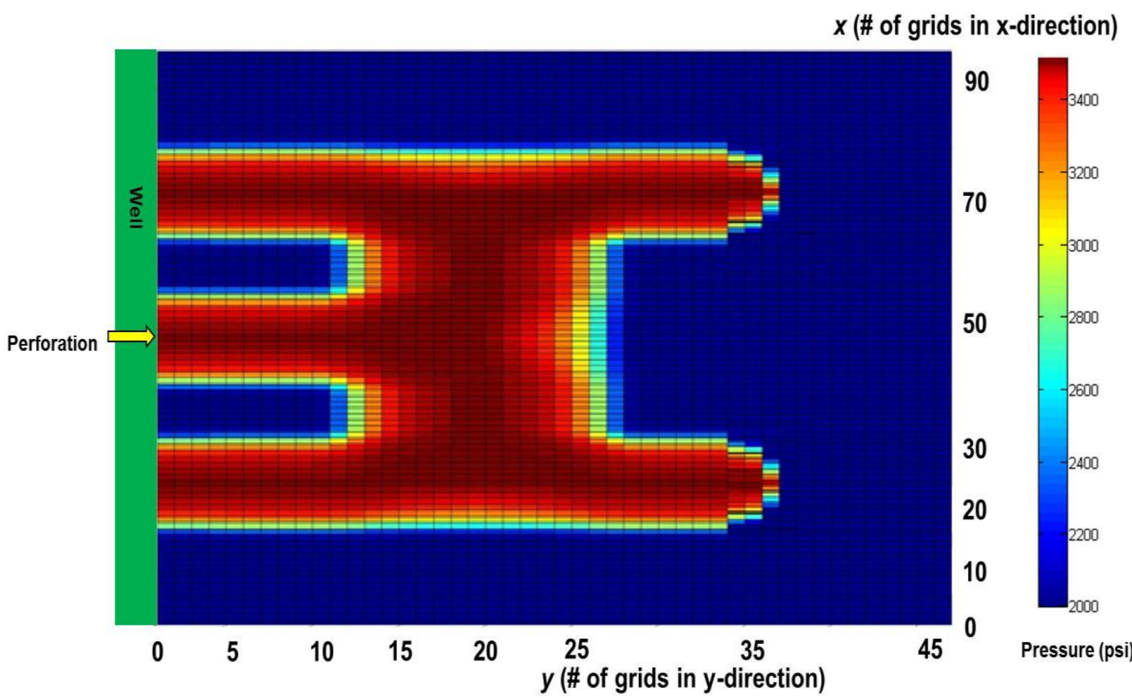

Figure 29. Pressure map for the opening validation run.

The results from this section (4.3) validated the opening behavior of the natural fracture at the intersection between the hydraulic fractures. It showed the same behavior as Blanton's experiment.

Chapter 5

RESULTS AND ANALYSES

We have developed and validated fully coupled model of complex hydraulic fracture propagation that can generate fracture network in a naturally fractured shale gas reservoir. Therefore, our coupled model will be used to investigate the impact of pertinent factors on ultimate fracture geometry, such as pre-existing natural fracture, rock toughness, natural fracture spacing, stress anisotropy, and perforation locations. Numerical experiments and analysis are documented as follows.

In section 5.1, we performed numerical experiment to quantify how rock toughness affects fracture geometry. This comparison study also allowed us to quantify the impact of rock toughness on final fracture geometry.

In section 5.2, we conducted a study that quantifies the impact of natural fracture spacing on the fracture network. The analysis moves from the near wellbores of the natural fracture to those that were farther away, and moves from perpendicular to parallel directions. This analysis allowed us to characterize the impact of natural fracture spacing on fracture growth.

In section 5.3, the effect of stress anisotropy is evaluated by performing several simulations using different anisotropies. This study is performed using a single perpendicular natural fracture system to see how stress anisotropy will affect the interaction between hydraulic and natural fractures.

In section 5.4, a complex natural fracture system is installed inside the reservoir. This simulation allowed us to investigate complex fracture network creation.

Finally, in section 5.5, we provided meaningful analysis on the effect of the natural fractures by introducing the concepts of *Fracture Network Index (FNI)* and *Width Anisotropy* (W_{ani}).

5.1 Effect of Rock Tougness

As shown in Equations 22 to 25, rock toughness governs propagation pressure. In this section, three cases are simulated:

- Case 1a : K_{IC} = 100 $psi \cdot in^{0.5}$,
- Case 1b : K_{IC} = 750 $psi \cdot in^{0.5}$,
- Case 1c : K_{IC} = 1500 $psi \cdot in^{0.5}$.

Figure 30 shows zoomed and overall views of the reservoir discretization map. Figure 31 indicates the location and length of the natural fracture in the formation. Table 9 shows reservoir rock and fluid properties for this section's simulation.

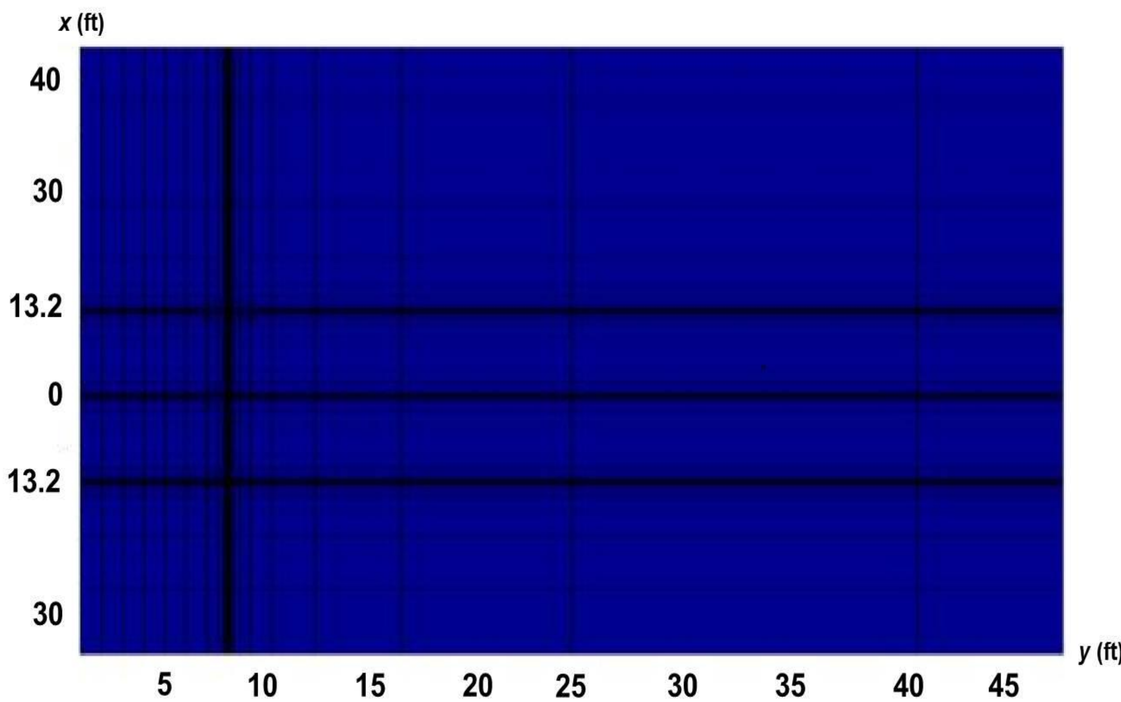

(a) Zoomed view.

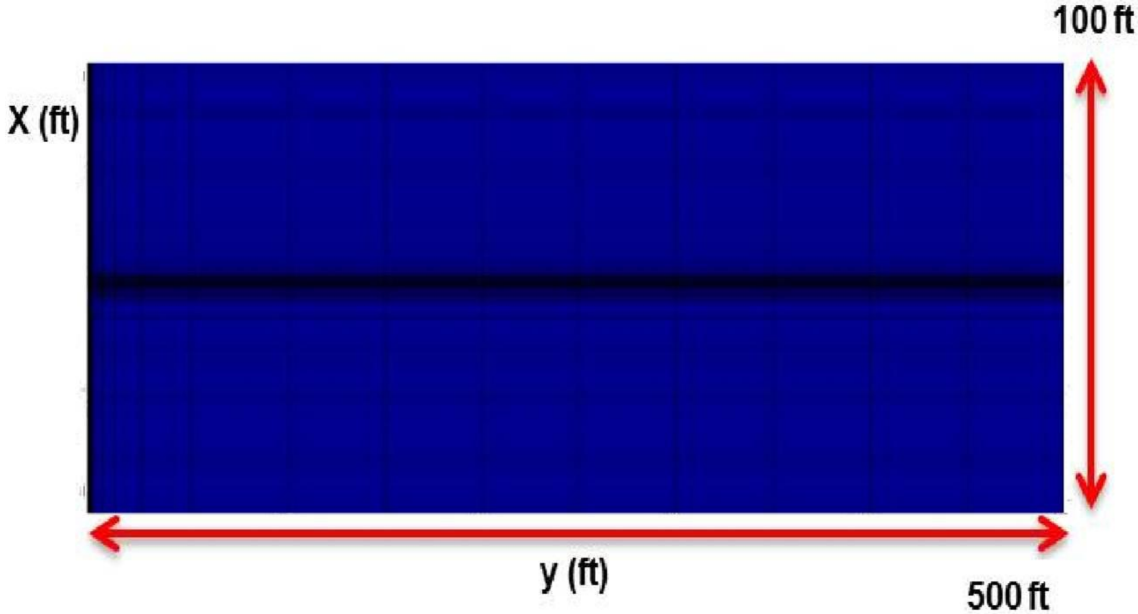

(b) Overall view.

Figure 30. Zoomed and overall view of the reservoir grid system.

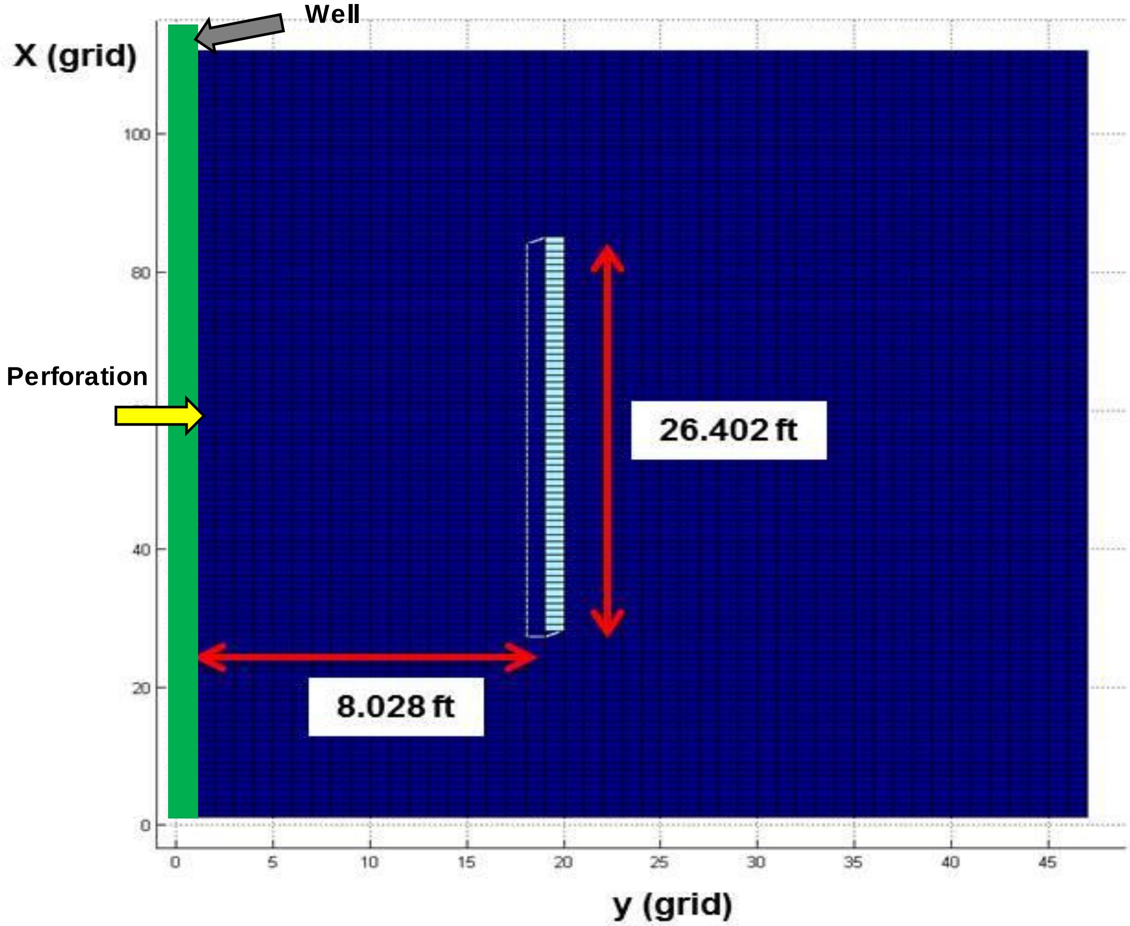

Figure 31. Location and length of the natural fracture in the system.

Table 9. Reservoir rock and fluid input data for this section.

Rock and Fluid Properties	Input Data
Ky = permeability in y direction (flow direction)	0.00001 md
Kx = permeability in x direction	0.00001 md
Kynf, Kxnf = permeability of Natural Fracture	0.1 md
Φ = porosity	0.1
Φnf = porosity of NF	0.1
σ_{min} = minimum horizontal in-situ stress	2950 psia
σ_{max} = maximum horizontal in-situ stress	3000 psia
G = shear modulus of rock	2.17 x 10^{-6} psi
V = Poisson's ratio of rock	0.15
h = gross fracture height	100
μ = viscosity of fluid	0.8
Bw = FVF of frac. fluid	1.0
ρ = density of fluid	62.4 lb/cu.ft
Cw = compressibility of water	6.00 x 10^{-6} psi^{-1}
Wini = initial width of fracs	Matrix=0.005ft, NF=0.002ft
Initial reservoir P =	2000 psi
Flow rate Q =	10 bpm

Figure 32 presents permeability maps of different cases: (a) K_{IC} = 100 psi $\cdot in^{0.5}$, (b) K_{IC} = 700 psi $\cdot in^{0.5}$, and (c) K_{IC} = 1500 psi $\cdot in^{0.5}$. The figures show that only Case 1c exhibited opening behavior. In Case 1b, the fracture initially crossed and subsequently began to open the natural fracture. Relatively high rock toughness generated high fluid pressure leading to the initiation of a natural fracture opening. The length of each case was 389.418 ft, 354.214 ft, and 337.105 ft, respectively; these results suggest that a low level of rock toughness results in longer fractures. However, the width results for each case showed a different relationship. The maximum width of was 0.156 in for Case 1a, 0.3 in for Case 1b, and 0.204 in for Case 1c. Generally, greater rock toughness is associated with wider fractures, but the opening behavior in Case 1c resulted in a fracture that was relatively smaller than in Case 1b. Table 10 displays the length and maximum width for each case simulation.

Table 10. Length and maximum width from the results of the simulation investigating rock toughness.

Treatment time = 60 minutes	Case1a	Case1b	Case1c
Max. Width (in)	0.156	0. 3	0.204
Length of NF (ft)	391.418	354.214	337.106

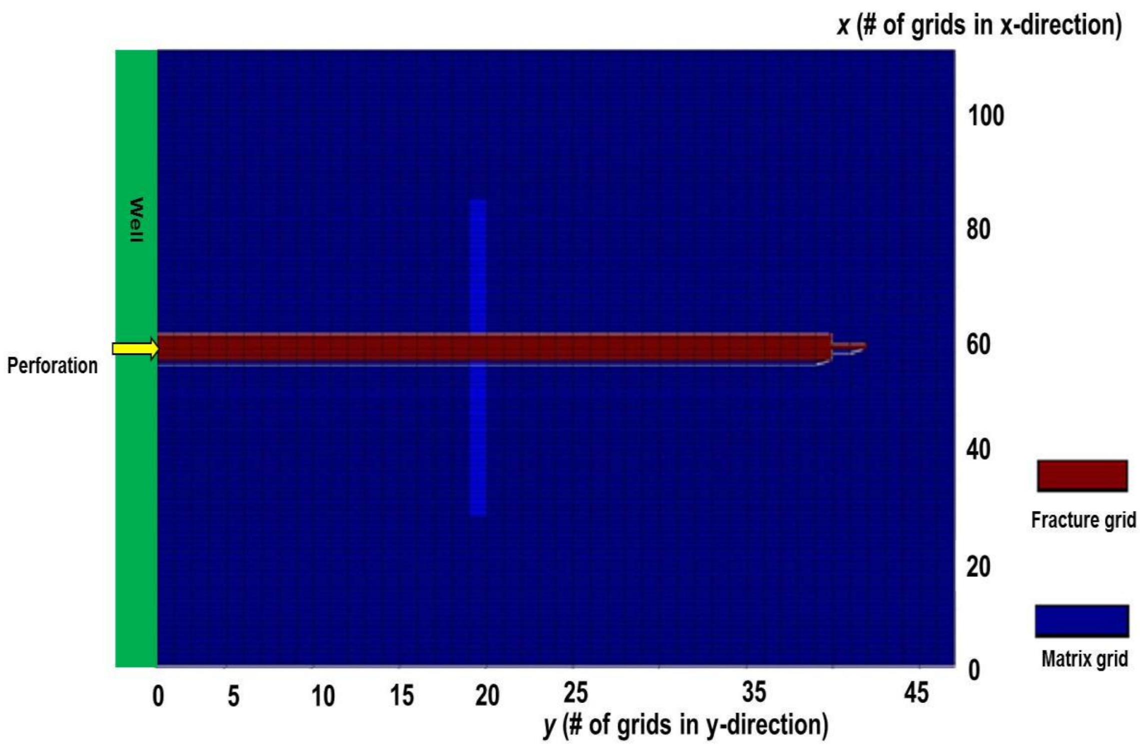

(a) Case 1a

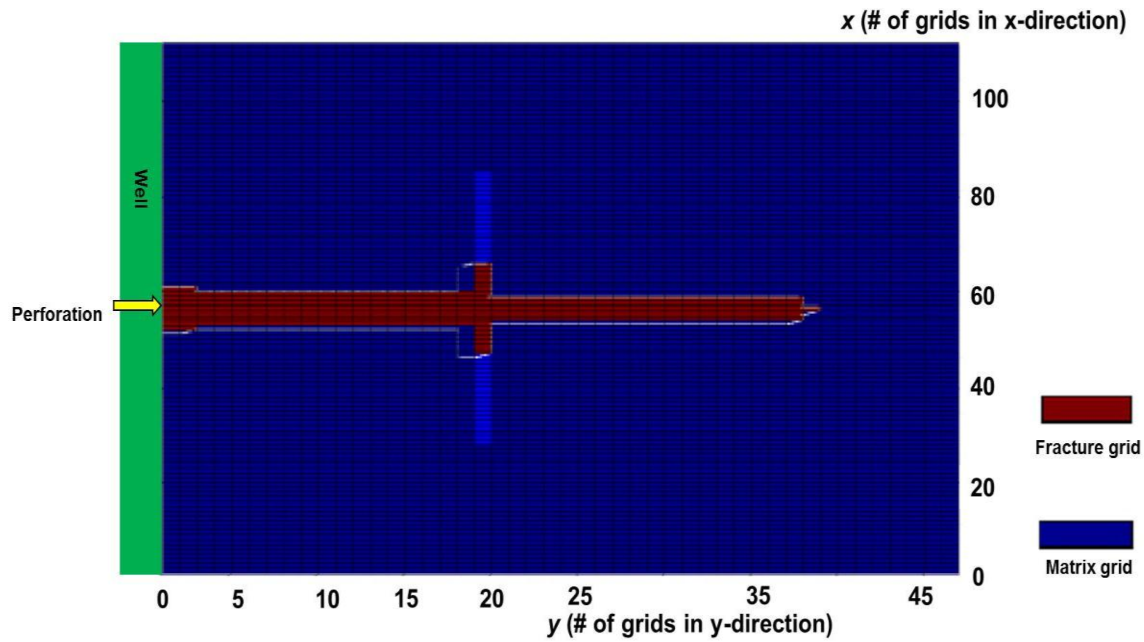

(b) Case 1b

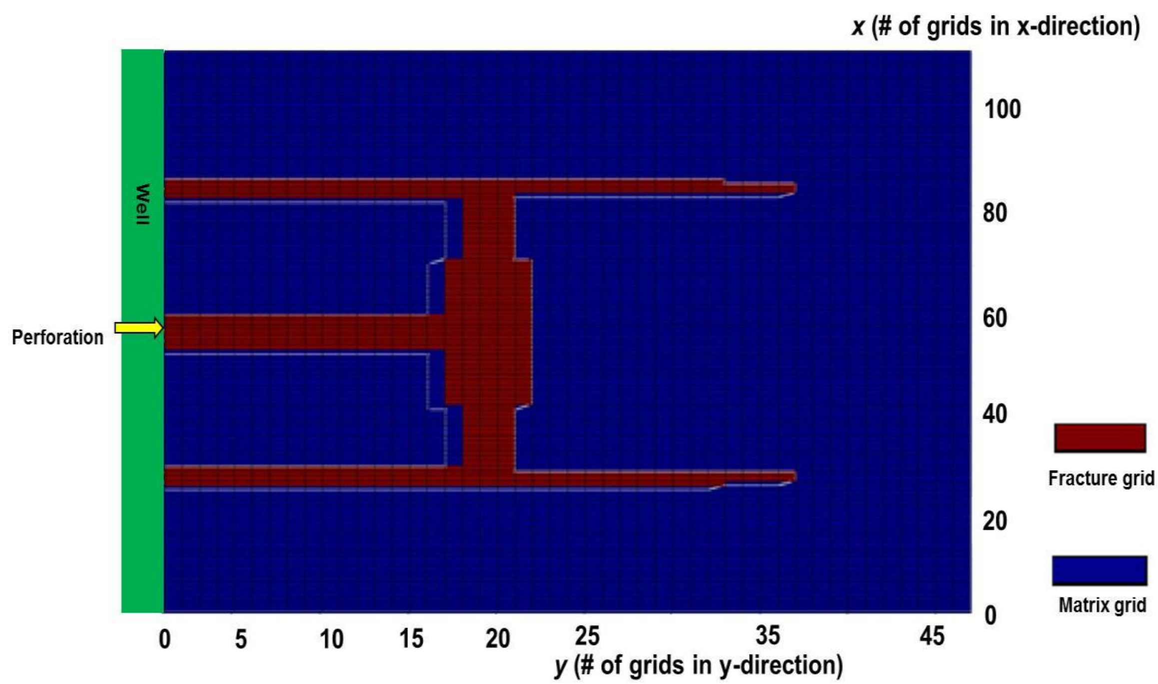

(c) Case 1c

Figure 32. Permeability Map for Rock toughness case study

Figure 33 presents pressure maps by case. We can see that more fluid leaked off to the natural fracture in Case 1b compared to Case 1a. This result may represent pressure-dependent leakoff, because fluid pressure was much higher in Case 1b than in Case 1a.

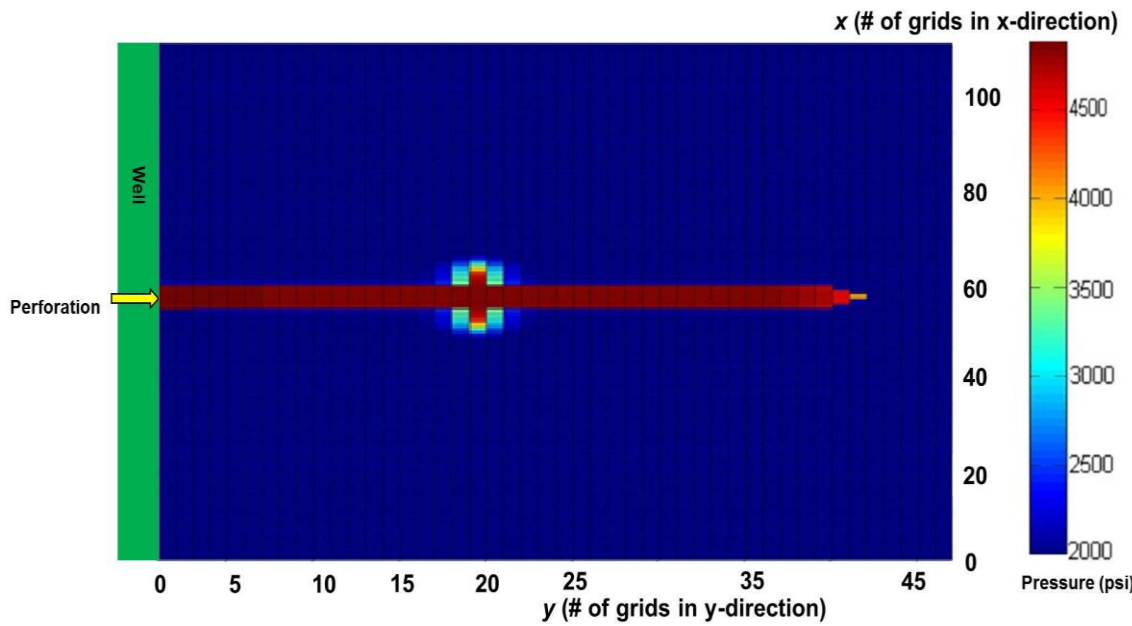

(a) Case 1a

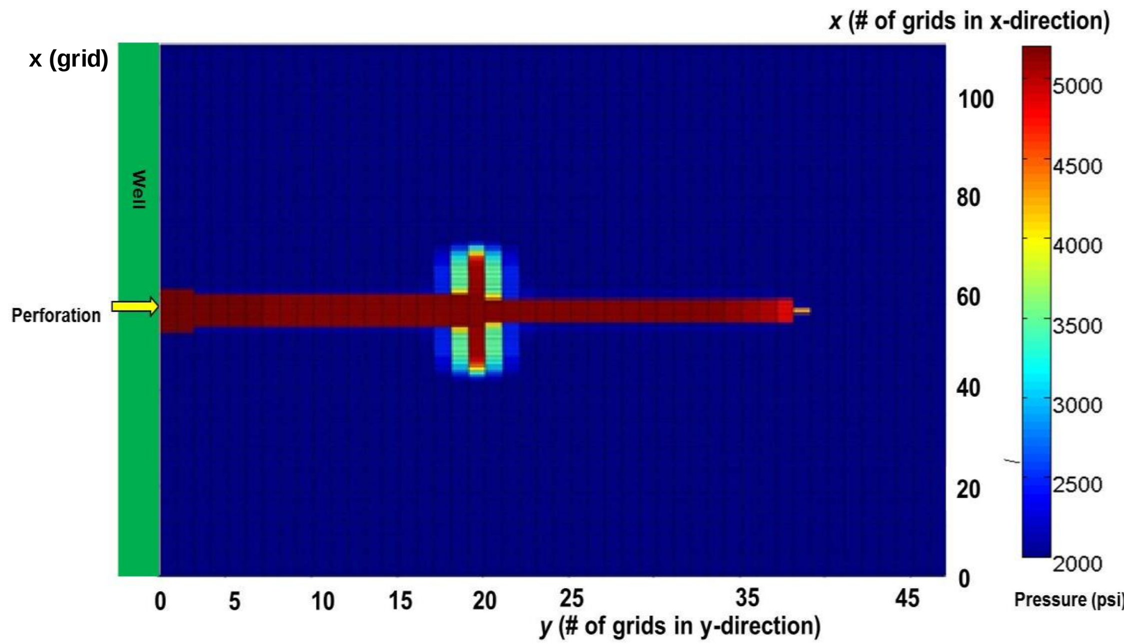

(b) Case 1b

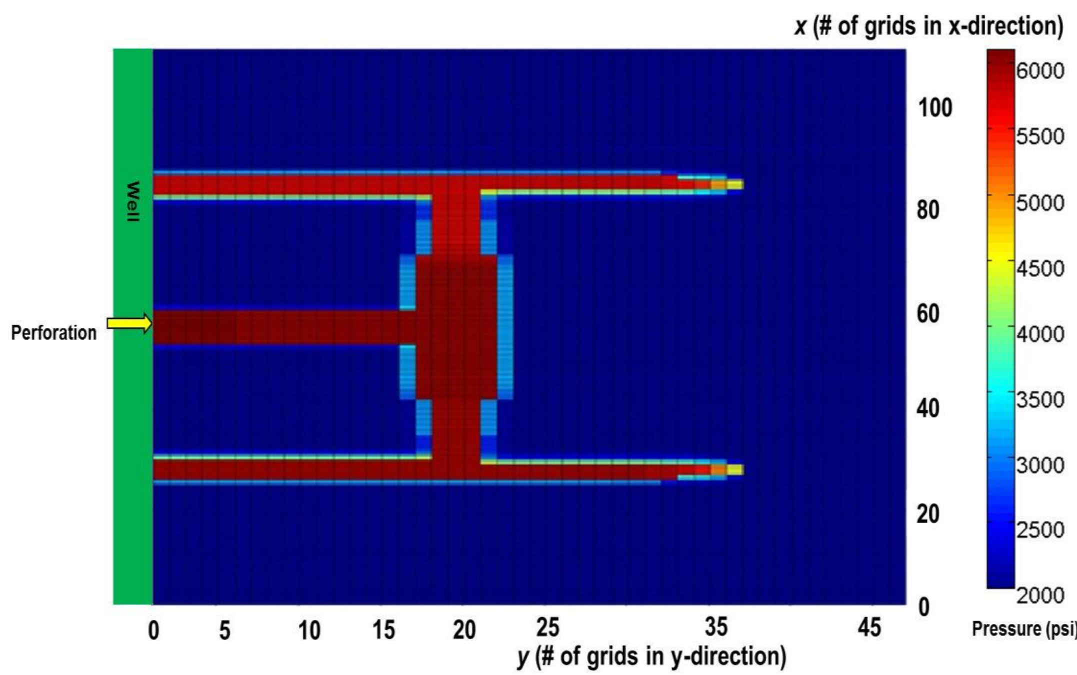

(c) Case 1c

Figure 33. Pressure maps for rock toughness.

BHTP plots in Figure 34 clearly show that Case 2 has higher fluid pressure.

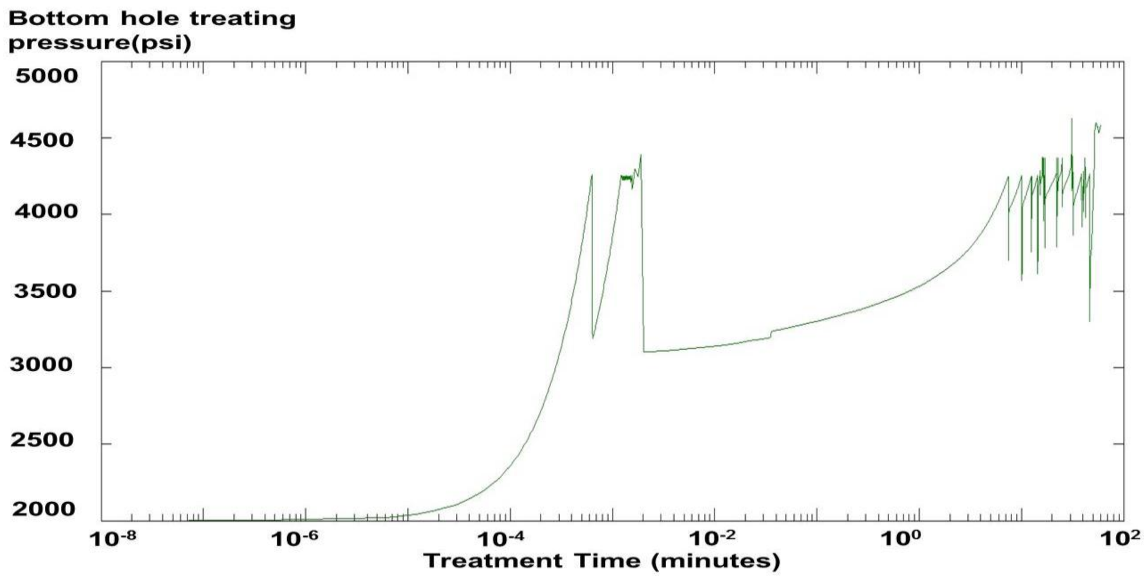

(a) Case 1a

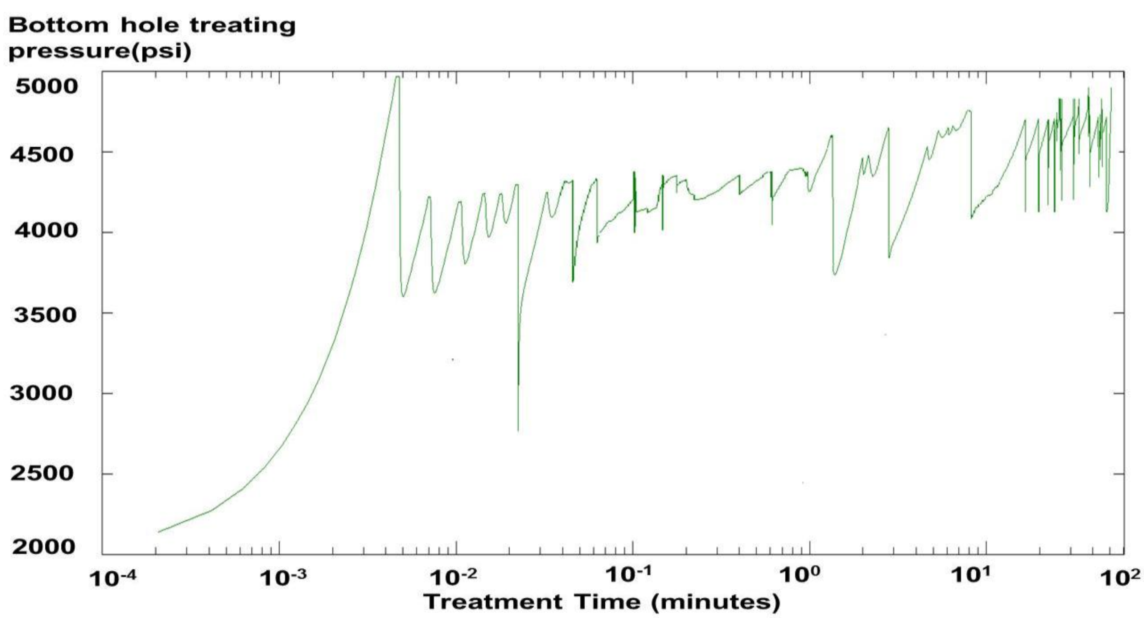

(b) Case 1b

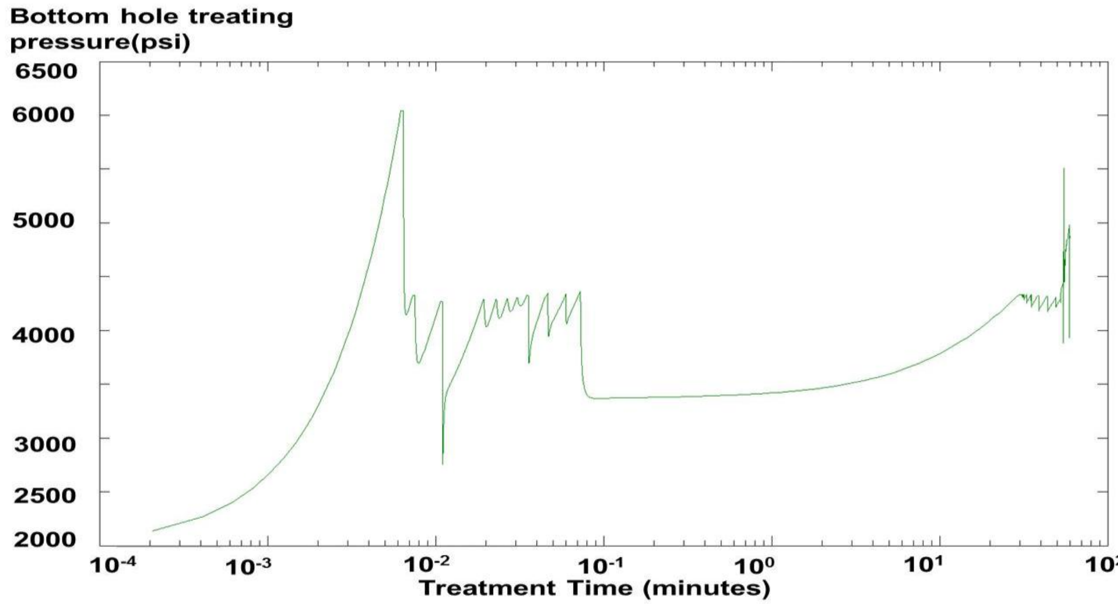

(c) Case 1c

Figure 34 BHTP vs. log(time) with respect to rock toughness.

In Figure 34(c), we can observe a dramatic pressure drop, which indicates the opening behavior. Governing propagation pressure is reduced at the intersection of the hydraulic fracture and natural fracture. The fracture opens the natural fracture at high velocity, as reflected in the BHTP plot for Case 1c.

From the case study in this section 5.1, we observed three different interaction behaviors: an immediate opening (Case 1c), an opening after crossing (Case 1b), and a crossing with the natural fracture remained close (Case 1a). This phenomenon can be explained by Equation 25 since large rock toughness affects to the change of minimum propagation pressure at the intersection between the natural fracture and the hydraulic fracture.

5.2 Effect of Natural Fracture Spacing

In this section, we investigated the effect of natural fracture spacing in two directions. For Step 1, by locating a perpendicular natural fracture (parallel to the σ_h direction) in two locations 0.06ft and 8.028 ft away, respectively, from the initiation point, we observed fracture propagation to identify the effect on fracture geometry. Figure 35 below shows the initial geographical setting for the simulation. Table 11 presents the input data.

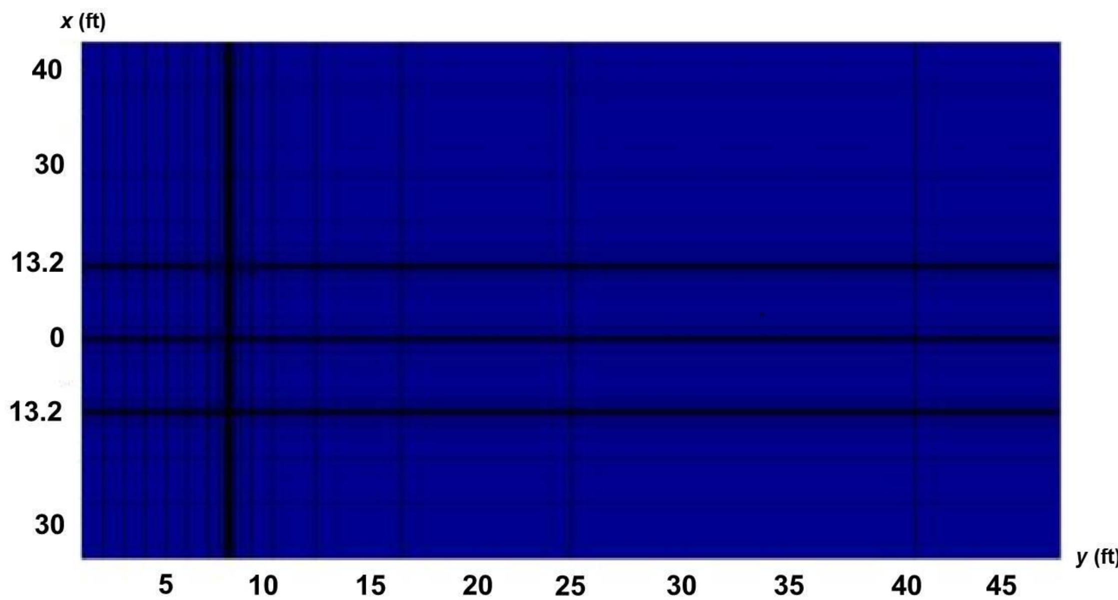

(a) Zoomed view.

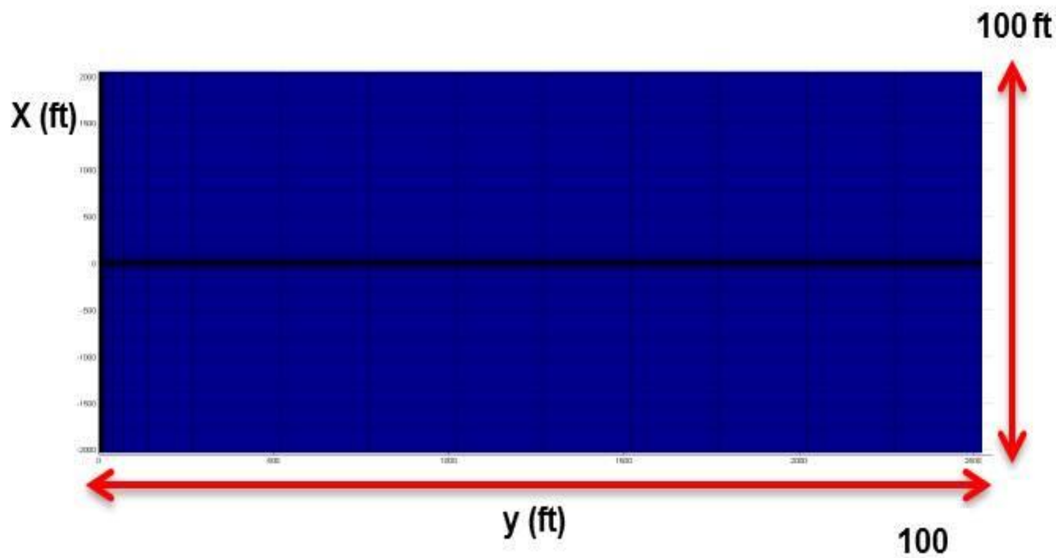

(b) Overall view.

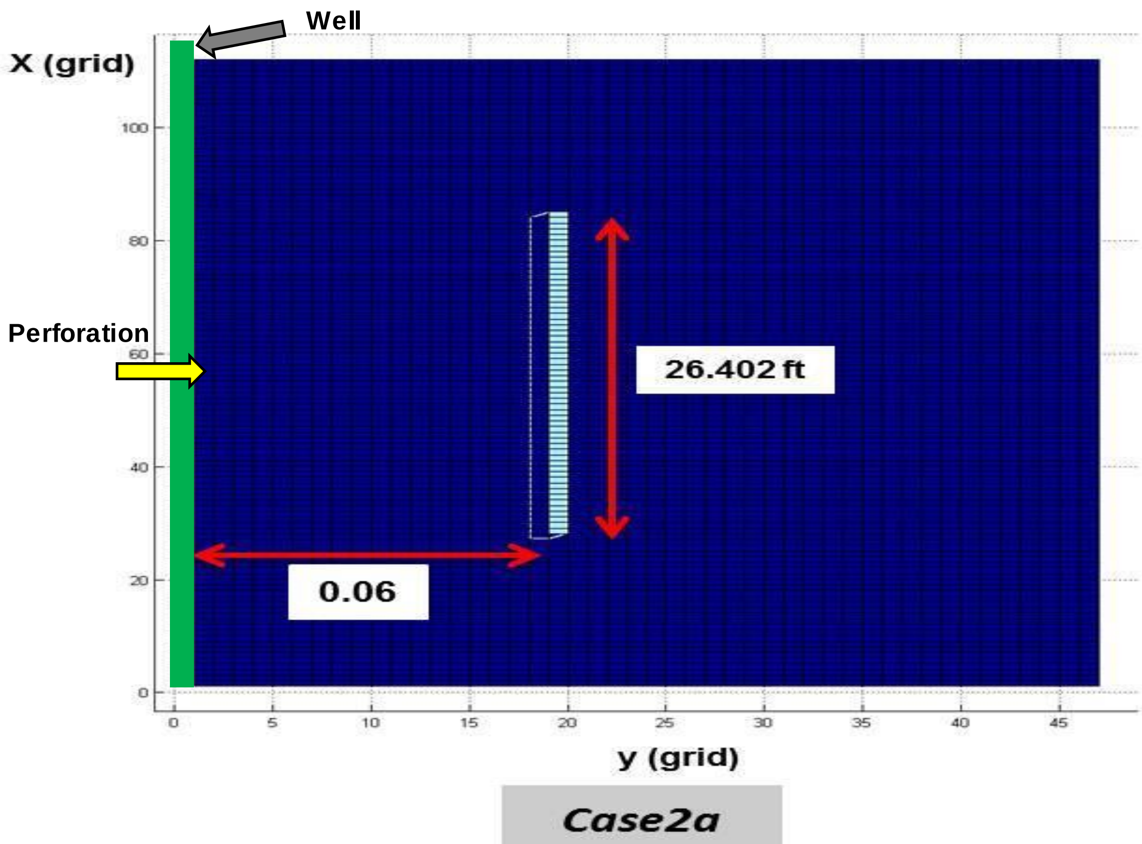

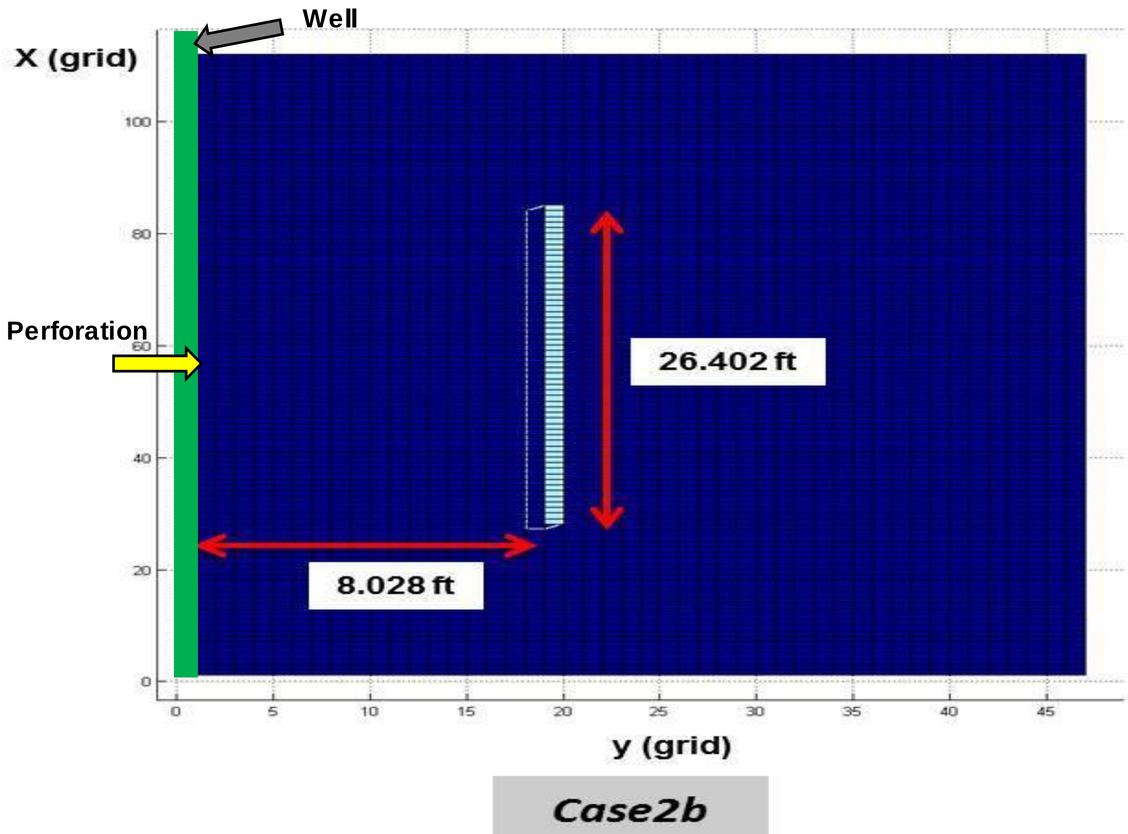

(c) NF location for Case 2a (0.06 ft) and Case 2b (8.028 ft).

Figure 35. (a) Zoomed and (b) overall views, and (c) NF locations of the reservoir grid system for NF spacing observations (Step 1).

As shown in Figure 35 and Table 11, Case 2a and 2b have the same reservoir property, rock property, fluid property, and fracture treatment, except the distance of existing natural fracture to the perforation.

Table 11. Reservoir rock and fluid input data for NF spacing observation (Step 1).

Rock and Fluid Properties	**Input Data**
Ky = permeability in y direction (flow direction)	0.00001 md
Kx = permeability in x direction	0.00001 md
Kynf, Kxnf = permeability of Natural Fracture	0.1 md
Φ = porosity	0.1
Φnf = porosity of NF	0.1
σ_{min} = minimum horizontal in-situ stress	2950 psia
σ_{max} = maximum horizontal in-situ stress	3000 psia
G = shear modulus of rock	2.17 x 10^{-6} psi
V = Poisson's ratio of rock	0.15
KIC = rock toughness	455
h = gross fracture height	100
μ = viscosity of fluid	0.8
Bw = FVF of frac. fluid	1.0
ρ = density of fluid	62.4 lb/cu.ft
Cw = compressibility of water	5.00 x 10^{-6} psi^{-1}
Wini = initial width of fracs	Matrix=0.005ft, NF=0.005ft
Initial reservoir P =	2000 psi
Flow rate Q =	10 bpm

Controlling for every condition except the location of natural fracture, we performed two simulations of 10-minute fracture treatments. In Case 2a, hydraulic fracture immediately opened the natural fracture at the intersection. In Case 2b, the fracture propagated across the pre-existing fracture. This difference can be explained using Equation 25. As length grows longer, propagation pressure decreases so that minimum propagation pressure as predicted using Equation 25 differs for Case 2a and Case 2b. Table 12 shows the relationship between hydraulic fracture and natural fracture with minimum propagation pressure at the intersection.

Table 12 Minimum propagation pressure at the HF-NF intersection (NF spacing case study, Step 1).

	Case2a	Case2b
$min \begin{Bmatrix} \sigma_{h@i,j} + \frac{K_{ICm@i,j}}{\sqrt{\pi L_{f@i,j}}} \\ \sigma_{H@i,j} + \frac{K_{ICm@i,j}}{\sqrt{\pi L_{f@i,j}}} \\ \sigma_{h@i,j} + \frac{K_{ICnf@i,j}}{\sqrt{\pi L_{f@i,j}}} \\ \sigma_{H@i,j} + \frac{K_{ICnf@i,j}}{\sqrt{\pi L_{f@i,j}}} \end{Bmatrix}$	$\sigma_{H@i,j} + \frac{K_{ICnf@i,j}}{\sqrt{\pi L_{f@i,j}}}$	$\sigma_{h@i,j} + \frac{K_{ICm@i,j}}{\sqrt{\pi L_{f@i,j}}}$

Table 13 lists general geomechanical results from the simulation. Figures 35 and 36 present permeability maps.

Table 13. Length and width results of NF spacing (Step 1).

Treatment time = 10 minutes	Case2a	Case2b
Max. Width (in)	0.132	0.132
Length of NF (ft)	68.482	76.306

We can see both cases resulted identical maximum widths but the length in Case 2a extended 68.482 ft which is shorter than Case 2b of 76.306 ft. Because the hydraulic fracture in Case 2a opened the natural fracture, the growth in y direction is restricted compared to Case 2b such that Case 2a has the shorter fracture length in y direction.

Figure 36 is the permeability map for Case 1 and 2.

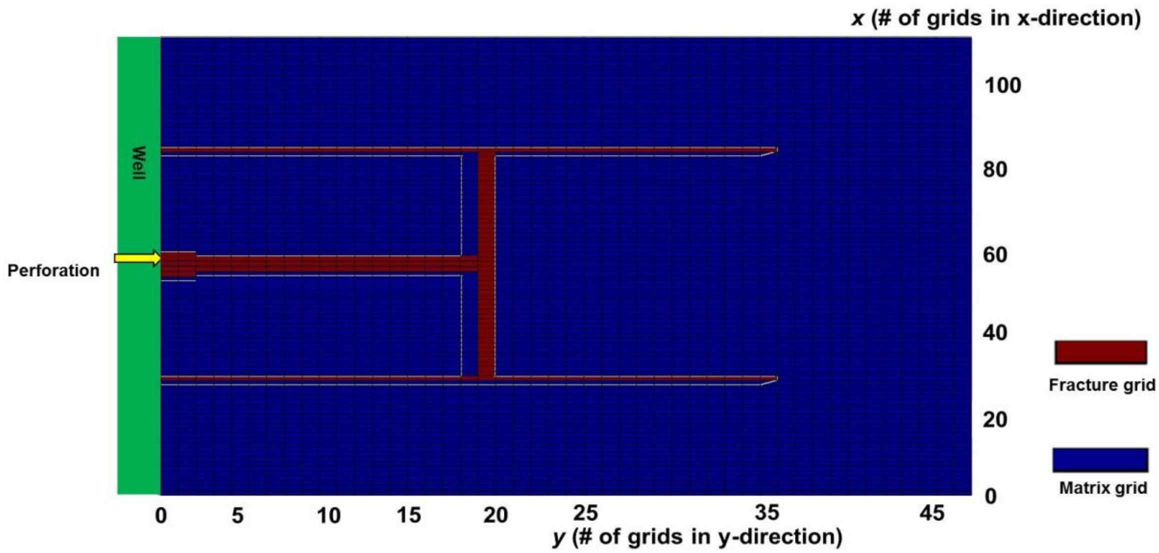

(a) Case2a

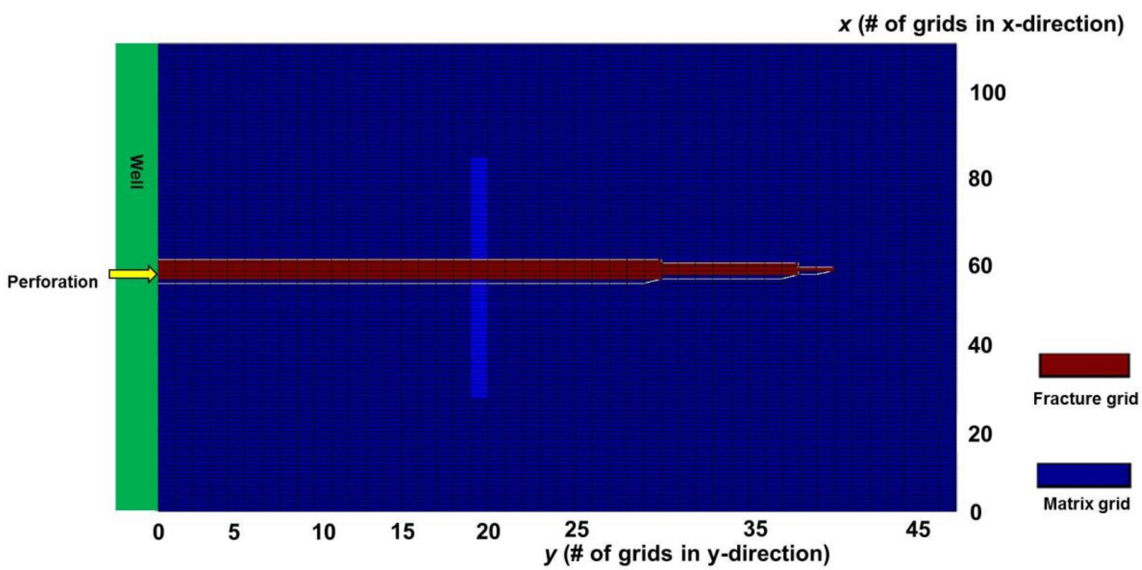

(b) Case 2b

Figure 36. Permeability maps for Cases 2a and 2b as determined by NF spacing (Step 1).

Case 2a shows an immediate opening interaction and Case 2b displayed crossing with the natural fracture closed for the entire simulation time.

In Step 2, two natural fractures are assigned parallel to the hydraulic fracture path (perpendicular to the σ_h direction) with the initiation point at the middle. We then set up the other two perpendicular natural fractures, which were opened by hydraulic fracture after the crossing. First perpendicular natural fracture was deployed from 2.198 ft far from the perforation and the second one was located at the distance of 26.4 ft from the perforation. In this setting, we investigated two cases: one with a 26.4-ft (Case 2c) distance between parallel natural fractures and the other with 264 ft in between (Case 2d). Figure 37 and 38 below show the initial geographical settings for each case. The results show that the distance between parallel natural fractures varies among cases.

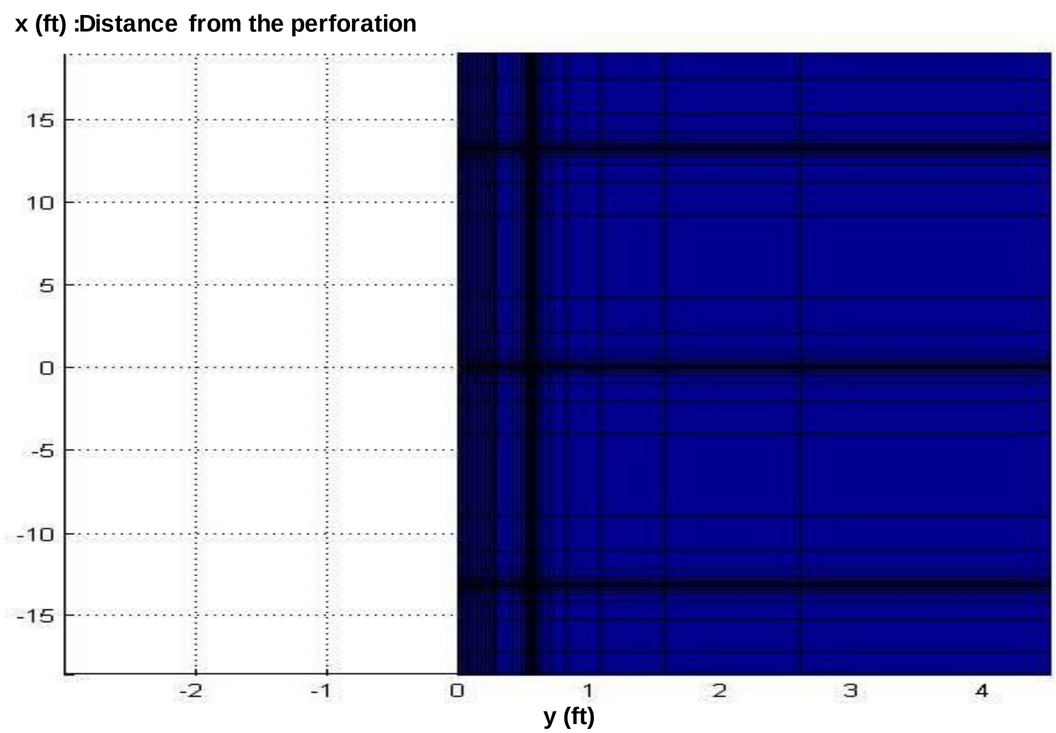

(a) Zoomed view.

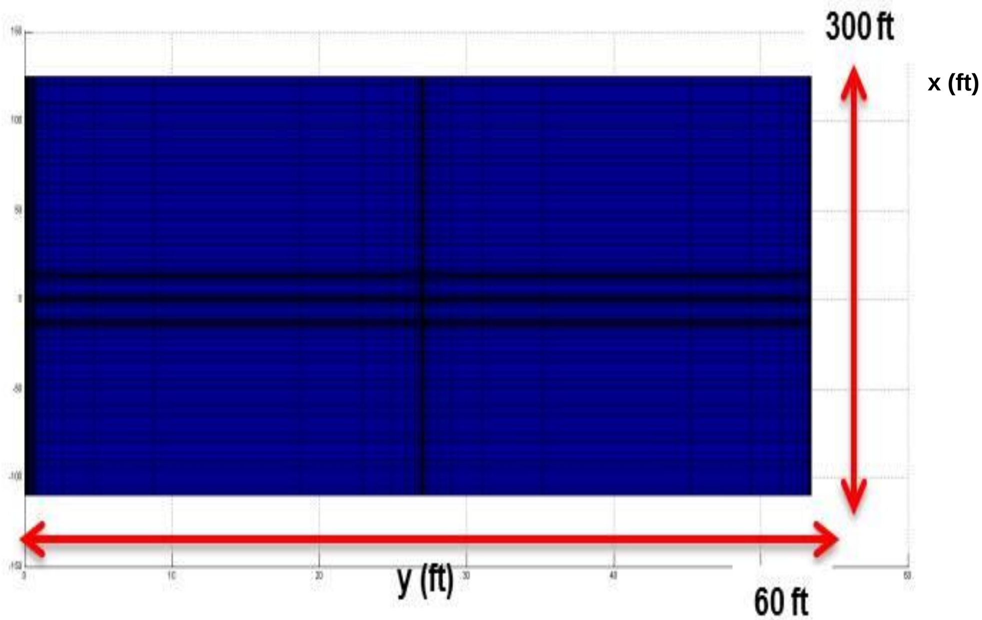

(b) Overall view.

Figure 37. (a) Zoomed and (b) overall views of NF spacing observation (Step 2) for Case 2c.

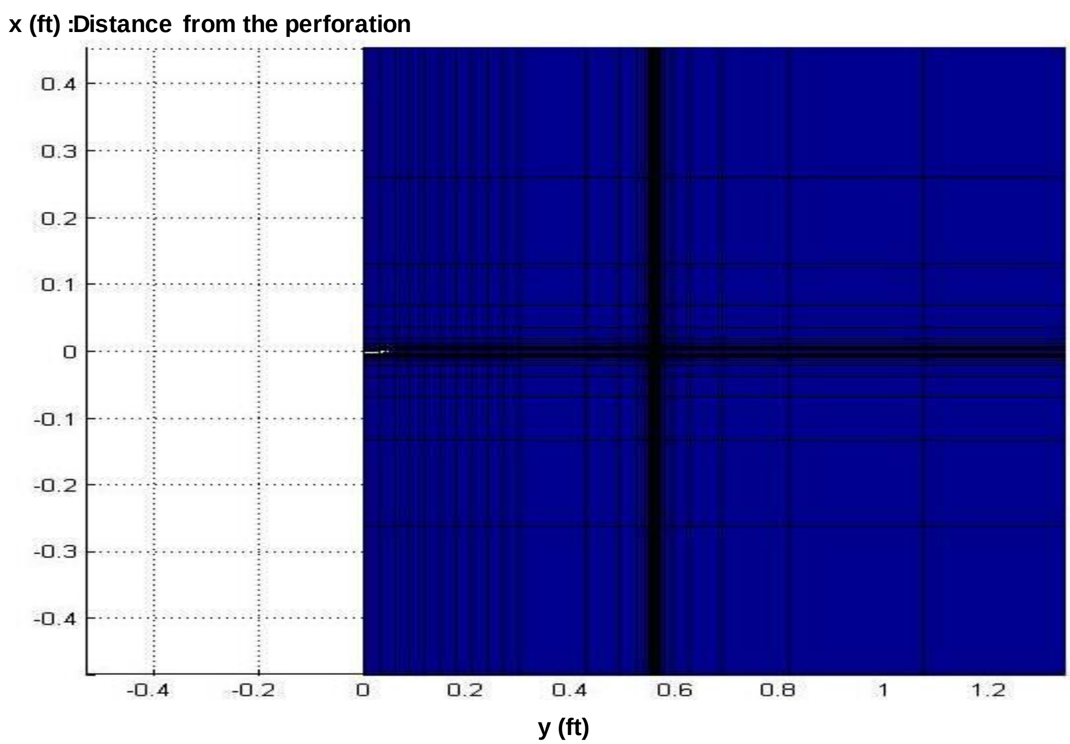

(a) Zoomed view

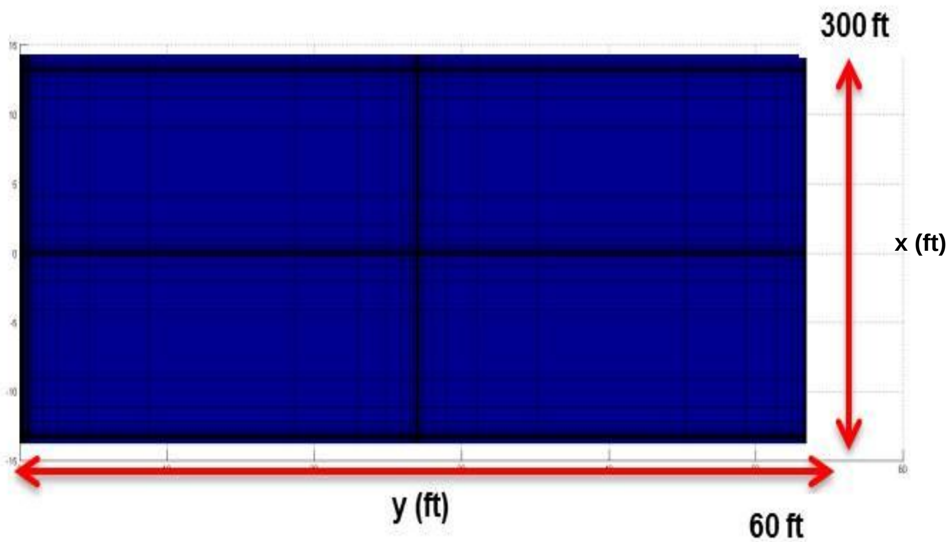

(b) Overall view

Figure 38. (a) Zoomed and (b) overall views of NF spacing observation (Step 2) for Case 2d.

The natural fractures built in Cases 2c and 2d were similar in length to the reservoir boundaries. Therefore, the dark lines in Figures 37 and 38 represent natural fractures. Table 14 presents the reservoir input data. The simulations of fracture behavior were run for 3 minutes.

Table 14. Reservoir rock and fluid input data for NF spacing observation (Step 2).

Rock and Fluid Properties	Input Data
Ky = permeability in y direction (flow direction)	0.00001 md
Kx = permeability in x direction	0.00001 md
Kynf, Kxnf = permeability of Natural Fracture	0.1 md
Φ = porosity	0.1
Φnf = porosity of NF	0.1
σ_{min} = minimum horizontal in-situ stress	2950 psia
σ_{max} = maximum horizontal in-situ stress	3000 psia
G = shear modulus of rock	2.17 x 10^{-6} psi
V = Poisson's ratio of rock	0.15
KIC = rock toughness	455
h = gross fracture height	100
μ = viscosity of fluid	0.8
Bw = FVF of frac. fluid	1.0
ρ = density of fluid	62.4 lb/cu.ft
Cw = compressibility of water	5.00 x 10^{-6} psi^{-1}
Wini = initial width of fracs	Matrix=0.002ft, NF=0.002ft
Initial reservoir P =	2000 psi
Flow rate Q =	10 bpm

Figure 39 depicts the permeability maps for Case 2c and numbers each fracture created. From the figure, we can see that the simulation created multiple fractures. The fracture induced by the well block first crosses each perpendicular natural fracture and then dilates it when the fluid pressure is sufficient. Opened Fracture #1 and #2 were both created in this manner. When Opened Fracture #1 reaches parallel natural fractures, Opened Fracture #1 begins to dilate the parallel natural fracture, which is denoted as Opened Fracture #3.

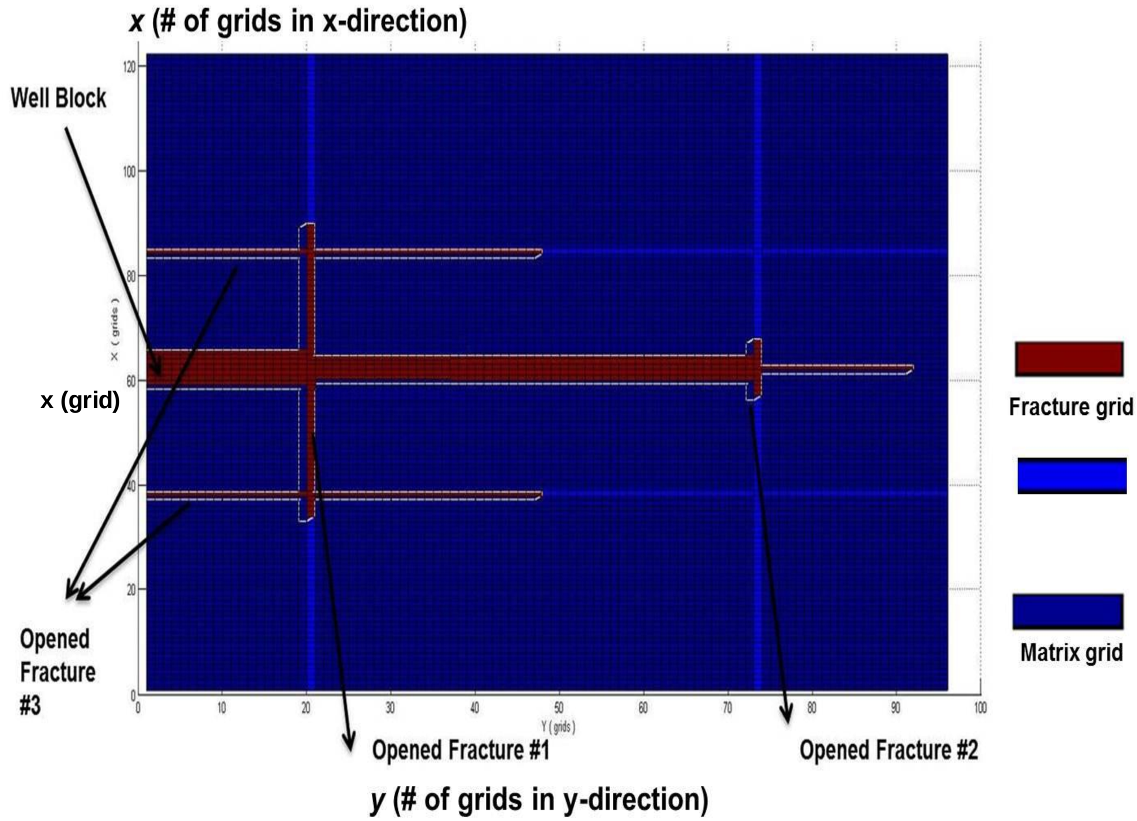

Figure 39. . Permeability map of the reservoir and created fracture index for NF spacing case study (Step 2, Case 2c).

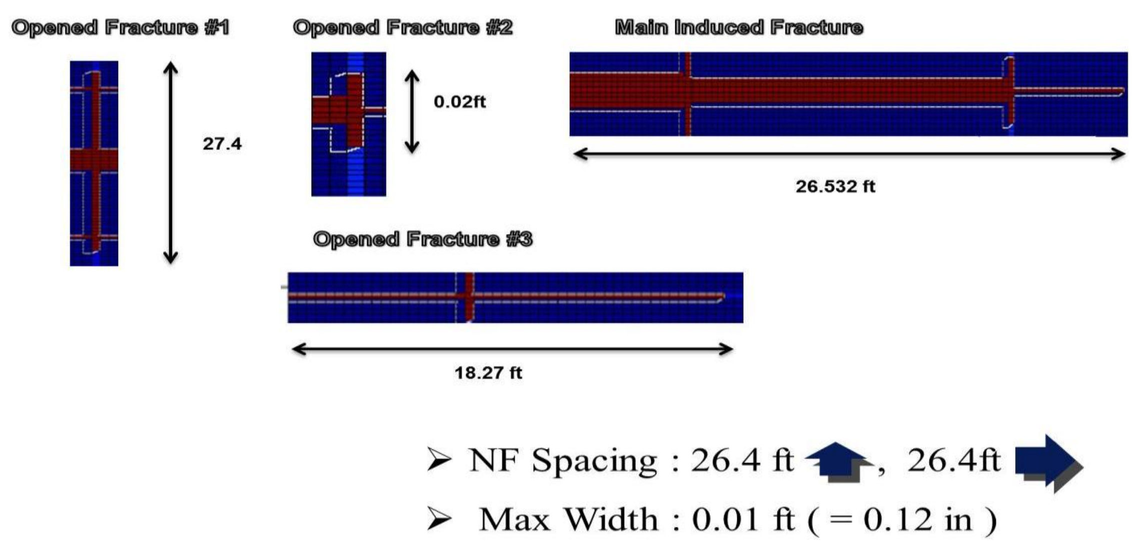

Figure 40. Fracture geometry details for NF spacing case study (Step 2, Case 2c).

Figure 40 shows all the geomechanical details for Case 2c simulation. Opened Fracture #1 continues to extend over Opened Fracture #3.

Figure 41 shows the permeability map for Case 2d and numbers each fracture created. Because the parallel natural fractures are far away from the induced fracture, Case 2d yielded simpler geometry that Case 2c. Figure 42 describes each fracture created separately. Opened Fracture #1 from Case 2c and Opened Fracture #4 are the first dilated natural fractures in their respective simulations, but there is a key difference. Opened Fracture #1, which was created from the first intersection, also creates Opened Fracture #3; the sum of both lengths is 45.67 ft. However, the length of Opened Fracture #4, which is the only fracture extending from the first intersection, is 32.82 ft. This large difference shows that a parallel natural fracture opens more easily than a perpendicular one. In addition, the width of the main fracture body is narrower than that of Case 2d after is passes the first natural fracture. The dilation of Opened Fracture #3 may have caused this difference.

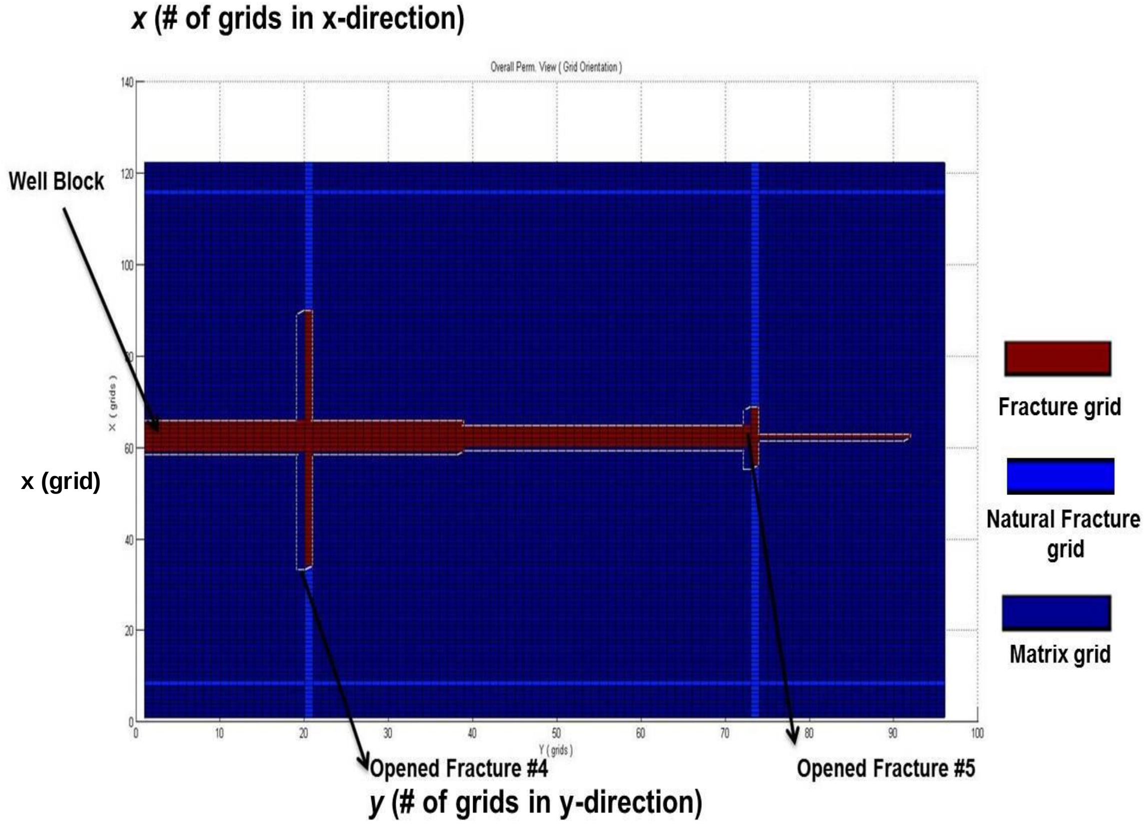

Figure 41. Permeability map of the reservoir and fracture index for the NF spacing case study (Step 2, Case 2d).

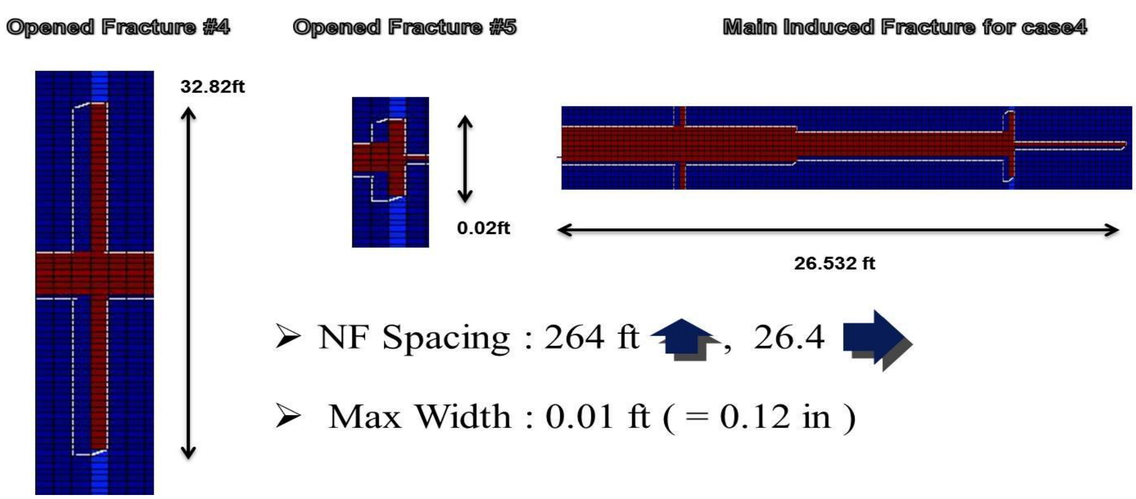

Figure 42. Fracture geometry details for NF spacing case study (Step 2, Case 2d).

From the results in this section (5.2), we investigated the effect of natural fracture spacing. In Step 1, smaller the distance from the perforation (Case 2a) had the opening behavior when the hydraulic fracture interacted with the natural fracture. In Equation 25, L_f is at the denominator of K_{IC} such that shorter length strengthens the effect of rock toughness to have similar result as the case having a large rock toughness; thus the natural fractures insects with the hydraulic fracture at the short distance has the tendency to be opened. The narrow spacing in parallel natural fractures at Case 2c in Step 2 showed another opening behavior. Compared to the opening of the natural fracture lay perpendicular to σ_H, the natural fractures in the direction perpendicular to σ_h opened much faster.

5.3 Effect of Stress Anisotropy

Stress anisotropy is the last factor investigated in this study. The minimum propagation pressure derived from Equation 25 can vary depending on the difference between σ_h and σ_H. We therefore investigated stress anisotropy, which can be understood as $\sigma_H - \sigma_h$.

The case study for stress anisotropy was performed in a simple, perpendicular, natural fracture system to see how stress anisotropy contributes to opening and/or crossing behavior.

Using the same initial settings as used for Case 2a in the natural fracture spacing case study (Step 1), we performed two simulations with stress anisotropy of 10 and 500, respectively, for 10 minutes. Table 15 shows the relevant input data; Figure 43 illustrates the permeability map for Cases 3a and 3b.

Table 15. Reservoir input data for the stress anisotropy case study (Section 5.3).

Rock and Fluid Properties	Input Data
Ky = permeability in y direction (flow direction)	0.00001 md
Kx = permeability in x direction	0.00001 md
Kynf, Kxnf = permeability of Natural Fracture	0.1 md
Φ = porosity	0.1
Φnf = porosity of NF	0.1
σ_{min} = minimum horizontal in-situ stress	2950 psia
σ_{max} = maximum horizontal in-situ stress	Case1= 2960 psia Case2=3450 psia
G = shear modulus of rock	2.17 x 10^{-6} psi
V = Poisson's ratio of rock	0.15
KIC = rock toughness	455
h = gross fracture height	100
μ = viscosity of fluid	0.8
Bw = FVF of frac. fluid	1.0
ρ = density of fluid	62.4 lb/cu.ft
Cw = compressibility of water	5.00 x 10^{-6} psi^{-1}
Wini = initial width of fracs	Matrix=0.005ft, NF=0.005ft
Initial reservoir P =	2000 psi
Flow rate Q =	10 bpm

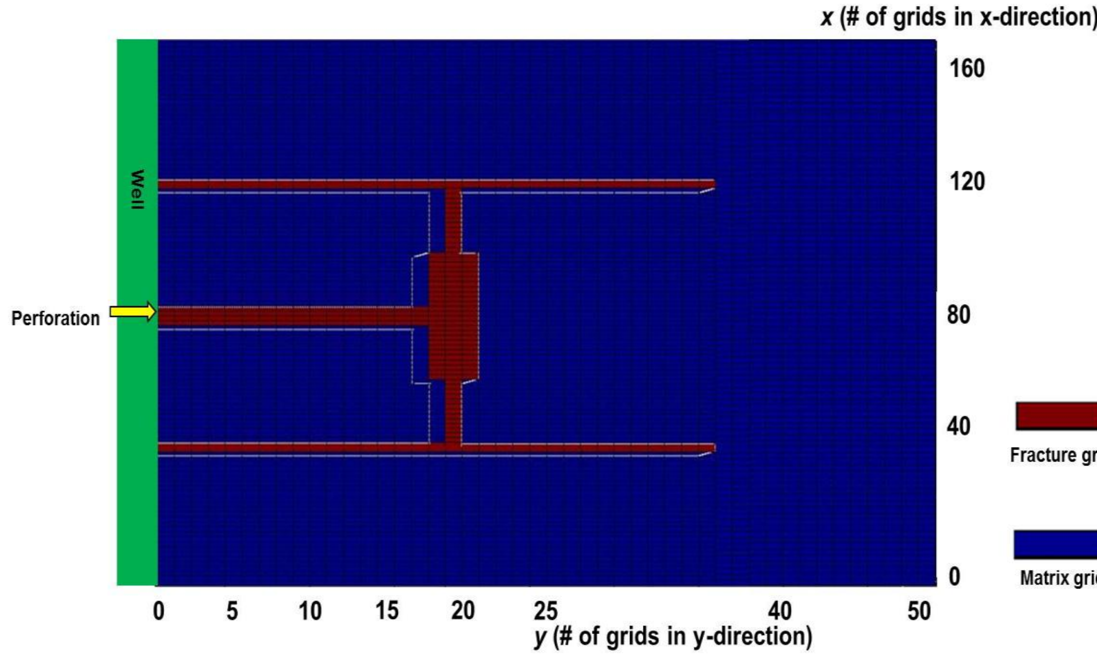

(a) Case 3a with stress anisotropy of 10 psi

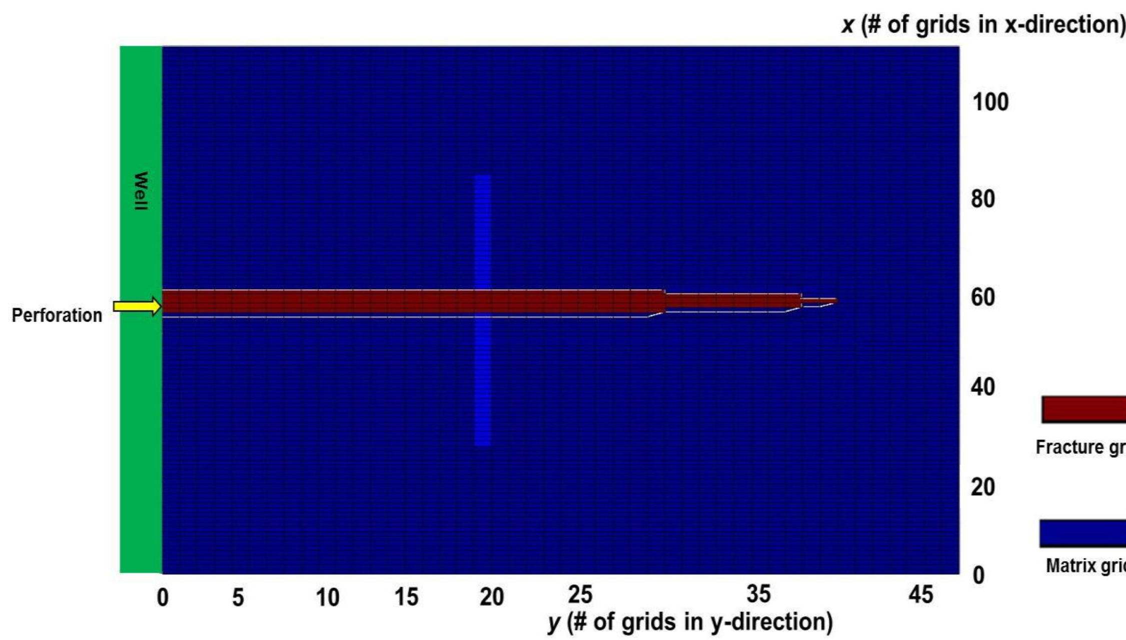

(b) Case 3b with stress anisotropy of 500 psi

Figure 43. Permeability maps for Cases 3a and 4b, from the stress anisotropy case study (Section 5.3).

Case 3a showed the opening behavior when the hydraulic fracture interacts with the natural fracture. Case 3b simply propagates across the natural fracture and it shows identical geometry as the fracture created at Case 2b. This may occurred because the minimum propagation pressures chosen at the intersection were different at Case 3a and 3b. Figures 36 (a) and 43 (a) can also be compared, because both figures are derived from the same condition with different degrees of stress anisotropy. Figure 43 (a) displays a width expansion that is not observed in Figure 36 (a). The result depicted in Figure 36 (a) was generated using stress anisotropy of 50 psi such that the width calculated using Equation 28 was reduced compared to that calculated for Figure 43 (a).

5.4 A Complex Natural Fracture System

In this section, we investigate how the fracture network is created through the influence of natural fractures inside the reservoir. The initial geomechanical conditions for this section are illustrated in Figure 44. The first perpendicular natural fracture is located 0.06 ft from the initiating grid block. All of the remaining perpendicular natural fractures are located 26.4 ft from the perpendicular natural fracture. Parallel natural fractures were therefore spaced at 13.2 ft. Therefore, we have 11 parallel natural fractures and 8 perpendicular natural fractures, which yield a total boundary of 211.26 ft by 132 ft. The lines in Figure 44 represent natural fractures.

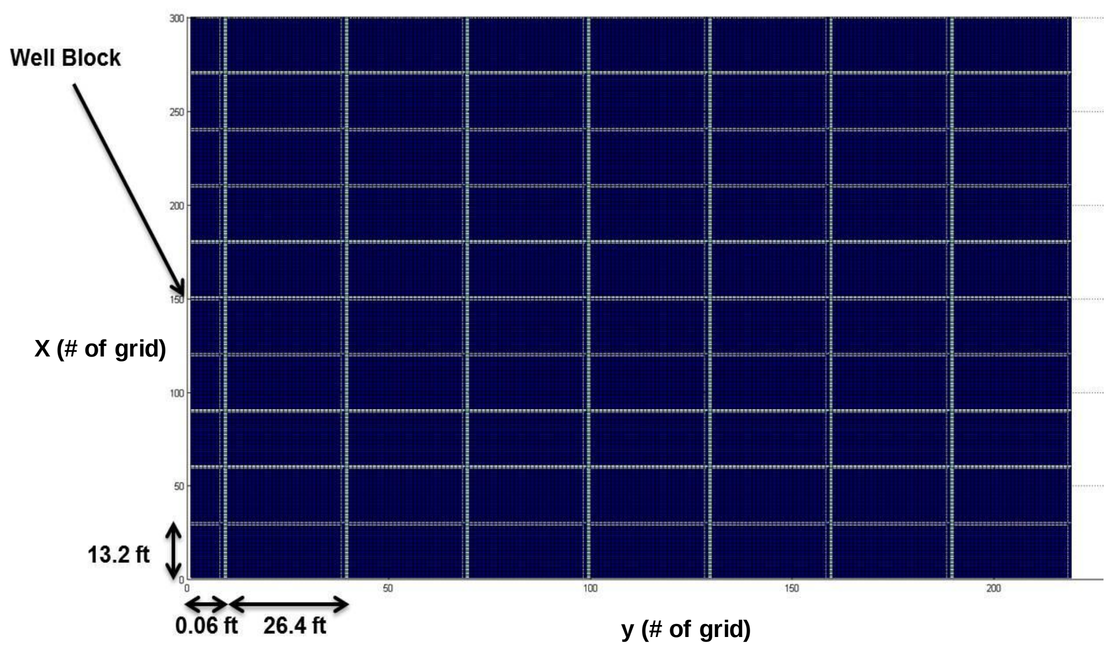

Figure 44. Initial geomechanical conditions for the complex network simulation.

Table 16 shows rock and fluid input data for the 36-minute simulation. To speed the simulation, we set the rock toughness to zero and stress anisotropy to 50 psia, which achieved a complex fracture in less running time.

Table 16. Rock and fluid data for the complex network system.

Rock and Fluid Properties	Input Data
Ky = permeability in y direction (flow direction)	0.00001 md
Kx = permeability in x direction	0.00001 md
Kynf, Kxnf = permeability of Natural Fracture	0.1 md
Φ = porosity	0.1
Φnf = porosity of NF	0.1
σ_{min} = minimum horizontal in-situ stress	2950 psia
σ_{max} = maximum horizontal in-situ stress	3000 psia
G = shear modulus of rock	2.17 x 10^{-6} psi
V = Poisson's ratio of rock	0.15
KIC = rock toughness	0
h = gross fracture height	50
μ = viscosity of fluid	0.8
Bw = FVF of frac. fluid	1.0
ρ = density of fluid	62.4 lb/cu.ft
Cw = compressibility of water	5.00 x 10^{-6} psi^{-1}
Wini = initial width of fracs	Matrix=0.002ft, NF=0.002ft
Initial reservoir P =	2000 psi
Flow rate Q =	10 bpm

Figure 44 comprises a series of permeability maps at different time-points. It demonstrates the fracture geometry change over time.

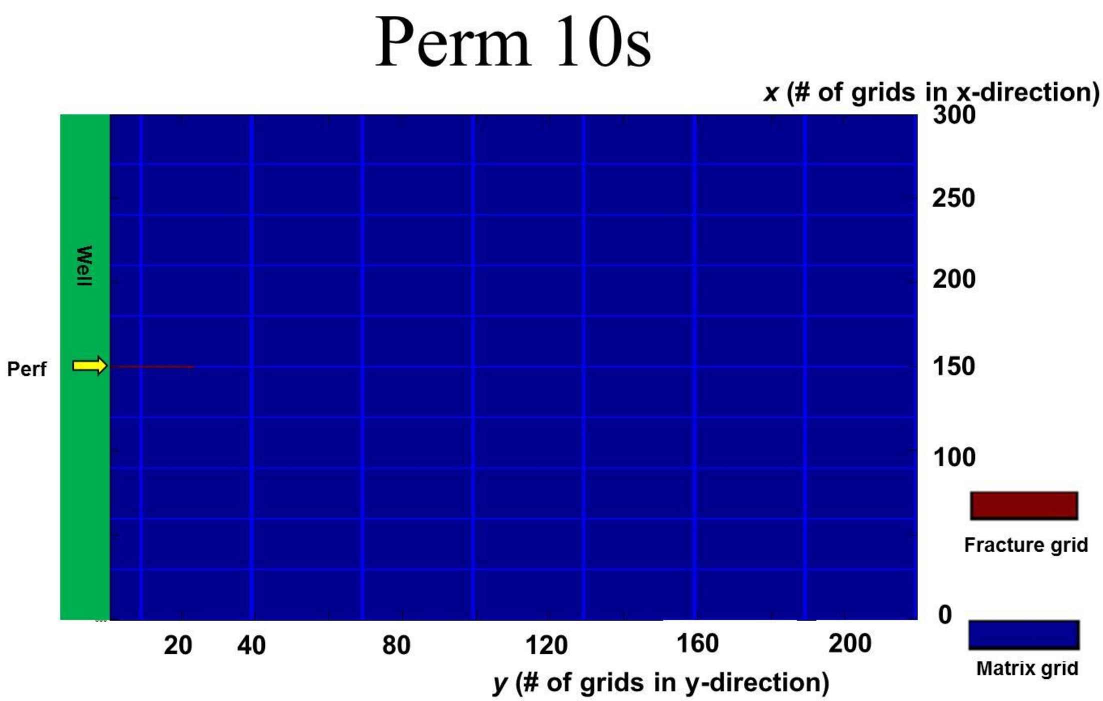

Perm 10s
x (# of grids in x-direction)
300
250
200
150
100
0
Well
Perf
20
40
80
120
160
200
y (# of grids in y-direction)
Fracture grid
Matrix grid

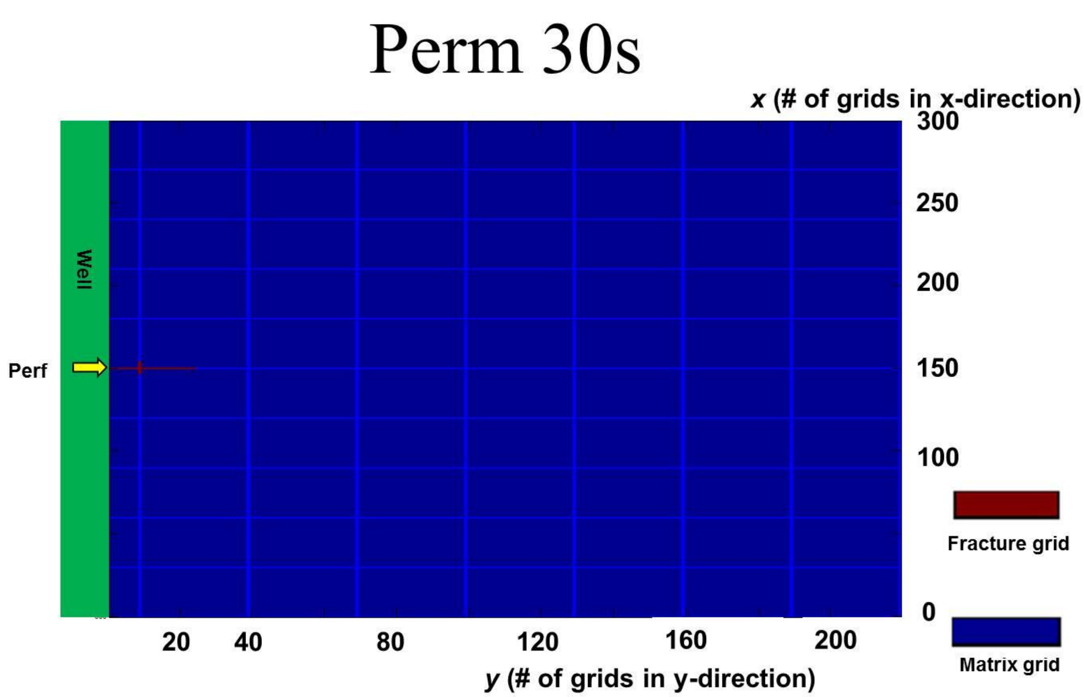

Perm 30s
x (# of grids in x-direction)
300
250
200
150
100
0
Well
Perf
20
40
80
120
160
200
y (# of grids in y-direction)
Fracture grid
Matrix grid

Perm 1min

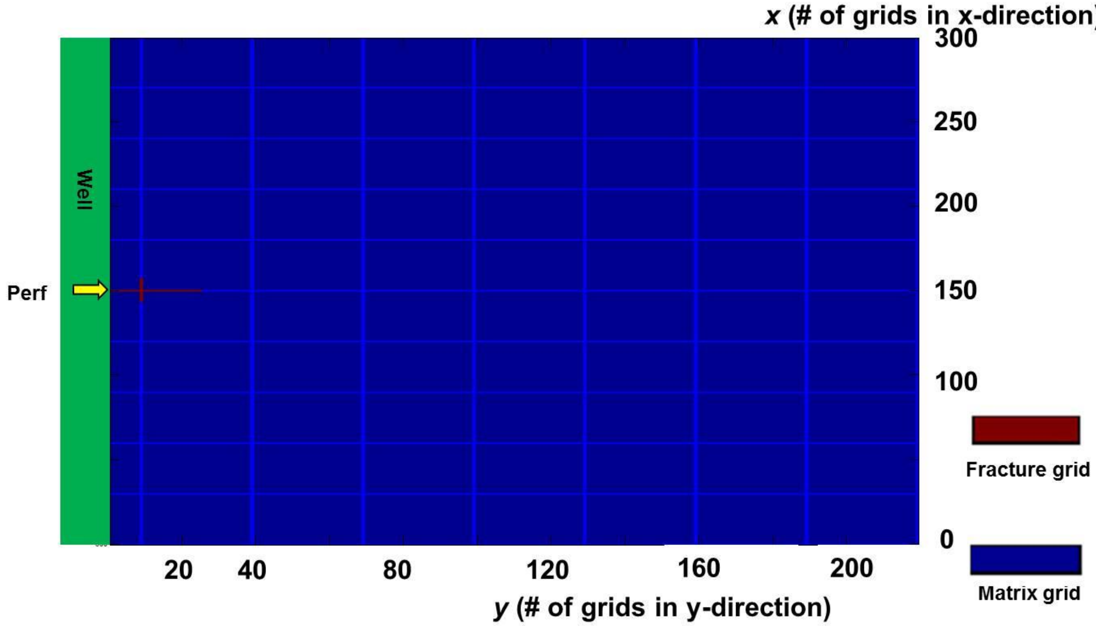

Perm 2min

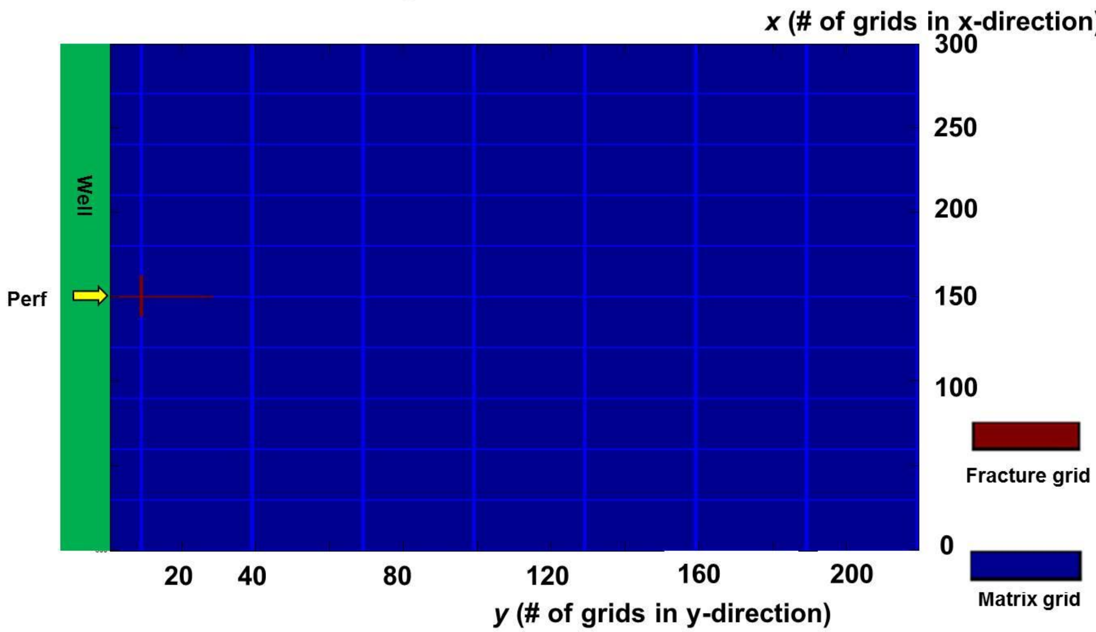

Perm 3min

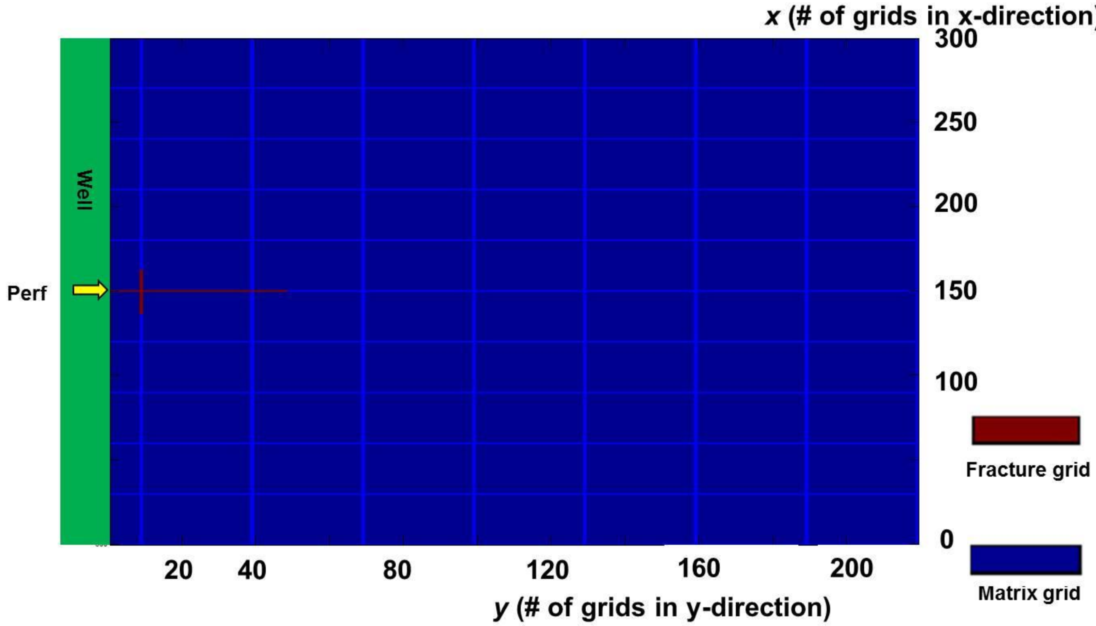

Perm 5min

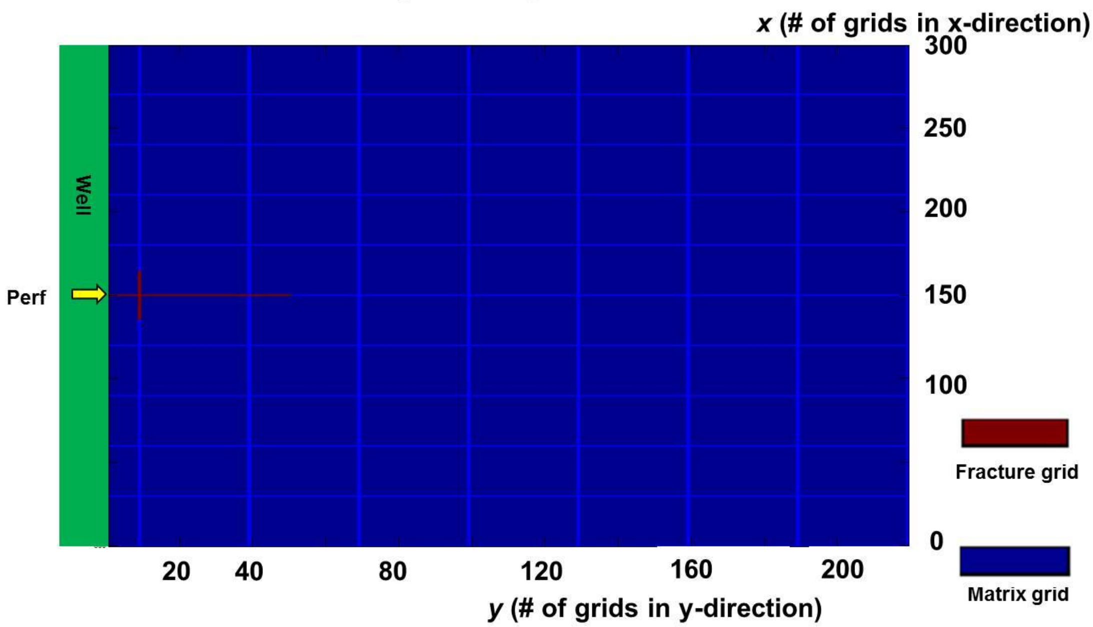

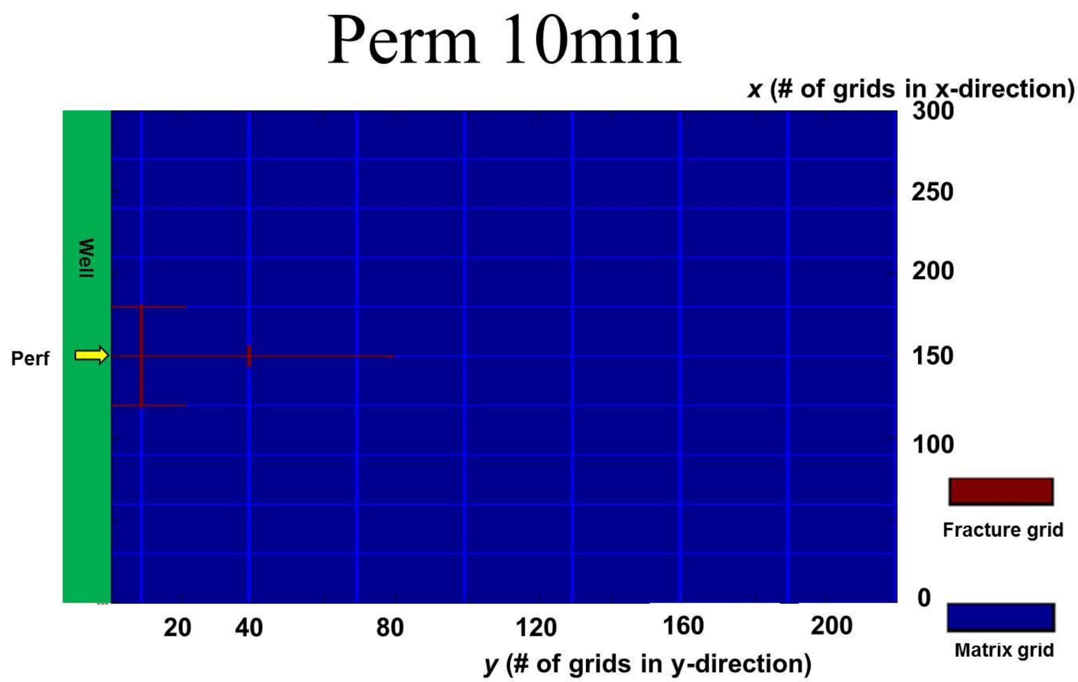
Perm 10min
x (# of grids in x-direction)
300
250
200
150
100
0
Well
Perf
20
40
80
120
160
200
y (# of grids in y-direction)
Fracture grid
Matrix grid

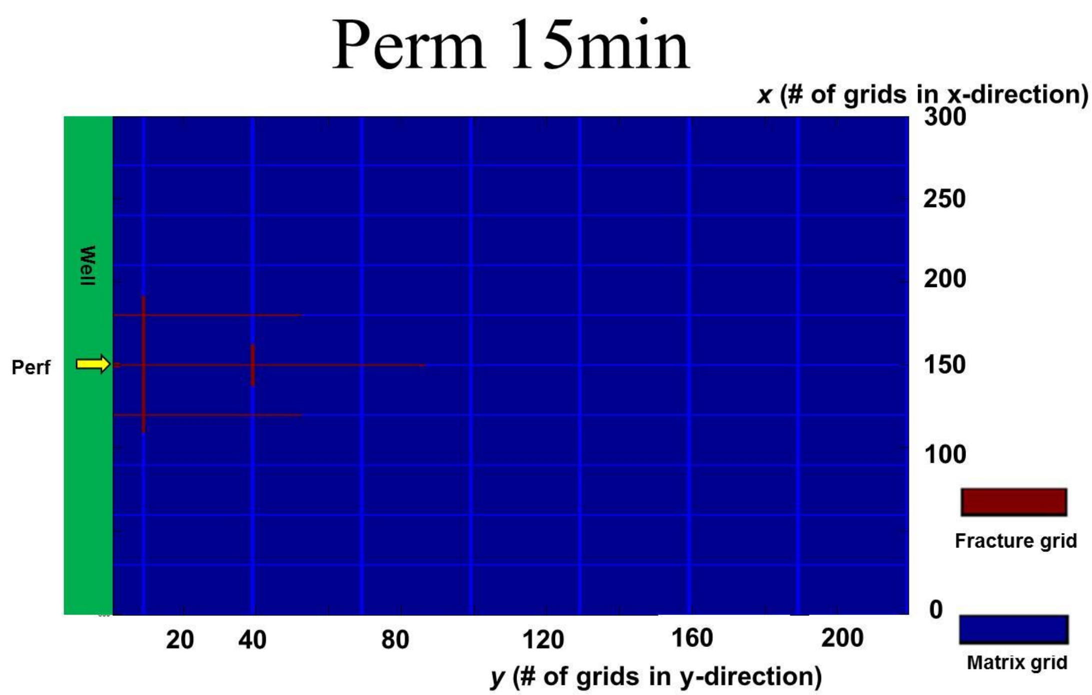
Perm 15min
x (# of grids in x-direction)
300
250
200
150
100
0
Well
Perf
20
40
80
120
160
200
y (# of grids in y-direction)
Fracture grid
Matrix grid

Perm 20min

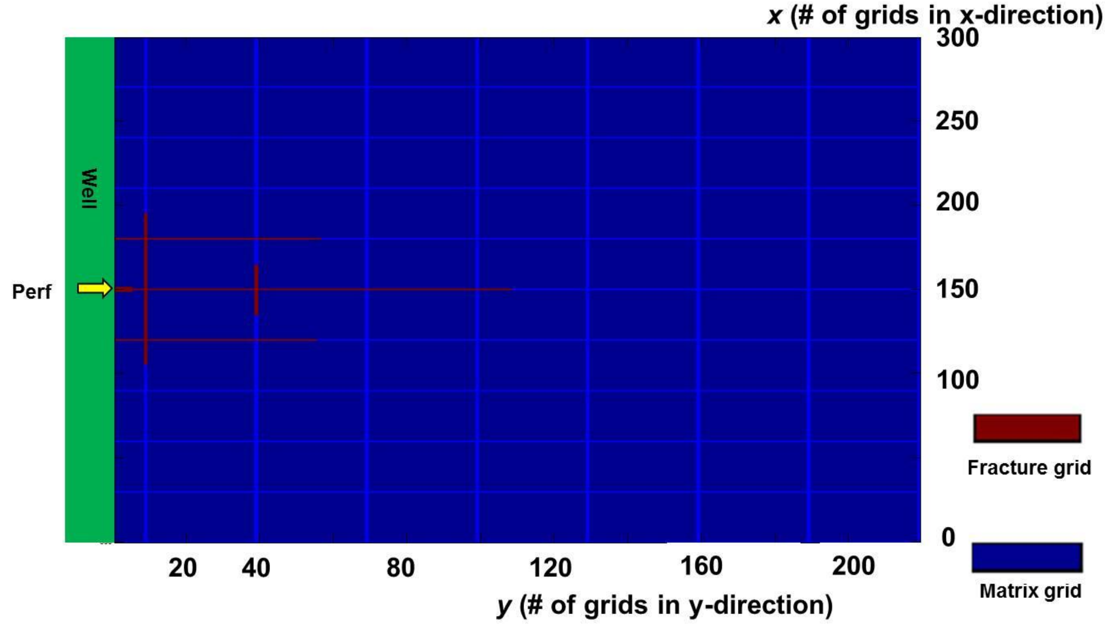

Perm 25min

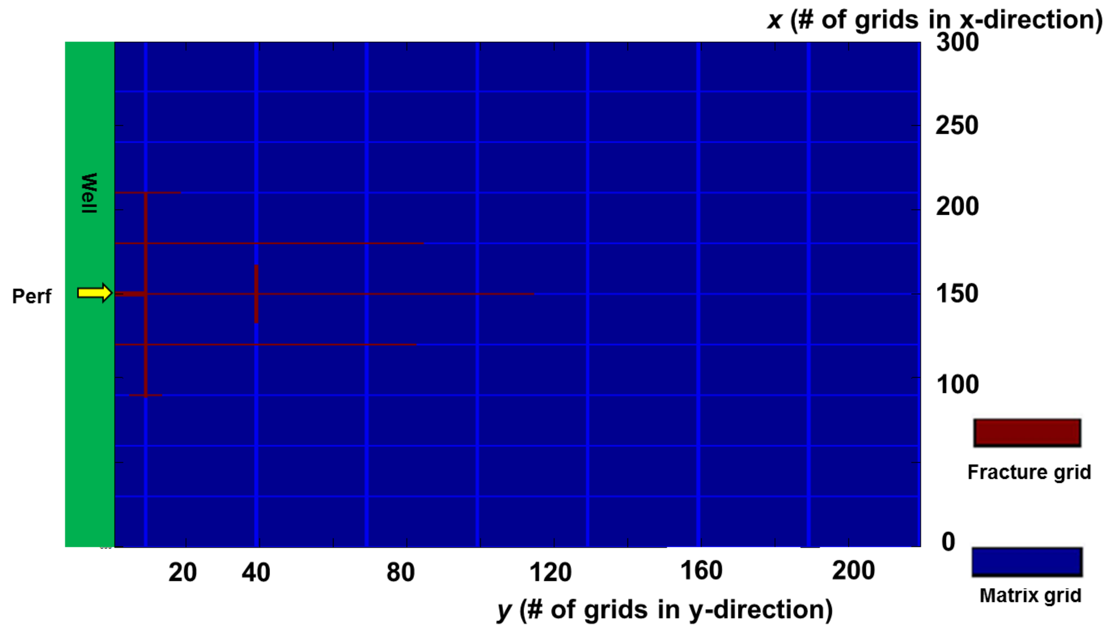

Perm 30min

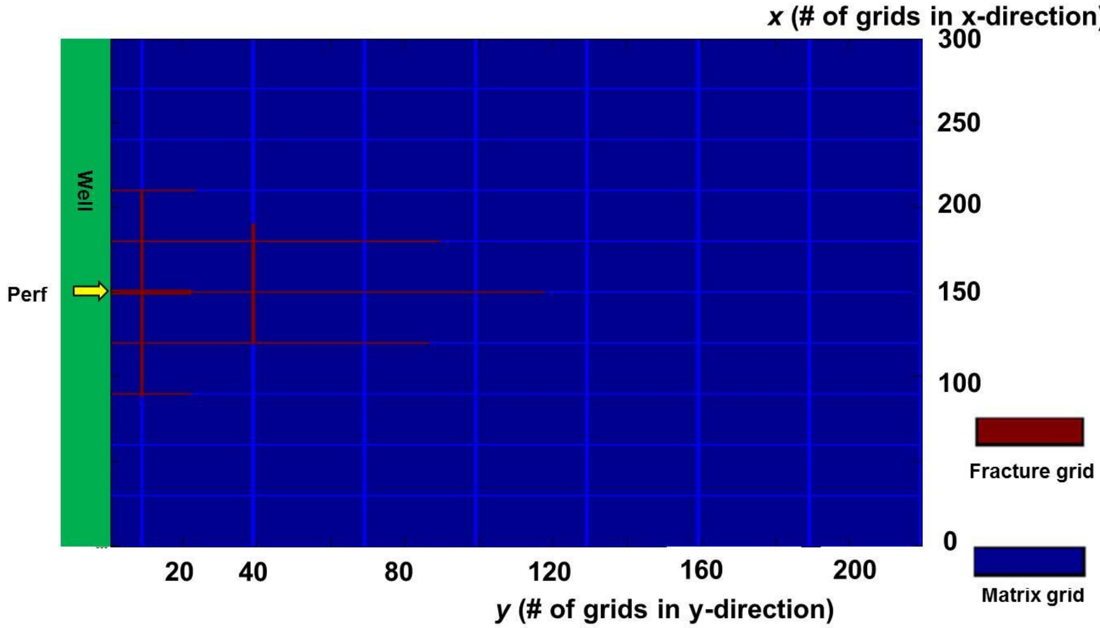

Perm 35min

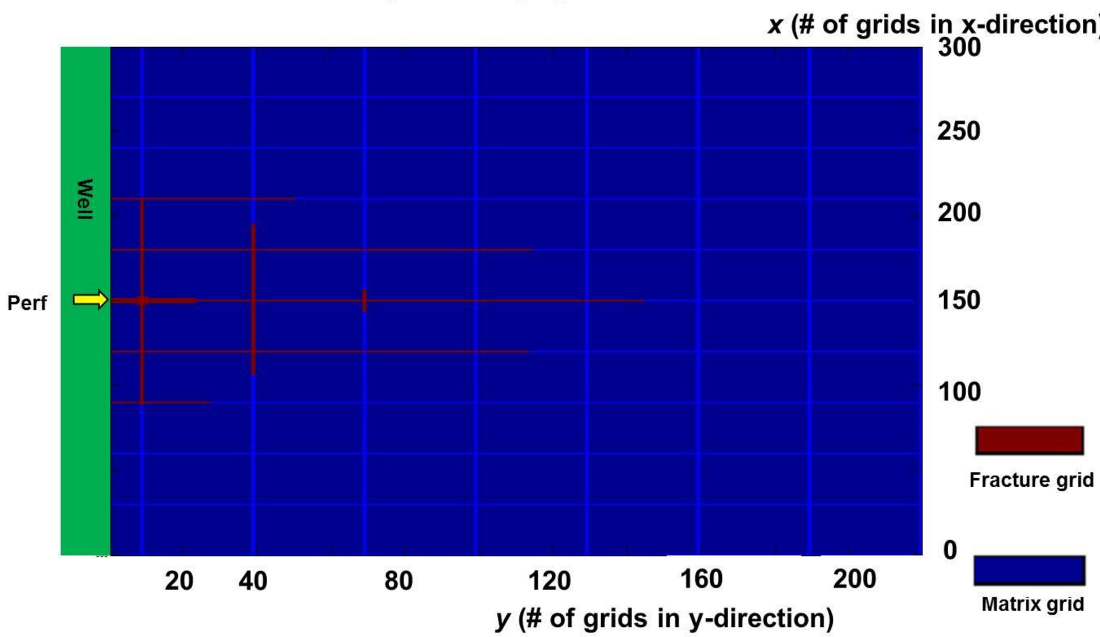

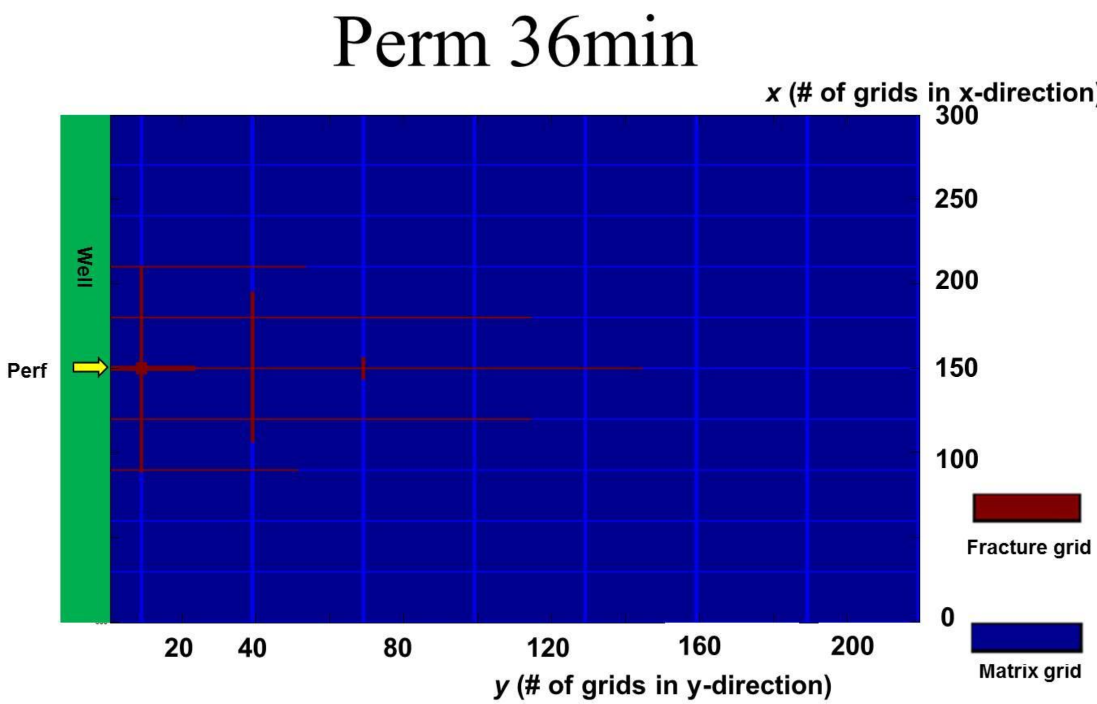

Figure 45. Permeability maps from the complex network simulation, obtained at different time-points.

Through these maps, we were able to dynamically investigate how the complex fracture network was created. The result from 10 seconds shows the fracture propagates through the first natural fracture and opens it at about 30 seconds. After 20 minutes of treatment, width expansion is observed. Width expansion occurs this late because rock toughness was set to zero. In other words, the fracture immediately propagates in either direction when fluid pressures at the tip exceed σ_h or σ_H. Therefore, fracture tends to propagate further than width expansion. By comparing the maps from the 5-minute and 10-minute time-points, it is obvious that parallel natural fractures open faster than perpendicular ones. Between 10 and 15 minutes, the first perpendicular natural fracture was re-initiated from the intersection with the first parallel natural fractures. The 25-minute map illustrates the opening of the second parallel natural fracture. The final permeability map obtained at 36 minutes illustrates a complex fracture network with nine fracture tips propagating simultaneously. The longest fracture in the *y* direction from this simulation was 119 ft; in the *x* direction, the longest fracture was 52.8 ft. The 36-minute map also shows that width expansion is more likely in the *y* direction, which proves the existence of stress anisotropy of 50 psi.

Figure 46 is a set of pressure maps for corresponding time-points.

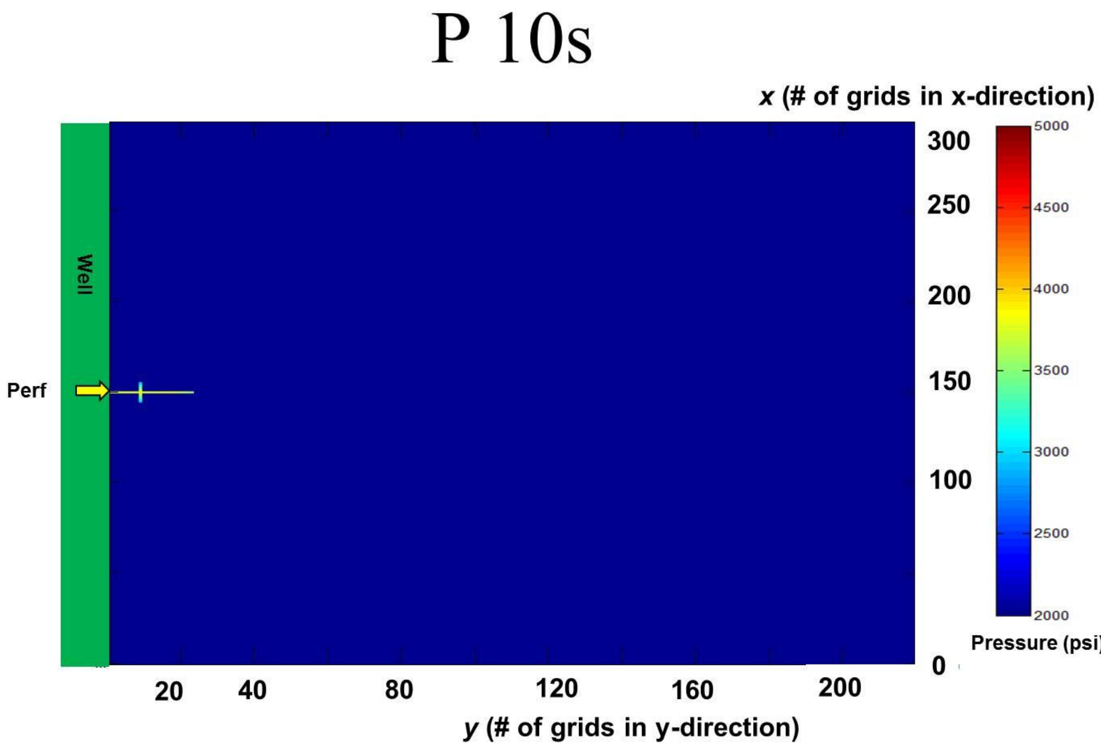

P 30s

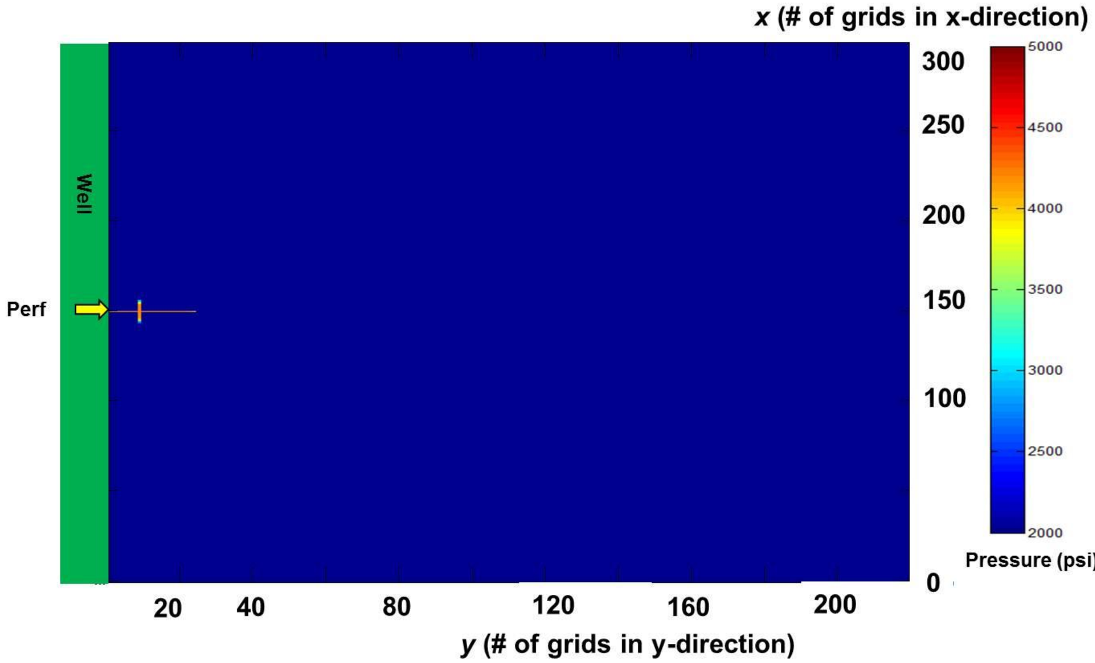
x (# of grids in x-direction)
300
250
200
150
100
0
Well
Perf
20
40
80
120
160
200
y (# of grids in y-direction)
5000
4500
4000
3500
3000
2500
2000
Pressure (psi)

P 1min

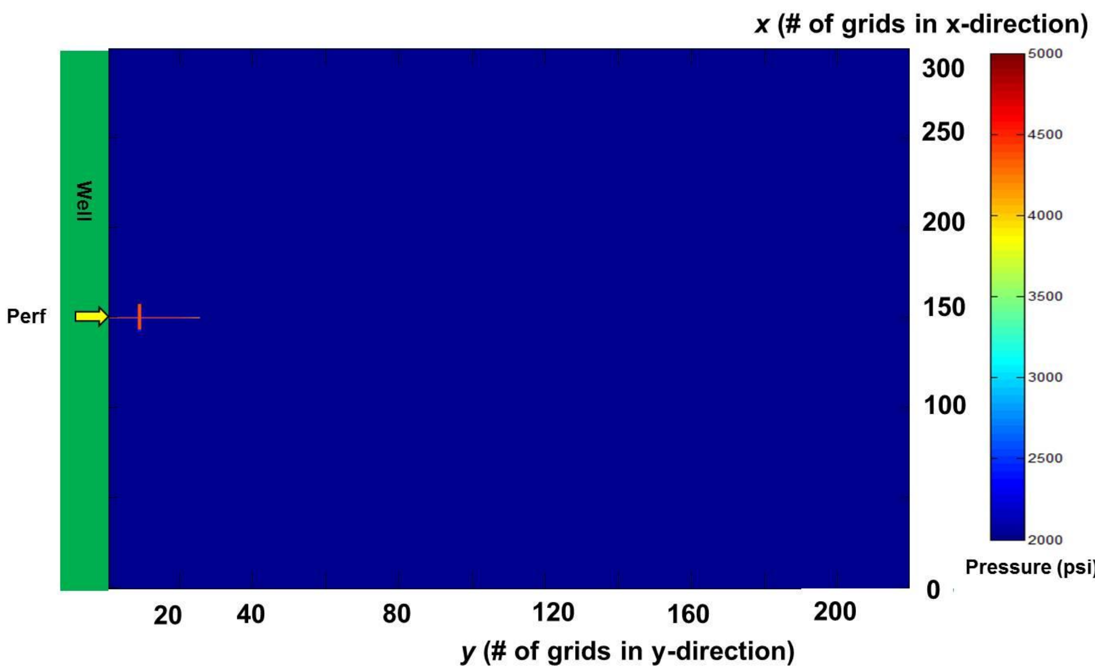
x (# of grids in x-direction)
300
250
200
150
100
0
Well
Perf
20
40
80
120
160
200
y (# of grids in y-direction)
5000
4500
4000
3500
3000
2500
2000
Pressure (psi)

P 2min

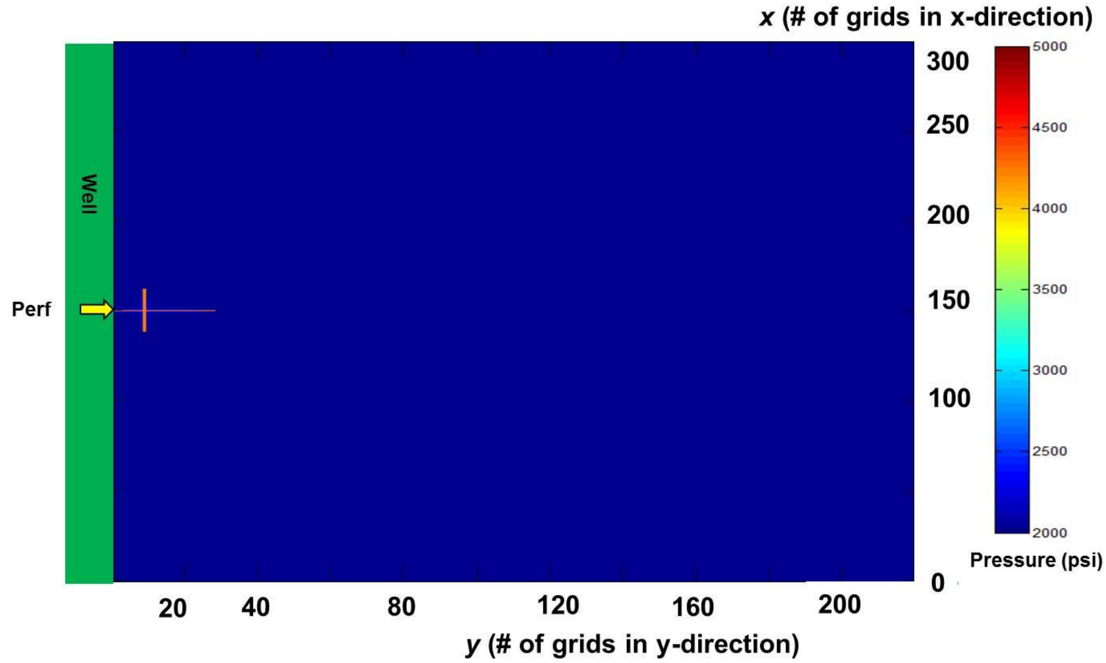
x (# of grids in x-direction)
300
250
200
150
100
0
Well
Perf
20
40
80
120
160
200
y (# of grids in y-direction)
5000
4500
4000
3500
3000
2500
2000
Pressure (psi)

P 3min

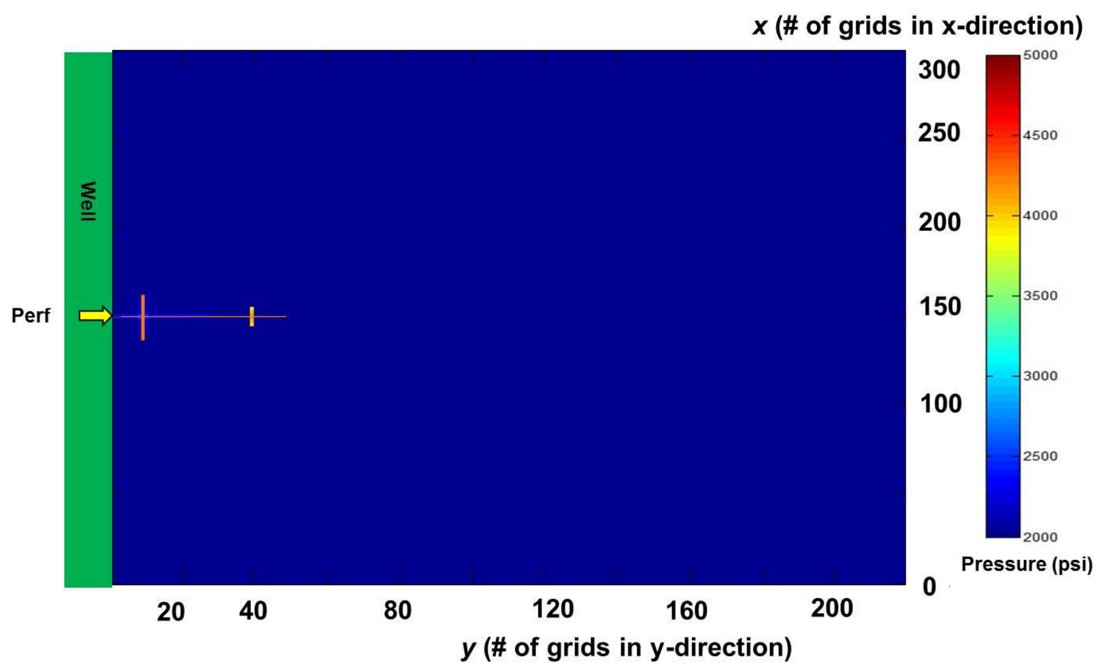
x (# of grids in x-direction)
300
250
200
150
100
0
Well
Perf
20
40
80
120
160
200
y (# of grids in y-direction)
5000
4500
4000
3500
3000
2500
2000
Pressure (psi)

P 5min

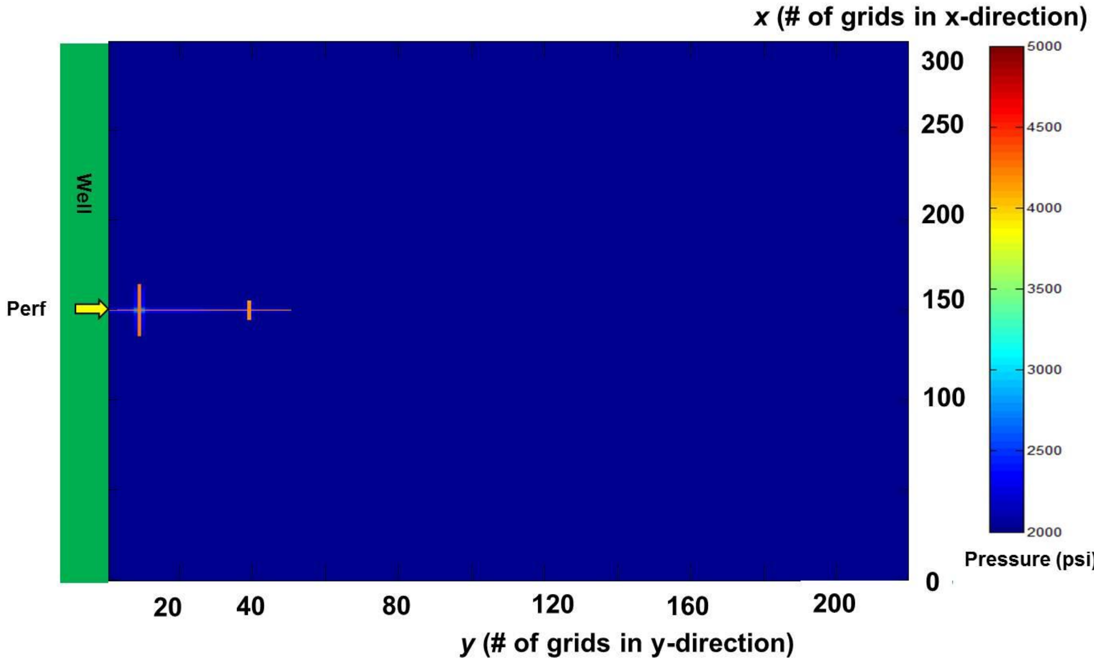

P 10min

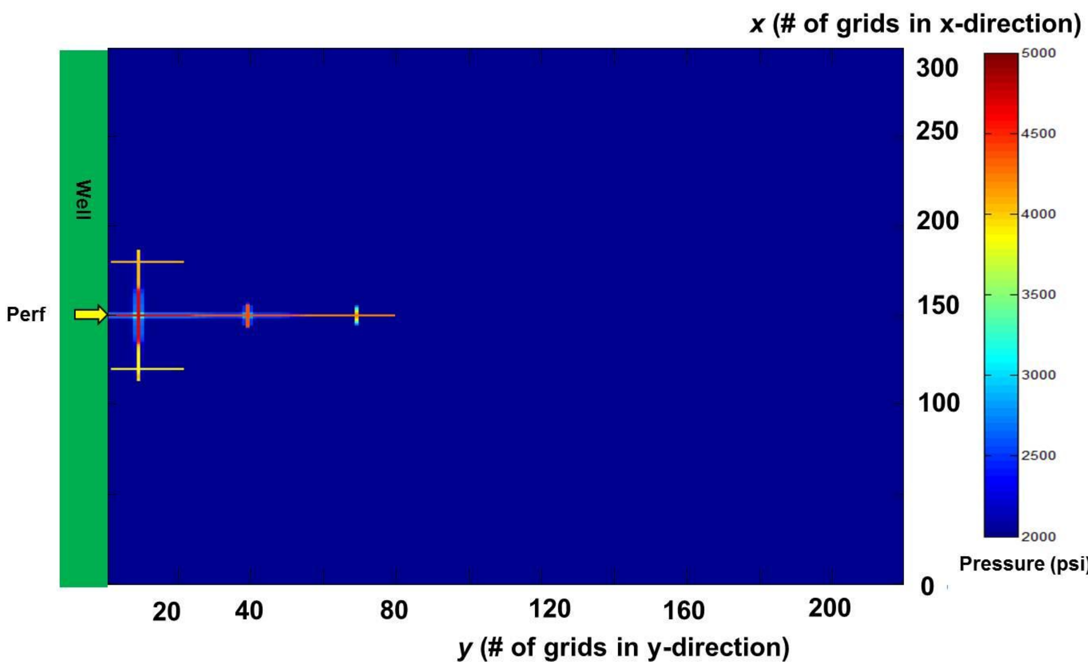

P 15min

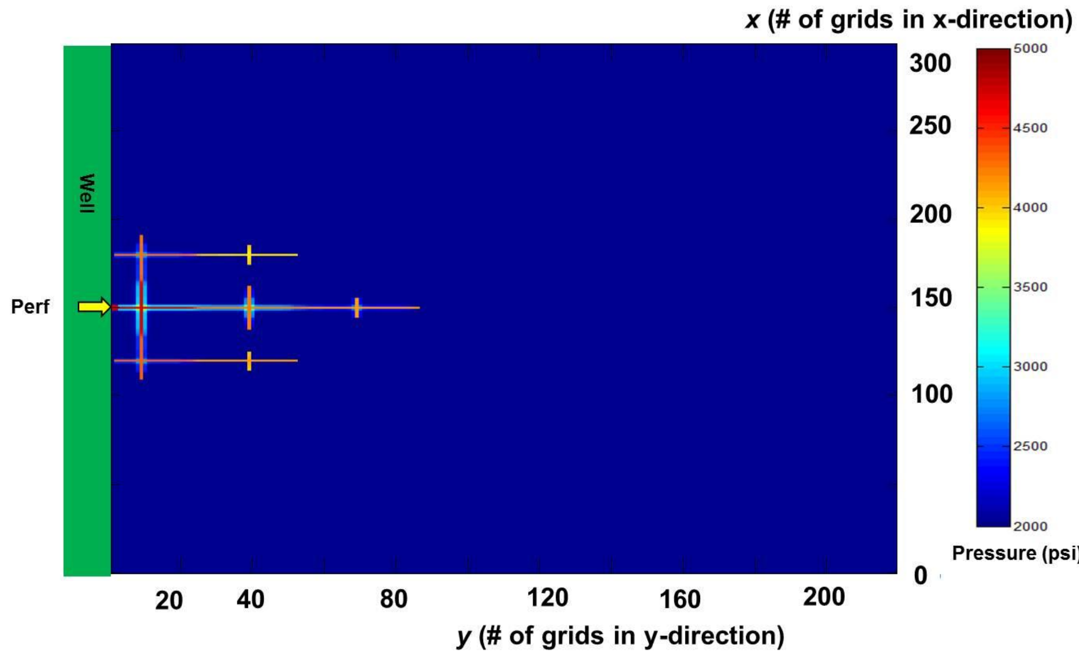

P 20min

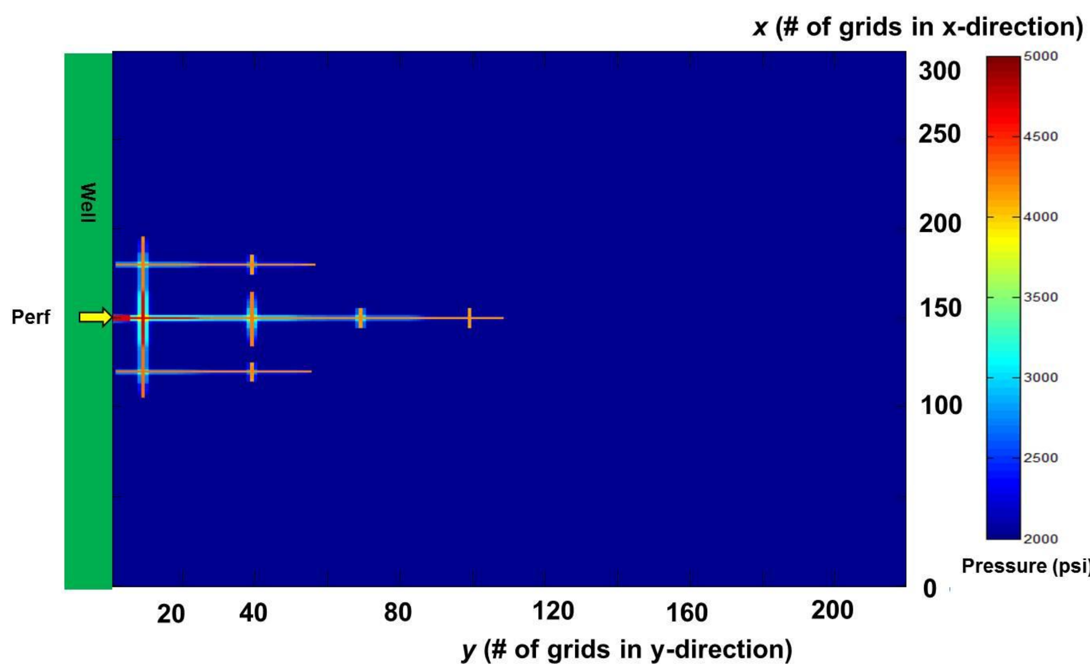

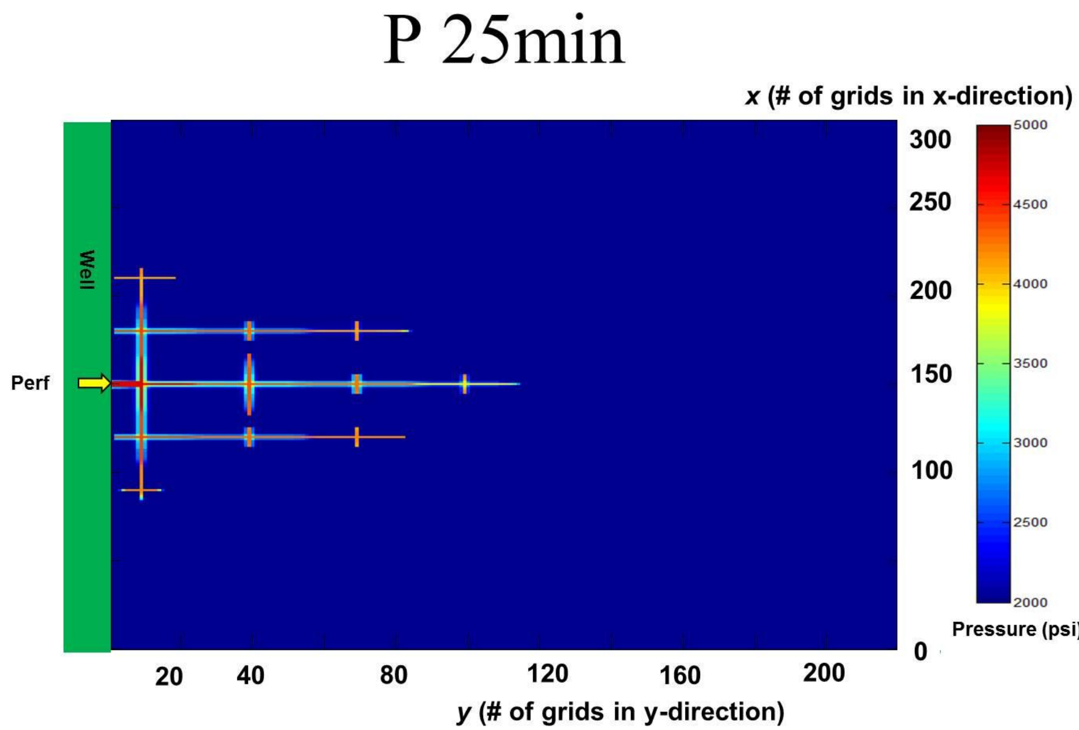
P 25min
x (# of grids in x-direction)
300
250
200
150
100
0
Well
Perf
5000
4500
4000
3500
3000
2500
2000
Pressure (psi)
20
40
80
120
160
200
y (# of grids in y-direction)

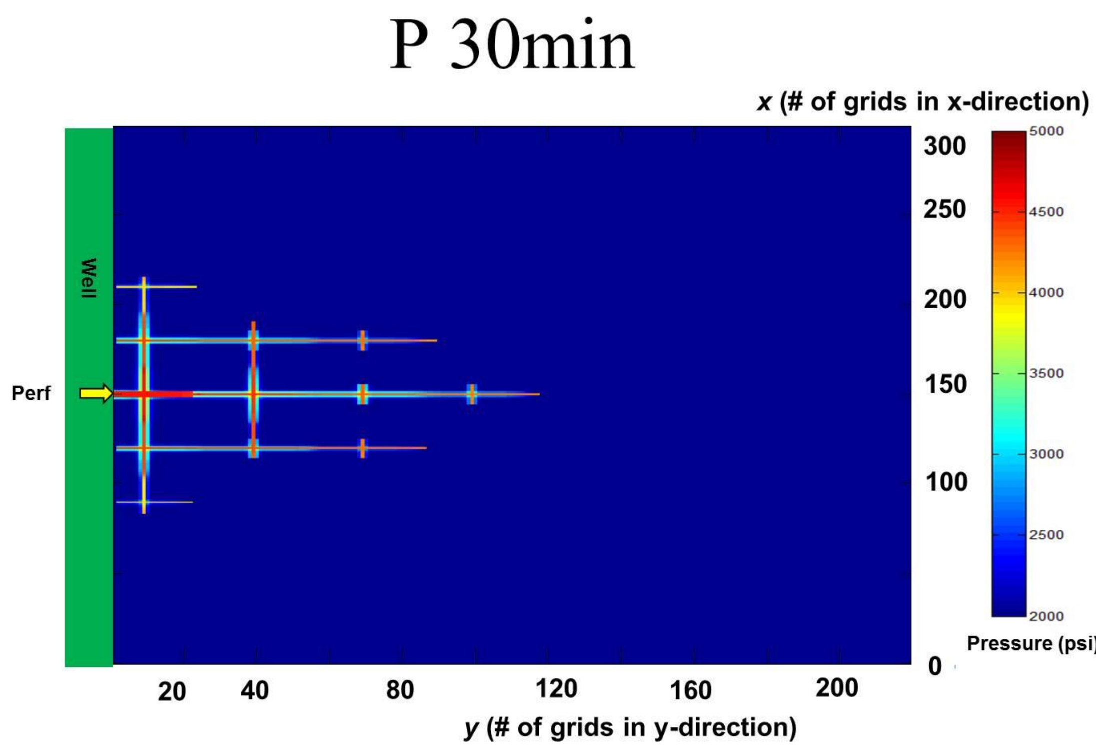
P 30min
x (# of grids in x-direction)
300
250
200
150
100
0
Well
Perf
5000
4500
4000
3500
3000
2500
2000
Pressure (psi)
20
40
80
120
160
200
y (# of grids in y-direction)

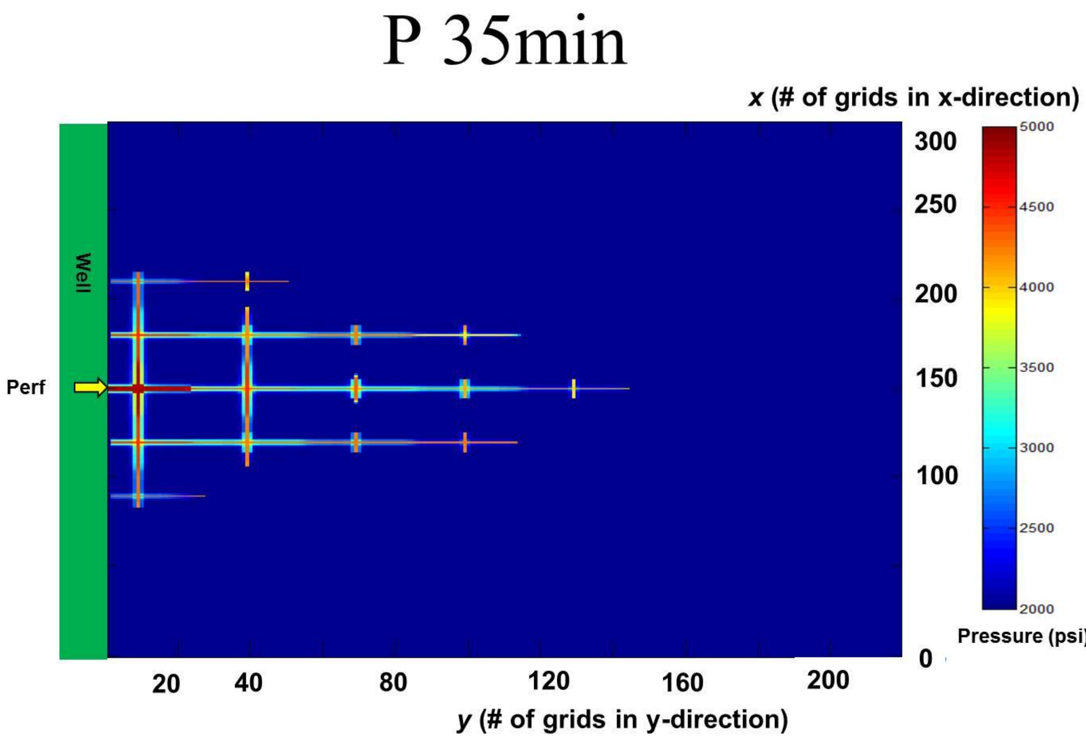

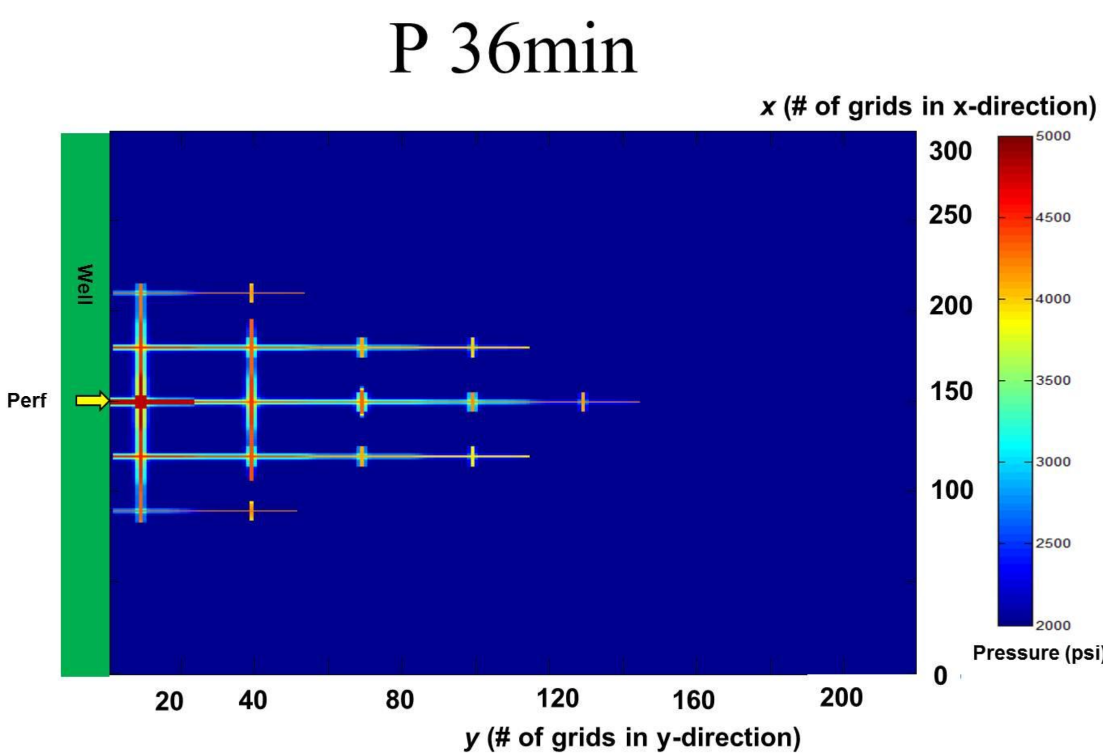

Figure 46. Pressure from the complex network simulation for different time-points.

Unlike the permeability maps, the -pressure maps show details of leakoff through the closed natural fractures. Therefore, the pressure map displays a more complex geographical network. In order to accurately represent the shale gas reservoir, the reservoir was designed to have ultra-low permeability. Therefore, the pressure distribution reflecting leakoff of the fracture fluid shows that the leakoff takes a narrow path through the matrix. However, the path taken by leakoff through the closed natural fractures is rather wide. We therefore decided to investigate how a complex fracture network can be created in a complex, naturally fractured reservoir.

Figure 47 presents the bottom hole treating pressures plots, which are scaled according to conditions.

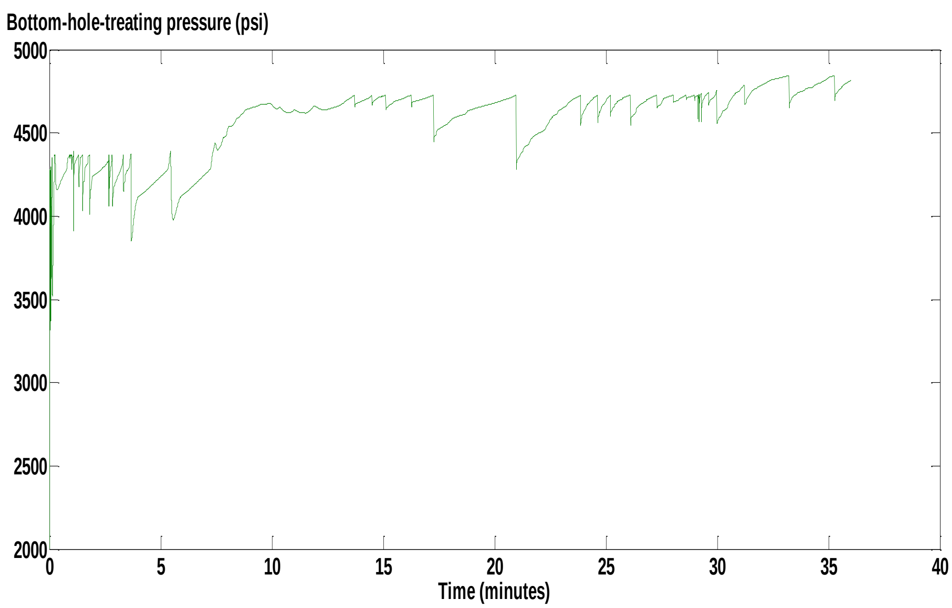

(a) BHTP (psi) versus time (minutes) with a linear scale.

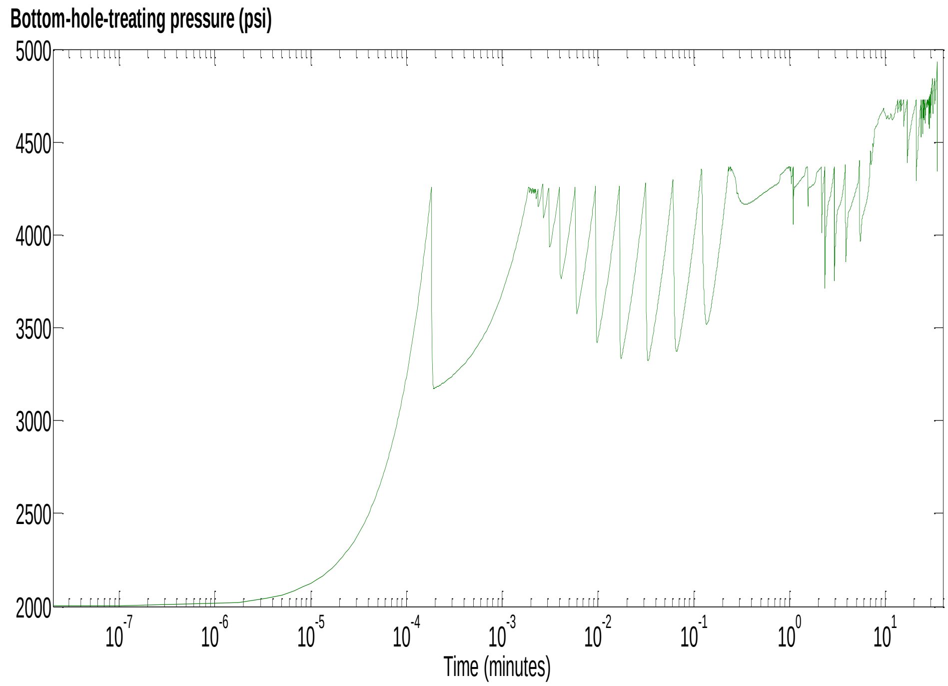

(b) BHTP (psi) versus time (log(minute)) with a semi-log scale.

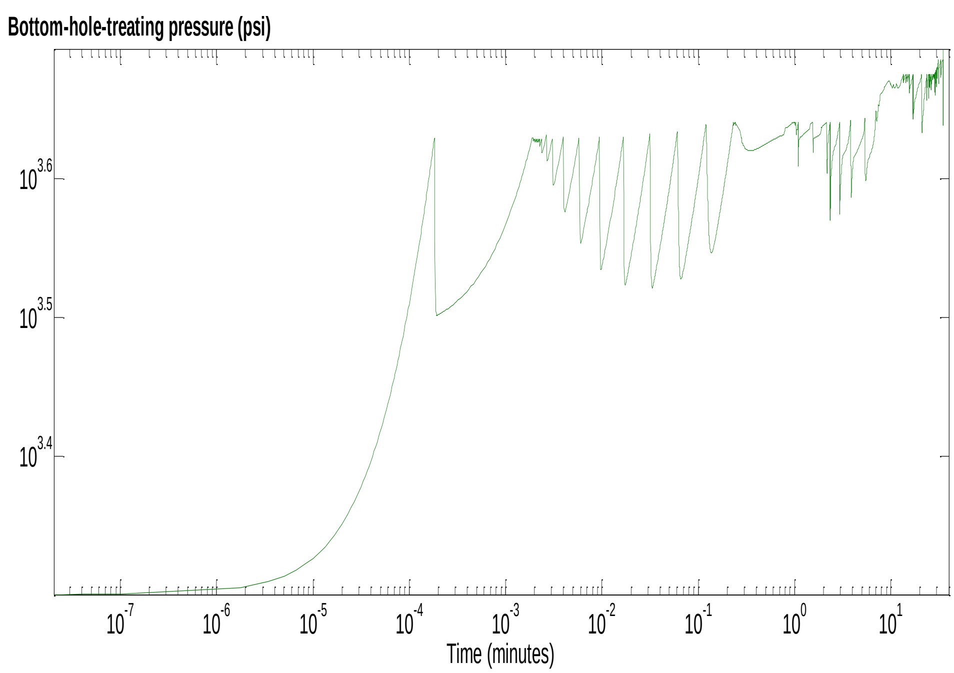

(c) BHTP (log(psi)) versus time (log(minute)) using a log-log scale.

Figure 47. BHTP versus time plots for the complex network simulation.

BHTP plots in Figure 47 may be interpreted to predict fracture propagation behavior further to the network geometry because the pressure response analytically reflects the propagation pattern. However, due to the complexity of the interpretation analysis, this work is left as a future work in this research.

As a result, we observed the creation of complex fracture network in this section (5.4). The series of propagation patterns including immediate opening, opening after crossing, and crossing without opening interacting natural fractures generated complex fracture geometry.

5.5 The Introduction of *Fracture Network Index (FNI)* and *Width Anisotropy* (W_{ani})

From the results driven from the section 5.1 to 5.3, we can conclude that the minimum propagation pressures selected from Equation 25 governs the propagation pattern at the intersection between the natural fracture and the hydraulic fracture. The width difference was also observed according to the propagating directions. The effect of rock toughness, natural fracture spacing, and stress anisotropy were investigated independently through the sections but the results were not quantified as a general form. Therefore, in this section, we analytically quantified the results by introducing the concept of *Fracture Network Index (FNI)* and *Width Anisotropy* (W_{ani}).

5.5.1 Fracture Network Index (FNI)

Fracture Network Index (FNI) is the dimensionless parameter which describes the fracture propagation behavior at the intersection between a natural fracture and a growing fracture. *FNI* can be derived from Equation 25 by reducing the opening criterion. The opening criterion derived from Equation 25 is

$$\boldsymbol{\sigma_{h@i,j} + \frac{K_{ICm@i,j}}{\sqrt{\pi L_{f@i,j}}} > \sigma_{H@i,j} + \frac{K_{ICnf@i,j}}{\sqrt{\pi L_{f@i,j}}}}$$

(Eq. 30).

Equation 30 can also be reduced with assuming the rock toughness of the natural fracture zero ($K_{ICnf} = 0$) and applying simple algebra leaving the value one at the left hand side as:

$$\mathbf{1} > \frac{(\boldsymbol{\sigma_{H@i,j}} - \boldsymbol{\sigma_{h@i,j}})}{\boldsymbol{K_{ICm@i,j}}}\sqrt{\boldsymbol{\pi L_{f@i,j}}}$$

(Eq. 31),

and can be re-written as a general form by converting $\sqrt{\mathbf{12\pi}}$ to 6.13996 as:

$$\mathbf{1} > 6.13996\,\frac{(\,\boldsymbol{Stress\ Anisotropy, psi}\,)}{(\boldsymbol{Rock\ Toughness\ of\ the\ Matrix},\ \boldsymbol{psi} * \sqrt{\boldsymbol{in}})}\sqrt{(\boldsymbol{Fracture\ Length, ft})}$$

(Eq. 32).

The right hand side of the Equation 32 is denoted as *Fracture Network Index (FNI)* through the rest of this thesis for convenience. Therefore, *FNI* is defined as:

$$\boldsymbol{FNI} = \mathbf{6.13996}\frac{(\,\boldsymbol{Stress\ Anisotropy}\,)}{(\boldsymbol{Rock\ Toughness\ of\ the\ Matrix})}\sqrt{(\boldsymbol{Fracture\ Length})}$$

(Eq. 33),

and the opening criterion can be written as:

$$\mathbf{1} > FNI$$

(Eq. 34),

the crossing as:

$$\mathbf{1} < FNI$$

(Eq. 35),

and, finally, the tendency of the opening after crossing can be written as:

$$\mathbf{1} < FNI \approx 1$$

(Eq. 35).

FNI values calculated from the cases studies in the sections 5.1 to5.3 is listed at Table 17 below.

Table 17. The results of *Fracture Network Index (FNI)* from the sections 5.1 to 5.3.

Section#	Case#	Rock toughness ($K_{ICmatrix}$), $psi * in^{0.5}$	Stress Anisotropy ($\sigma_H - \sigma_h$), psi	Fracture Length (L_f), ft	*Fracture Network Index (FNI)*, fractional
5.1	1a	100	50	8.028	8.69839741
5.1	1b	750	50	8.028	1.15978632
5.1	1c	1500	50	8.028	0.57989316
5.2 (Step 1)	2a	455	50	0.06	0.16527219
5.2 (Step 1)	2b	455	50	8.028	1.91173569
5.2 (Step 2)	2c	455	50	2.198	1.00031783
5.2 (Step 2)	2d	455	50	2.198	1.00031783
5.3	3a	455	10	0.06	0.03305444
5.3	3b	455	500	0.06	1.65272194

From the Table 17, we can clearly predict the interaction behavior between the natural fracture and the hydraulic fracture by using *FNI*.

In this section, we introduced a simple measure, *FNI*, which quantifies the interaction between and a natural fracture and a growing fracture. Although critical interactions were implemented on *FNI* in this study, it is not enough to predict the geometry of a fracture network in the actual field yet. It needs to be extended further to predict more complex propagation pattern by including various other effects such as shear slippage, contact angle (θ), near wellbore damages, height growth, and etc..

5.5.2 *Width Anisotropy* (W_{ani})

From the case studies through 5.1 to 5.3, we have observed a narrower width of the fracture propagating to the x direction than the one propagated to the y direction. We also have mentioned that this difference was caused by the distinct width calculation from Equation 27 and 28. Therefore, combining Equation 27 and 28, we can derive a value which quantifies this width difference. By simply subtracting the width in Equation 28 from Equation 27, we can get the *Width Anisotropy* (W_{ani}) as:

$$\boldsymbol{W_{ani}, ft = \frac{(1-\nu)h_f\left(\sigma_H(i,j)-\sigma_h(i,j)\right)}{G}},$$

(Eq. 36),

and it can be written as the general form as:

$$\boldsymbol{W_{ani}, ft = \frac{(1-\nu)h_f(\text{Stress Anisotropy}, psi)}{G}}$$

(Eq. 37).

As seen in Equation 37, stress and width anisotropies are linearly related each other with the assumption of constant height. Because the height growth occurs through the small region compared to the horizontal growth, W_{ani}, is a good measure predicting the width of connected networks.

Table 18 shows the W_{ani} calculated from above case studies.

Table 18. The calculation of W_{ani} through the case studies in the section 5.1-5.3.

Section#	Case#	Fracture Height (h_f), ft	shear mod. (G), psi	Poisson's ratio (ν), fractional	Stress Anisotropy ($\sigma_H - \sigma_h$), psi	Width Anisotropy (W_{ani}), ft
5.1	1a	100	2170000	0.15	50	0.001958525
5.1	1b	100	2170000	0.15	50	0.001958525
5.1	1c	100	2170000	0.15	50	0.001958525
5.2 (Step 1)	2a	100	2170000	0.15	50	0.001958525
5.2 (Step 1)	2b	100	2170000	0.15	50	0.001958525
5.2 (Step 2)	2c	100	2170000	0.15	50	0.001958525
5.2 (Step 2)	2d	100	2170000	0.15	50	0.001958525
5.3	3a	100	2170000	0.15	10	0.000391705
5.3	3b	100	2170000	0.15	500	0.019585253

The W_{ani} calculated from in the Table 18 perfectly proves the results generated from the above case studies.

Similar to *FNI*, W_{ani} suggested in this section provides the simple measurement of the width difference along the x and y directions. The fracture width of each branch of the complex fracture network is obviously smaller than that of a single fracture, and the conventionally used proppant might not be able to be transported to the tip of the fracture network. Thus, W_{ani} could be used as a measurement in selecting proper proppant for a fracture treatment in the naturally fractured reservoirs. W_{ani} also can be developed further by incorporating height growth, the effect of angle, and etc..

Chapter 6

CONCLUSIONS AND RECOMMENDATIONS

In this research, the interactions between a growing hydraulic fracture and the surrounding natural fractures were modeled and investigated how the interaction will contribute to the creation of a fracture network. Five possibilities that might occur during the hydraulic fracture of naturally fractured reservoirs were quantified through the series of case studies and simulations.

1. The natural fractures may have no influence and the hydraulic fracture will propagate in a direction perpendicular to the minimum horizontal stress as if there is no natural fracture in the reservoir. This interaction behavior is denoted as crossing. This behavior tends to occur when *Fracture Network Index (FNI)* is greater than 1.

2. The hydraulic fracture intersects the natural fracture, and crosses initially and opens after the fluid pressure reaches enough energy to initiate opening of the natural fracture. Through the case studies, we figure out that this pattern is likely to happen when *FNI* is greater but very close to 1.

3. The natural fractures may be opened and the hydraulic fracture will propagate along the natural fracture path. This interaction behavior is denoted as opening. Large stress anisotropy and rock toughness, and small distance to the natural fracture may generate opening and these factors are all implemented to the criterion, *FNI* less than 1.

4. Large in-situ stress anisotropy may cause different profile of the fracture width. The width calculated for the fractures propagated in the direction parallel to the minimum horizontal stress show narrower width than the fractures grew perpendicular to the minimum horizontal stress direction. This phenomenon is quantified through the introduced, *Width Anisotropy* (W_{ani}). W_{ani} quantifies the difference in width at a grid block with the linear relationship of stress anisotropy.

5. Combination of above 4 aspects within the reservoir having large number of natural fractures may create complex fracture network as shown in the section 5.4.

The measurements introduced in this study to predict complex fracture propagation in shale reservoirs are *FNI* and W_{ani}, and it can be developed further to incorporate various effects such as height growth, contact angle, shear slippage, tortuosity, multiphase flow, and etc., for an accurate prediction. After implementing these effects, we could match BHTP plots with *FNI* and W_{ani} to completely predict the complex fracture network growth with respect to time. However, above works are left as a future work. In addition, the development of adequate proppant transportation model in the naturally fractured reservoirs is another suggested work for the future.

NOMENCLATURE

a	fracture half height or zone of slippage	[in]
A	cross sectional area	[ft^2]
B	formation volume factor	[RB/STB]
C_w	the compressibility of water	[psi^{-1}]
C_w	the compressibility of water	[psi^{-1}]
E	Young’s modulus	[GPa]
G	shear modulus of rock formation	[psi]
H or h_f	fracture height	[ft]
h	gross fracture height	[ft]
K_f	the coefficient of friction	[-]
$K_{I,II,III}$	stress intensity factor mode I, II, III	[psi-√in]
K_{IC}	rock toughness or critical stress intensity factor	[psi-√in]
K_{ICm}	rock toughness of matrix	[psi-√in]
K_{ICnf}	rock toughness of natural fracture	[psi-√in]
k_{nf}	the permeability of natural fracture	[md]
k_r	relative permeability	[md]
$k_{x\ or\ y}$	permeability on x or y direction	[md]
L_f	half length of fracture	[ft or in]
l	fracture half length	[ft]
$\dot{m}_{cx}$	mass flux for component c along the x, y and z direction	[lbm/D-ft^2]
m_{vc}	mass of component c per unit volume of rock	[lbm]
p_f	fracturing fluid pressure	[psi]

$p_{initiation}$	initiation pressure	[psi]
$p_{propagation}$	propagation pressure	[psi]
p_{tip}	the pressure at the tip of fracture	[psi]
p_w	variable-rate pressure-change response	[psi]
p_{wb}	bottomhole treating pressure	[psi]
p_r	formation pore pressure	[psi]
q	fluid flow rate	[bpm]
q_{mc}	rate of mass depletion for component c through injection	[lbm/D]
R_s	solution gas-oil ratio	[scf/STB]
r	distance from a tip of the crack	[ft or in]
t	treatment time	[min or day]
S_w	saturation of water	[-]
FNI	Fracture Network Index	[-]
Δt or dt	time since shut-in	[sec]
T_o	tensile stress of the rock	[psi]
W_{ani}	width anisotropy	[ft]
w	fracture width	[ft or in]
α	biot's poroelastic constant	[-]
α_c	volumetric conversion factor	[-]
β_c	transmissibility conversion factor	[-]
ε	convergence criteria	[-]
θ	the angle measured from the fracture axis	[°]
μ	fluid viscosity	[cp]
ν	Poisson's ratio	[-]

ρ	fluid density	[lb/gal]
σ_1	maximum principal stress	[psi]
σ_3	minimum principal stress	[psi]
σ_c	critical stress	[psi]
σ_{ext}	tectonic stress	[psi]
σ_h	minimum horizontal in-situ stress	[psi]
$\sigma_{\min}$	minimum in-situ stress	[psi]
σ_n	normal stress acting on the plane of natural fracture	[psi]
σ_{ob}	overburden stress	[psi]
σ_t	the stress acting parallel to the natural fracture	[psi]
$\Delta\sigma_{\mathrm{c}}$	change in stress due to rock toughness	[psi]
$\Delta\sigma_{\mathrm{P}}$	pore pressure expansion stress	[psi]
τ	shear stress	[psi]
τ_0	the inherent shear strength of the natural fracture plane	[psi]
Φ	porosity	[-]

REFERENCES

Aquilera, R. 2008. Role of natural fractures and slot porosity on Tight Gas Sands. Paper SPE 114174 presented at the SPE Unconventional Reservoirs Conference, Keystone, Colorado, USA, 10-12 Feb. doi: 10.2118/114174-MS

Baree, R.D. and Mukherjee, H. 1996. Determination of pressure dependent leakoff and its effect on fracture geometry. Paper SPE 36424 presented at the SPE Annual technical Conference and Exhibition, Denver, Colorado, 6-9 Oct. doi: 10.2118/36424-MS

Blanton T.L. 1982 Experimental Study of Interaction Between Hydraulicalyy Induced and Pre-Existing Fractures. Paper SPE 10847 presented at the SPE Unconventional Gas Recovery Symposium, Pittsburgh, Pennsylvennia, USA, 16-18 May. doi: 10.2118/10847-MS.

Crouch, S.L. and Starfield, A.M. 1983. *Boundary Element Methods in Sold Mechanics: With Application in Rock Meechanics and Geological Engineering.* London: George Allen and unwin.

Taleghani, A.D. 2009. Analysis of hydraulic fracture propagation in fractured reservoirs: an improved model for the interaction between indeced and natural fractures. Ph.D dissertation, Univ. of Texas at Austin.

DOE/EIA report: "Annual Energy Outlook 2010 with Projections to 2035: Importance of low-permeability natural gas reservoir," EIA, http://www.eia.doe.gov/oiaf/aeo/lpnat_gas.html, 2010.

Geertsma, J. and de Klerk, F.A. 1969. Rapid Method of Predicting Width and Extent of Hydraulic Induced Fractures. *J Pet Technol* **21** (12): 1571-81; *Trans*., AIME, **246**. SPE-2458-PA. doi: 10.2118/2458-PA.

Grebe, J.J. and Stoesser, M. 1935. Increasing crude production 20,000,000 bbl. from established fields. *World Petroleum J*, (August), 473-82.

Jaeger, J. C., N. G. W. Cook, et al. 2007. *Fundamentals of rock mechanics.* Malden, MA, Blackwell Pub.

Keshavarzi, R. and Mohammadi, S. 2012. A new Approach for numerical Modeling of Hydraulic Fracture Propagation in Naturally Fractured Reservoirs. SPE 152509-MS.

Lorenz, J. C. and Warpinski, N. R. 1996. Natural fracture characteristics and effects. Leading Edge, 15(8), 909-911.

Lawn, B. 1993. *Fracture of Brittle Solids*, Camvridge University Press, 2004. doi: 10.1017/ CBO9780511623127

Nolte, K.G. 1988. Fracture Design Considerations Based on Pressure Analysis. *SPEPE* **13** (1): 22-30. SPE-10911-PA. doi: 10.2118/10911-PA

Perkins, T.K. and Kern, L.R.1961. Widths of Hydraulic Factures. *J Pet Technol* **13** (9): 934-949; *Trans.*, AIME, **222**. SPE-89-PA. doi: 10.2118/89-PA

Poltluri, N., D. Zhu, and Hill, A.D. 2005.The Effect of Natural Fractures on Hydreaulic Fracture Propagation. Paper SPE 94568 presented at the SPE European Foramtion Damgae Conference, Sheveningen, The Netherlands, 25-27 May. doi: 10.2118/94568-MS.

Renshaw, C. E., and D.D. Pollard. 1998. An experimetal Verified Criterion for Propagation Across Unbounded Frictional Interfaces in Brittle Linear Elastic Materials. International Journal of Rock Mechanics and Mining Science & Geomechanics, **32** (3): 237-249. doi: 10.1016/0148-9062(94)00034-4.

Teufel, L.W. and Clark, J.A. 1984. Hydraulic fracture propagation in layered rock: Experimental studies of fracture containment. *SPEJ* **24** (1): 19-32. SPE-9848-PA. doi: 10.2118/9878-PA.

Settari A. 2004. Methods For Modeling Dynamic Fractures In Coupled Reservoir And Geomechanics Simulation. Paper SPE 90874 presented at SPE Annual Technical Conference and Exhibition, Houston, Texas, 26-29 September. doi: 10.2118/90874-MS.

Veatch, R.W., Moschovidis, Z. A., and Fast, C.R. 1989. An overview of hydraulic fracturing. In: Gidley, Holditch, Nierode, Veatch, editors. Recent advances in hydraulic fracturing. Monograph, Vol. 12, Richrdson: SPE, 1-38.

Warpinski, N.R. 1991. Hydraulic Fracturing in Tight Fissured Media. *J Pet Technol* **43** (2): 146-150 & 208-209. SPE-20154-PA. doi: 10.2118/20154-PA.

Warpinski, N.R. and Teufel, L.W. 1987. Influence of Geologic Discontinuities on Hydrauli Fracture Propagation. *J Pet Technol* **39** (2): 209-220; *Trans.*, AIME, **283.** SPE 13224-PA. doi: 10.2118/13224-PA.

Weijers, L. 1995. The newar-wellbore geometry of hydraulic fractures initiated from horizontal and deviated wells. Ph.D. Dissertation, Delft Univ. of Tech.

Weng, X., Kresse, O., Cohen C., Wu R., and Gu H. 2011. Modeling of Hydreaulic Fracutre Network Propagation in a Naturally Fractured Formation. Paer SPE 140253 presented at the SPE Hydraulic Fractureing Technology Conference, The Woodlands, Texas, USA, 24-26 Jan. doi: 10.2118/140253-MS.

Zeini Jahromi, M., Wang, J. Y., and Ertekin, T. 2012. Development of a Two-Dimensional Fully Coupled Numerical Simulator for Modeling Hydraulic Fracture Propagation and Long-term Recovery in Tight Gas Reservoirs. (under review)

Zhang, X., Jeffery, R.G., and Thiercelin, M. 2007b. Effects of Frictional Geological Discontinuities on Hydraulic Fracture Propagation. Paper SPE 106111 presented at the SPE Hydraulic Fracture Technology Conference, College Station, Texas, USA, 29-31 Jan. doi: 10.2118/106111-MS.